UC Berkeley
UC Berkeley Electronic Theses and Dissertations

Title
Growth and Characterization of Silicon Carbide Thin Films and Nanowires

Permalink
https://escholarship.org/uc/item/62z8k32g

Author
Luna, Lunet Estefany

Publication Date
2016

Peer reviewed|Thesis/dissertation

eScholarship.org Powered by the California Digital Library
University of California

Growth and Characterization of Silicon Carbide Thin Films and Nanowires

by

Lunet Estefany Luna

A dissertation submitted in partial satisfaction of the
requirements for the degree of
Doctor of Philosophy

in

Chemical Engineering

in the

Graduate Division

of the

University of California, Berkeley

Committee in charge:

Professor Roya Maboudian, Chair
Professor Carlo Carraro
Professor Jeffrey Reimer
Professor Liwei Lin

Summer 2016

Growth and Characterization of Silicon Carbide Thin Films and Nanowires

Copyright 2016

by

Lunet Estefany Luna

Abstract

Growth and Characterization of Silicon Carbide Thin Films and Nanowires

by

Lunet Estefany Luna

Doctor of Philosophy in Chemical Engineering

University of California, Berkeley

Professor Roya Maboudian, Chair

Silicon carbide (SiC) based electronics and sensors hold promise for pushing past the limits of current technology to achieve small, durable devices that can function in high-temperature, high-voltage, corrosive, and biological environments. SiC is an ideal material for such conditions due to its high mechanical strength, excellent chemical stability, and its biocompatibility. Consequently, SiC thin films and nanowires have attracted interest in applications such as micro- and nano-electromechanical systems, biological sensors, field emission cathodes, and energy storage devices.

In terms of high-temperature microdevices, maintaining low-resistance electrical contact between metal and SiC remains a challenge. Although SiC itself maintains structural and electrical stability at high temperatures, the metallization schemes on SiC can suffer from silicide formation and oxidation when exposed to air. The second chapter presents efforts to develop stable metallization schemes to SiC. A stack consisting of Ni-induced solid-state graphitization of SiC and an atomic layer deposited layer of alumina is shown to yield low contact resistivity of Pt/Ti to polycrystalline n-type 3C-SiC films that is stable in air at 450 ºC for 500 hours.

The subsequent chapters focus on the growth and structural characterization of SiC nanowires. In addition to its structural stability in harsh-environments, there is interest in controlling SiC crystal structure or polytype formation. Over 200 different polytypes have been reported for SiC, with the most common being 3C, 4H, and 2H. In terms of SiC nanowire growth, the 3C or cubic phase is the most prevalent. However, as the stacking fault energy for SiC is on the order of a few meV, it is common to have a high density of stacking faults within a given SiC crystal structure. Thus, to enable reliable performance of SiC nanowires, a growth method that can promote a specific polytype or reduce stacking faults is of importance. Ni-catalyzed chemical vapor deposition method is employed for the growth of the nanowires. The effects of substrate structure and quality as well as the various growth parameters such as temperature, pressure, and

post-deposition annealing are investigated. Most significant has been the growth and characterization of vertically aligned hexagonal phase (or 4H-like) SiC nanowires grown on commercially available 4H-SiC (0001).

The studies presented in this thesis tackle issues in SiC metallization and nanowire growth in efforts to expand the versatility of SiC as a material platform for novel devices.

Dedicated to my father and in memory of my mother.

Table of Contents

1. Introduction 1

1.1. A brief history of silicon carbide (SiC).. 1

1.2. Exploring 1D and 2D SiC nanomaterials.. 3

1.3. Outline of this work 5

2. Stable metallization of n-type polycrystalline 3C silicon carbide.. 6

2.1. Status of SiC metallization.. 6

2.2. Contact characterization.. 7

2.3. Experimental section.. 9

2.3.1. Polycrystalline n-type 3C-SiC deposition.. 9

2.3.2. Ni-induced graphitization 10

2.3.3. Fabrication of circular transmission line method structures.. 11

2.3.4. Alumina deposition.. 11

2.3.5. Long-term stability testing.. 11

2.4. Effect of nickel-induced nanocrystalline graphitic (NCG) interlayer formation on Pt/Ti contact to n-type 3C-SiC.. 11

2.5. Effect of Ni-induced NCG and Al_2O_3 overlayer for a stable low resistivity contact between Pt/Ti and n-type 3C-SiC 12

2.6. Summary.. 15

3. Nickel-induced silicon carbide nanowire growth on silicon carbide.. 16

3.1. Introduction to metal-catalyzed semiconductor nanowire growth.. 16

3.2. SiC nanowires on SiC substrates 17

3.3. Experimental section.. 18

3.3.1. As-received 4H-SiC (0001) substrates.. 18

3.3.2. Nanowire synthesis and characterization.. 20

3.4. Effect of growth temperature.. 21

3.5. Catalyst composition.. 22

3.6. Effects of catalyst composition on SiC nanowire growth.. 27

3.7. Catalyzed *vs.* uncatalyzed SiC growth.. 28

3.8. Effect of substrate 30

3.9. Summary.. 36

4. Demonstration of 4H-like SiC nanowires with vertical alignment.. 37

4.1. SiC nanowire orientation on SiC substrates.. 37

4.2. Experimental Section.. 40

4.3. Raman spectroscopy characterization.. 41

4.4. Atomic resolution transmission electron microscopy (TEM) characterization 42
4.5. Structure modeled by axial next nearest neighbor Ising and nucleation models 45
4.6. Substrate induced vertical growth 48
4.7. Nanowire morphology 51
4.8. Electronic characterization 51
4.8.1. Sample preparation for electron energy loss spectroscopy (EELS) 52
4.8.2. Nanowire EELS analysis 52
4.9. Summary 57

5. Catalyst cluster formation 58
5.1. Introduction 58
5.2. Ex-situ studies of Ni-on-SiC 60
5.2.1. Varying temperature 60
5.2.2. Varying pressure 65
5.2.3. Polytype 68
5.2.4. Preliminary cross-sectional TEM 69
5.3. Preliminary low energy electron microscopy (LEEM) studies of Ni-on-SiC 71
5.3.1. Temperature calibration 71
5.3.2. Mimicking ex-situ experiments with in-situ LEEM 72
5.4. Summary 77

6. Conclusions and future work 78

Bibliography 79

Appendix A. Cross-sectional TEM sample preparation 92

Appendix B. Common surface reconstructions 98

Acknowledgments

I would like to thank my graduate advisor and mentor Prof. Roya Maboudian who guided and supported my research endeavors throughout the years. Her encouragement and belief in my success at UC Berkeley was evident early in my graduate school career and played a pivotal role both inside and outside my academic life. I would also like to thank Prof. Carlo Carraro for his encouragement, invaluable insight, and help in understanding various techniques and measurements used in this dissertation.

At UC Berkeley, I had the privilege to surround myself with inspiring role models, collaborators, and mentors. Along this vein, I am thankful for Prof. Jeffrey Reimer's mentorship, enthusiasm, and participation in my graduate school career. I would also like to acknowledge Prof. Liwei Lin as a member of my dissertation committee. Additional thanks goes to Prof. Jonas Johansson for fruitful and exciting research collaborations. I sincerely appreciate the Molecular Foundry staff members for their expertise and training towards the completion of this research: Dr. Colin Ophus, Dr. Velimir Radmilovic, Dr. Burak Ozdol, Dr. Jim Ciston, Dr. Andreas Schmid, Dr. Gong Chen, Dr. Peter Ercius, Chengyu Song, Marissa Libbee, Dr. Karen Bustillo, Dr. Roberto dos Reis, Dr. Virginia Altoe, Dr. Tevye Kuykendall, and Tracy Mattox.

I am grateful for having met wonderful students both inside and outside the Maboudian laboratory group. Yi-Pei Li helped me immensely during my first years in graduate school and I am extremely grateful for his friendship. Thank you to Anna Harley-Trochimczyk and Leslie Chan for their research insight, enlightening conversations, friendship, and to opening my eyes to the fun of graduate school; I learned an invaluable amount from these two impressive engineers. Thanks to Steven Delacruz for his positive attitude, honest conversations, and for patiently helping me to submit my dissertation forms. Rosemarie de la Rosa and Willie Mae Reese for keeping me grounded and making sure I have fun. Thank you to the past and current Maboudian lab members for training, camaraderie, and help in troubleshooting research obstacles, these include: Ben Hsia, Yongkwan Kim, Albert Gutes, John Alper, Shuo Chen, Hu Long, Hai Liu, Chuan-Pei Lee, Arthur Montazeri, and Sinem Ortaboy.

I would also like to acknowledge the organizations that supported this dissertation work: National Science Foundation (Graduate Research Fellowship Program and Division of Materials Research # 1207053), University of California Chancellor's Fellowship, and the Gates Millennium Scholarship. Work at the Molecular Foundry was supported by the Office of Science, Office of Basic Energy Sciences, of the U.S. Department of Energy under Contract No. DE-AC02-05CH11231.

A special thank you goes to Jared Shamwell for his continued support across three time zones, his unique prospective on life, and for staying awake until I finished working even just to say goodnight. Finally, I am indebted to my family for their unconditional love and optimism. My brother Rafael raised me to face my fears and taught me that only I can hold myself back. My sister Unique through phone conversations, video chats, and extended visits to Berkeley played a

critical role in puzzling my life together. My brother Mauricio, a true engineer at heart, always inspired me with his love for science, innovation, and engineering. My brother Carlos spoke words of wisdom and optimism that kept me on track. My father Rafael motivated me to push further and take advantage of opportunities he had only dreamed of. My last acknowledgment goes to my mother Crescencia, who taught me determination and perseverance. It is because of her I try my best with a big smile – may she rest in peace.

1. Introduction

1.1. A brief history of silicon carbide (SiC)

SiC is a chemically inert and mechanically stable wide-band gap semiconductor that is well known for its ability to withstand extreme conditions, wherein widely used silicon (Si) would fail [1,2]. SiC can form over 200 different crystal structures, all of which are formed by a basis combination of the 100% hexagonal crystal structure (wurtzite, 2H-SiC) and the 0% hexagonal crystal structure (zinc-blende, 3C-SiC). A number followed by a letter denotes the crystal structure: the number indicates the number of SiC bilayers required to reproduce the crystal pattern, and the letter indicates the symmetry of the crystal lattice (hexagonal, H or cubic, C). Polytypes are also commonly distinguished with an ABC stacking classification (Figure 1.1). With the ABC nomenclature, cubic and hexagonal crystal structures are described as ABC and AB stacking, respectively (Figure 1.2). Two striking differences between cubic and hexagonal SiC are the frequencies of the dominant transverse optical phonon mode (796 cm^{-1} for cubic, 776 cm^{-1} for hexagonal) and band gap energies (2.3 eV for cubic, 3.3 eV for hexagonal).

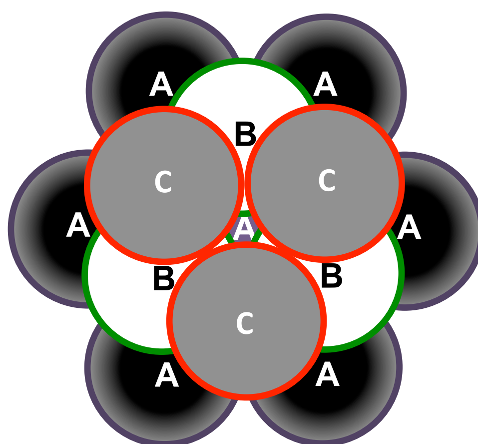

Figure 1.1. Schematic of ABC stacking depicted by close-packed spheres. Different pattern combinations of A, B, and C stacking layers determine different polytypes.

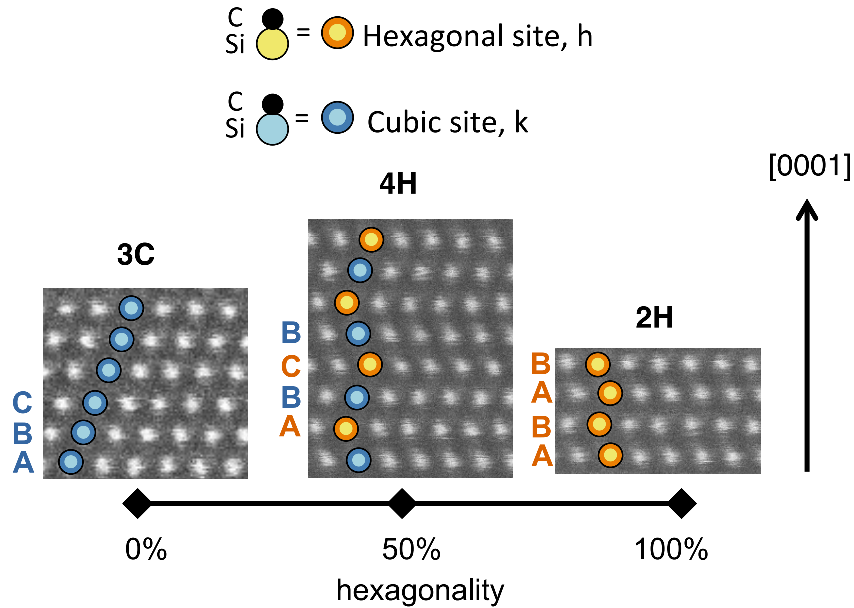

Figure 1.2. Atomic resolution micrographs of common SiC polytypes (3C, 4H, and 2H). For each polytype, the percent hexagonality and corresponding ABC stacking pattern is shown.

As Si is a mature technology and serves as the basis for most devices today, materials that can leverage Si fabrication techniques are desirable. The fact that Si and SiC share the same native oxide (silicon dioxide, SiO_2) places SiC in an opportune position to provide device durability and to take advantage of existing Si technology. Unlike Si, SiC widens device applicability into the harsh environment regime through its excellent intrinsic properties (Table 1.1). SiC's wider band gap, higher young's modulus, higher breakdown field, and higher thermal conductivity than Si allows for higher temperature operation, mechanical stability, higher voltage operation, and better heat dissipation, respectively.

Research has been conducted with various forms of SiC including amorphous, poly-, or single-crystalline films and single-crystalline wafers. The amorphous films provide flexible, resistive films for biomedical applications [3]. Also, compared to Si, single-crystalline SiC films induce low immune responses when placed in biological fluid [4]. Polycrystalline SiC films possess higher fracture stress than Si [5] and can withstand corrosive solutions [2], mechanical actuation [1,5], and high temperature [6]. Additionally, polycrystalline SiC can be doped to tailor its electrical properties for microdevices [7]. High quality, single-crystalline 4H-SiC (50% hexagonality) wafers are commercially available and have been used to facilitate substrate induced epitaxial growth of cubic [8] and hexagonal phase [9] SiC nanowires. Recent advancements in the minimization of defects in SiC wafer production have sparked interest in the development of SiC-based optical devices [10].

Table 1.1. Comparison of Si and SiC properties [11–13].

	Si	3C-SiC	4H-SiC
Band gap (eV)	1.1	2.3	3.3
Young's modulus (GPa)	185	392-694*	547
Breakdown electric field (kV/cm)	300	1,000	2,200
Thermal conductivity (W/cm-K)	1.49	3.6	3.7

*Experimental value depends on dopant level [14].

1.2. Exploring 1D and 2D SiC nanomaterials

A strong research interest in harsh-environment semiconductors is vital for pushing past the limits of current technology to achieve small, durable devices that can function in high-temperature, high-voltage, corrosive, and biological environments. SiC is an ideal material for such environments due to its high mechanical strength, excellent chemical stability, and biocompatibility. The research thrust towards smaller, more efficient, technologies has prompted the study of one (1D)- and two-dimensional (2D) SiC structures with dimensions in the nanometer regime. Such structures include nanowires [15,16] and thin films [17]. Particularly, SiC nanowires have attracted interest in applications such as biological sensors [18], field emission cathodes [19,20], and energy storage devices [21–23].

One of the main challenges with SiC technology addressed in this work includes stable, low contact resistivity metallization for high-temperature operation. The need for low contact resistivity metallization is evidenced by a growing interest in sensors that can operate under harsh environments. Sensing within these environments necessitates a robust semiconductor platform, different from those employed in traditional Si-based micro- and nano-electromechanical systems (M/NEMS). A robust material such as SiC provides compelling advantages not achievable with Si-based devices. However, although SiC performs well in harsh environments, its metallization scheme must also be able to perform well without oxidizing, delamination, or reacting to form resistive contacts.

An additional processing challenge addressed in this work includes polytype control of cubic and hexagonal growth of SiC nanomaterials. As SiC is characterized by extreme polytypism, the ability to control polytype serves as a way to target specific optical and electronic characteristics. One effective method to characterize SiC polytype is by Raman spectroscopy. As shown in Figure 1.3, SiC generates a rich Raman spectrum of induced phonon modes (atomic lattice vibrations) when subjected to incident visible light. The most dominant phonon modes are out-of-phase or optical lattice vibrations described as the transverse (TO) and longitudinal optical (LO) modes. The TO in particular is commonly used to identify the polytype of SiC. For 3C-SiC,

the TO and LO peak positions are centered at 796 and 964 cm^{-1}. On the other hand for 4H-SiC, the primary TO and LO peak positions are centered at 776 and 972 cm^{-1}.

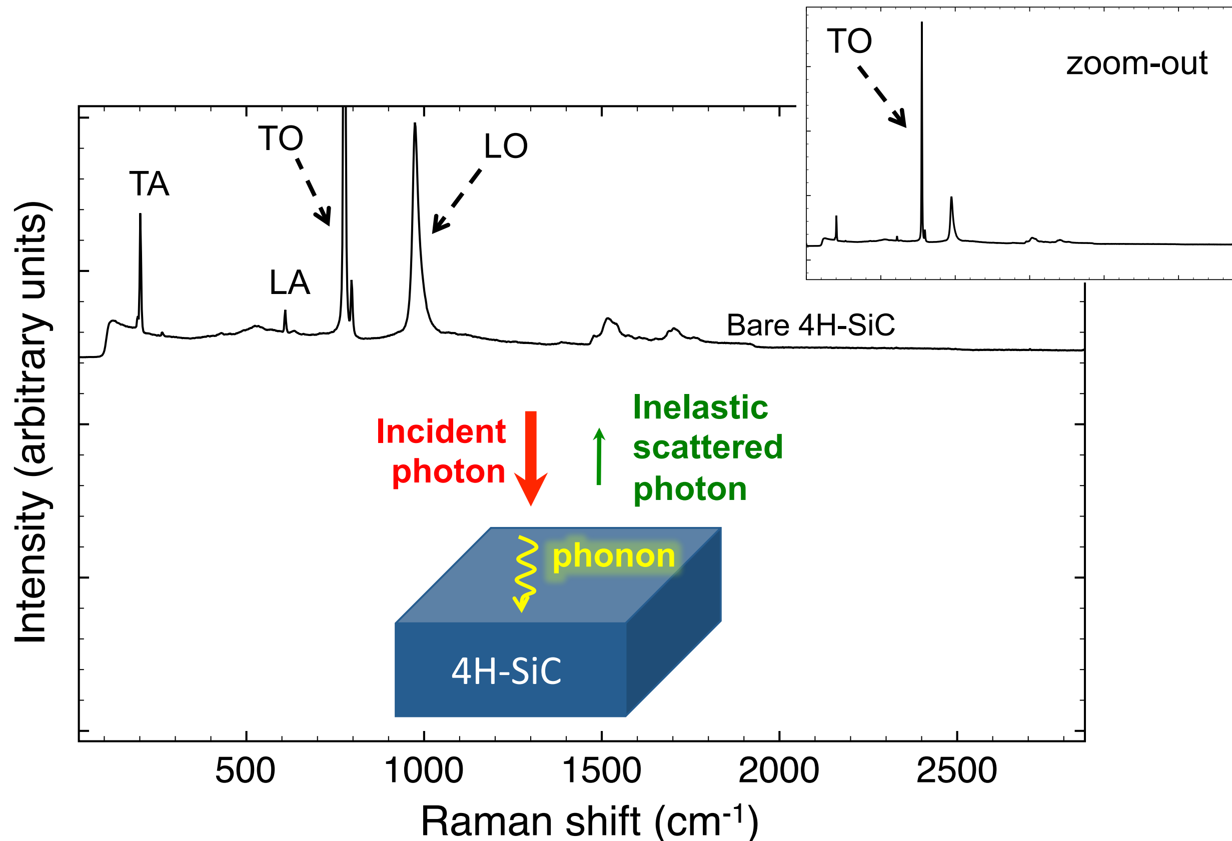

Figure 1.3. Raman spectrum of bare 4H-SiC (0001) substrate shows the different phonon modes available for this polytype. The transverse optical mode (TO) is the dominant signal. Nomenclature: Transverse acoustic (TA), Longitudinal acoustic (LA), and Longitudinal optical (LO). The unlabeled peaks around 1500 and 1700 cm^{-1} are due to second-order scattering, indicative of good crystallinity.

In the following chapters, SiC nanowires are grown using chemical vapor deposition (CVD). This growth mode presents opportunities to tailor nanowire properties such as diameter, length, doping, and polytype during nanowire growth on the wafer or die-level scale. The details of the nanowire growth process are important not only from a fundamental standpoint, but from an application standpoint as well. The growth mode dictates nanowire crystal structure, dimensions, doping, and the distribution on the substrate, all of which play a role in nanowire morphology and electrical properties. Controlling nanowire properties helps to tailor them for specific applications. For example, nanowire shape can be tailored to concentrate high electric fields in

field emission cathodes, dopant incorporation can be tailored to achieve desired conductivity in electronic devices, and crystal structure polytype and orientation can be tailored to obtain nanowires with specific band gaps for optoelectronics. Given that SiC polytypism is a challenge for bulk and nanomaterials, this dissertation also reports the effects of nanowire growth parameters on SiC polytype as well as morphology and orientation.

1.3. Outline of this work

Due to its unique intrinsic properties, SiC thin films and nanowires have attracted interest in applications such as M/NEMS, biological sensors, field emission cathodes, and energy storage devices. This dissertation first addresses the need for stable SiC metallization by presenting a metallization stack that incorporates solid-state graphitization of SiC and an atomic layer deposition of alumina (Chapter 2). The designed stack achieves low contact resistivity of Pt/Ti to polycrystalline n-type 3C-SiC films, which remains stable in air at 450 ºC for over 500 hours. Chapter 3 describes Ni-catalyzed chemical vapor deposition of SiC nanowires and reports the effects of growth temperature on nanowire morphology and crystallinity, identifies the primary catalyst for nanowire growth as Ni_2Si, and shows the effects of substrate surface on nanowire growth. Chapter 4 introduces vertically aligned, hexagonal phase SiC nanowires grown on commercially available 4H-SiC (0001) and explores the band gap variations across hexagonal phase SiC nanowires. Lastly, Chapter 5 delves further into the evolution of nickel silicide clusters present during nanowire growth.

2. Stable metallization of n-type polycrystalline 3C silicon carbide[1]

Stable metal contacts for devices based on silicon carbide (SiC) are required for high temperature microelectronics and microsensor devices. Ni-induced nanocrystalline graphitic carbon (NCG) is introduced between Pt/Ti and n-type polycrystalline 3C-SiC (polySiC) as a means of forming contacts that are stable at high temperature. With the addition of an alumina protection layer, this metallization scheme is further improved and can maintain low contact resistivity after 500 h at 450 °C in air. The role of the graphitic layer in both the formation and long-term stability of the contact is investigated. Although the formation of an ohmic contact between Pt/Ti and polycrystalline 3C-SiC does not require the graphitic carbon, this interfacial layer is necessary for maintaining low contact resistivity during long-term exposure to elevated temperature.

2.1. Status of SiC metallization

Micro-electricalmechanical systems (MEMS) technology enables a wide range of physical and chemical-sensing applications employed in consumer electronics, navigation systems, entertainment electronics, and bioengineered devices. While traditional Si-based MEMS are well developed and can undertake sensing tasks under ambient conditions, these devices fail when exposed to harsh environments due to the intrinsic material and surface properties of Si. Sensing in harsh environments, especially at high temperature (>400 °C), is drawing increasing attention, with potential applications in the energy sector (e.g., power plants, geothermal energy systems, and concentrated photovoltaics). The motivation is that enhanced pressure, temperature, and

---

[1] A modified version of this work was publish in S. Chen*, L.E. Luna*, Z. You, C. Carraro, R. Maboudian. "Ni-induced graphitization for enhanced long-term stability of ohmic contact to polycrystalline 3C-SiC." *J. Vac. Sci. Technol. A* 33 (2015) 031507. DOI: 10.1116/1.4916578. *Equal author contribution.

chemical sensing will allow more efficient operation. Thus, an intrinsically robust material such as silicon carbide is an ideal material to fabricate electronics and sensors capable of operation in harsh environments. Particularly, its mechanical and electrical stability and its chemical inertness make SiC well suited for designing devices for applications in high temperature and corrosive environments [17,24–27].

The introduction of SiC-based sensors for stable operation in harsh environments necessitates both a manufacturing process that is practical for large-scale production and reliable metal contacts [25]. While most of the reported stability testing are done in inert ambient (such as Ar or vacuum) [28,29], several studies have reported on the long-term stability of metal contacts to SiC upon exposure to elevated temperatures in air [30–34], which better mimics the environment of many practical harsh environment applications. Additionally, most of these contact studies have been conducted on single-crystalline SiC (4H, 6H) substrates. However to further advance MEMS designs, a more versatile and practical platform such as polycrystalline SiC is needed. MEMS devices can be manufactured from deposited polycrystalline SiC films on silicon nitride on Si [35], silicon dioxide on Si [36], or aluminum nitride (AlN) on Si for better lattice matching [37]. Through the use of SiC thin films, a larger adaptation of harsh environment devices comes closer to fruition. Several as-deposited metals on polycrystalline 3C-SiC (polySiC) films result in ohmic contacts [38] and show potential for high temperature operation [39–43]. However, the metal contact stability at elevated temperatures in air still remains a problem. A SiC metallization scheme for testing in air was established through the addition of a graphitized layer between Pt/Ti contacts and n-type polySiC. This scheme lowered the contact resistivity and maintained its low value after exposure to 550 °C in air; the authors reported that the nanocrystalline graphitic (NCG) layer served as a reaction barrier to silicide formation [44]. The NCG layer was formed at high temperature (1300 °C) and in ultrahigh vacuum (10^{-9} Torr). These temperature and pressure values significantly constrain the scale-up of the process to high volume production.

In this work, the high thermal and pressure budget associated with the formation of NCG in previous work is attenuated through use of an alternative graphitization method, namely Ni-induced graphitization. The Ni-induced graphitization approach is shown to increase the long-term reliability of Pt/Ti/SiC contacts to n-type polySiC in high temperature environments. We show that the Ni-induced NCG is a key factor for maintaining a robust interlayer between the metal and the semiconductor, hindering solid-state diffusion, and in obtaining long-term stability at 450 °C. The metallization scheme described in this chapter proves advantageous in the long-term testing performance, which comes from a thicker NCG layer with fewer defects.

2.2. Contact characterization

Contact between a metal and semiconductor can form linear (non-rectifying, ohmic) or non-linear (rectifying, schottky) contacts. The contact behavior depends on the magnitude of the Schottky barrier height (Φ_B) and is described by the Schottky-Mott model, as shown in equation 2.1:

$$\Phi_B = \Phi_{metal} - \chi_{semiconductor}, \quad \text{(eq. 2.1)}$$

In equation 2.1, Φ_{metal} is the metal work function and $\chi_{semiconductor}$ is the semiconductor electron affinity. In general, a large Φ_B leads to schottky contacts. Previous work identify metal contacts to single-crystalline and polycrystalline SiC as schottky and ohmic, respectively [44–46]. The ohmic behavior observed with polySiC is attributed to defects and film characteristics such as roughness [2,47].

In this work, the as-deposited metal on polySiC forms an ohmic contact. The resistance of the contact depends on the contact resistivity and contact area. However, measuring contact resistance can be convoluted with semiconductor voltage drops across the contact area and parasitic resistance from probes. Implementation of circular transmission line method (CTLM) structures not only mitigates the above concerns, but also simplifies fabrication. The circular geometries require only one metal layer and avoid patterning of current-confining structures in SiC as would be necessary for rectangular geometries [48].

The layout and geometry of the CTLM structures have been reported previously [10, 14]. In general, circles with set radius (r_0) and varying gap thickness (d) serve as structures for contact resistivity measurements (Figure 2.1). The contact resistivity (ρ_c) can be experimentally determined by modeling resistance obtained from CTLM structures for $d \ll r_0$ using:

$$R = R_s/2\pi r_0 \times r_0 \ln(1+d/r_0) + (Rs/\pi r_0)\, L_T, \quad \text{(eq. 2.2)}$$

where R_s is the sheet resistance and $L_T = \sqrt{(\rho_c/R_s)}$ [48].

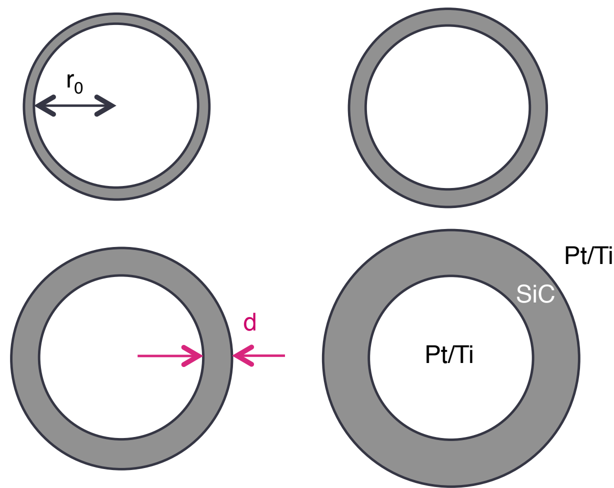

Figure 2.1. Schematic of CTLM structures and identification of materials and dimensions used for CTLM measurements.

2.3. Experimental section

Circular transmission line method is employed to study three different metallization stacks: (a) Pt(25 nm)/Ti(5 nm)/SiC, (b) Pt(25 nm)/Ti(5 nm)/NCG/SiC, and (c) Al_2O_3(10 nm)/Pt(25nm)/Ti(5nm)/NCG/SiC (Fig. 2.2). Stack (a) is prepared as a reference and contains as-deposited n-type polySiC with Pt/Ti electrodes on top. Stack (b) contains NCG, and stack (c) contains NCG and an additional top layer of alumina protection.

2.3.1. Polycrystalline n-type 3C-SiC deposition

In all cases, the substrates are Si (100) with 2 µm AlN, deposited via reactive sputtering [37,49]. Aluminum nitride is a good substrate for growing high quality polySiC films due to its low lattice-mismatch (1%) and similar thermal expansion coefficient with SiC [37]. In addition, AlN serves as an insulating layer to reduce leakage current between the SiC film and the Si wafer at high temperatures. Polycrystalline 3C-SiC is deposited onto AlN/Si substrates using low-pressure chemical vapor deposition (Thermo Electron Corporation, Lindberg BlueM, HTF55122A) with 7 sccm methyltrichlorosilane (MTS, Sigma-Aldrich, 99%), 70 sccm hydrogen (H_2, Praxair, 99.99%), and 0.015 sccm ammonia (NH_3, 5% in hydrogen) as the precursor, carrier, and n-type dopant gases, respectively. All polySiC films are grown for 30 min at 1200 °C and 1.4 Torr to yield a deposited SiC film ~300 nm in thickness with a film resistivity of 0.015 Ω-cm.

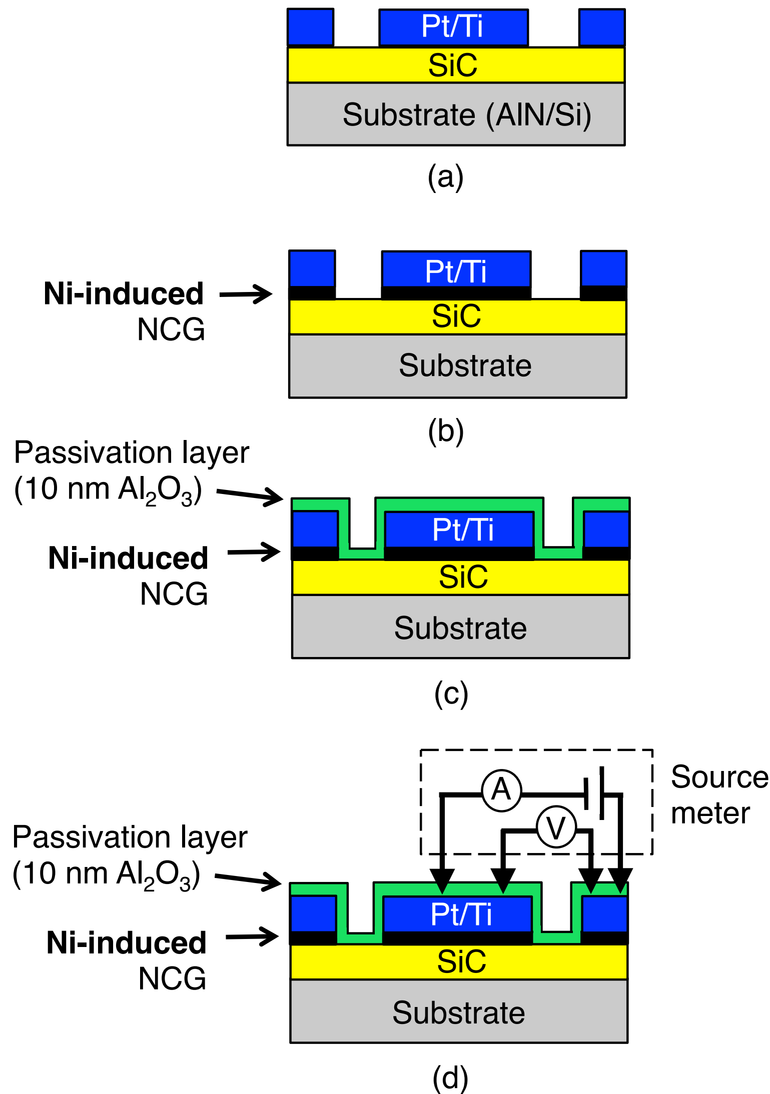

Figure 2.2 Three different contact stacks investigated: (a) Pt(25 nm)/Ti(5 nm)/SiC, (b) Pt(25 nm)/Ti(5 nm)/NCG/SiC, and (c) Al_2O_3(10 nm)/Pt(25 nm)/Ti(5 nm)/NCG/SiC. (d) Testing setup. For stack (c), probes penetrate through the Al_2O_3 layer.

2.3.2. Ni-induced graphitization

SiC/AlN/Si samples are dipped in hydrofluoric acid (HF) to remove surface oxide, followed by a quick water rinse. For stacks (b) and (c), a 20 nm thick layer of Ni is evaporated (VE100, Themionics Lab Corporation) onto SiC. The Ni/SiC/AlN/Si samples are then annealed to 1100 °C in H_2 at 4.3 Torr for 10 min using a horizontal hot-wall tube furnace (Thermo Electron Corporation, Lindberg BlueM, HTF55122A). After annealing, the samples are cooled quickly (~200 °C/min) to form NCG and nickel silicide. The nickel silicide and residual unreacted nickel

are removed by successive dips in HF/HNO_3 (1:3 in volume) and aqua regia. The presence of SiC, NCG, as well as the removal of nickel silicide is confirmed by Raman spectroscopy (JY HORIBA Labram, 632.817 nm excitation).

2.3.3. Fabrication of circular transmission line method structures

A standard lift-off process is used to pattern the CTL electrodes, which consist of an evaporated stack of Ti (5 nm) adhesion layer and Pt (25 nm). The NCG between the electrodes is removed with oxygen plasma (Plasma-Therm PK-12) created with 80 sccm O_2 at 80 W for 20 min.

The layout and geometry of the CTL have been reported previously [34,44]. Circles with a set radius (r_0 = 250 μm) and varying gap thicknesses (d = 5, 10, 15, 20 μm) are fabricated and serve as structures for contact resistivity measurements.

2.3.4. Alumina deposition

For stack (c), an alumina layer of 10 nm in thickness is deposited on top of the CTL structures via atomic layer deposition, ALD (Oxford FlexAl-Plasma Enhanced) at 300 °C and using trimethylaluminum and water as precursors. Figure 2.1d shows the I-V measurement setup, using tungsten probes and a source meter (Keithley 2400). The tungsten probe tips are able to penetrate the alumina layer in stack (c), eliminating the need for another photolithographic step to open up regions of the alumina layer. In addition, in penetrating the CTL pad, the alumina in the gap of the CTL structure is not disturbed, which is of key importance to protecting the NCG from oxidation.

2.3.5. Long-term stability testing

For the long-term stability tests, samples from the three stacks are exposed to 450 °C for a given time duration. All thermal exposures are done in a horizontal hot-wall tube furnace (Thermo Electron Corporation, Lindberg BlueM, HTF55122A) with both ends of the quartz tube open to air. After thermal exposure, samples are removed from the tube furnace for CTL measurements at room temperature. The measurements are repeated until contact resistivity dramatically increases or the sample reaches a thermal exposure time of 500 h.

2.4. Effect of nickel-induced nanocrystalline graphitic (NCG) interlayer formation on Pt/Ti contact to n-type 3C-SiC

Typical Raman spectra of Ni-induced NCG grown for stacks (b) and (c) show the characteristic graphitic carbon peaks, namely, D peak at 1330 cm^{-1}, G peak at 1580 cm^{-1}, and 2D peak at 2650

cm^{-1} (Figure 2.3). The ratio of the D to G peak intensities (I_D/I_G) provides an estimate of the average grain size [50]. The I_D/I_G ratio of the Ni-induced NCG is ~0.8. For comparison, the graphitic peaks of previously reported NCG obtained by UHV annealing of SiC is also shown in Figure 2.3 and has an I_D/I_G ratio of ~2.2 [34]. A larger I_D/I_G ratio corresponds to smaller average grain size, which in turn is an indication of increased structural defects. In addition, the positions of the D, G, and 2D Raman peaks of the Ni-induced NCG match well with the values reported in Pimenta et al. [51], and do not exhibit the stress-induced blue shifts typical of thinner UHV-produced NCG [34,52].

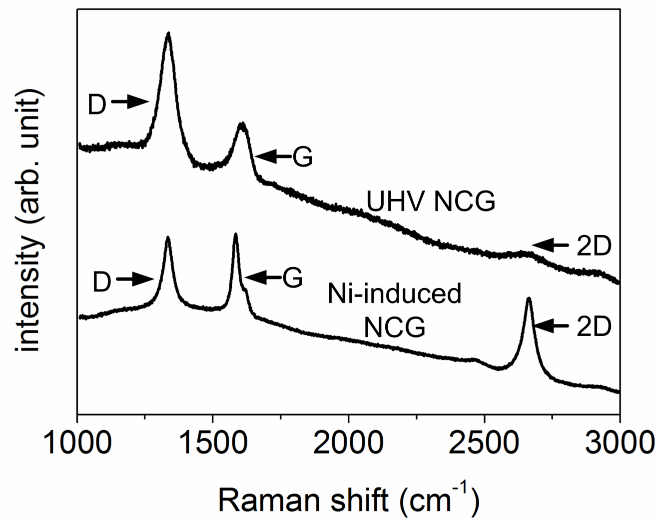

Figure 2.3. Raman spectra of UHV graphitized and Ni-induced graphitized poly-SiC. The UHV annealed NCG is obtained by the same method reported in Vincent et al. [34].

2.5. Effect of Ni-induced NCG and Al_2O_3 overlayer for a stable low resistivity contact between Pt/Ti and n-type 3C-SiC

The contact resistivity is calculated from the current-voltage (I-V) characteristics obtained from the CTL devices with varied gap distances [48]. All stacks, as fabricated, show ohmic contact behavior. The initial contact resistivity for all three stacks prior to thermal treatments is on the order of 10^{-4} Ω-cm^2. After exposing the stacks to 450 °C, stack (a) proved least reliable, whereas stack (c) was the most reliable (Figure 2.4). The contact resistivity of stack (a) degrades within the first 10 h, after which a contact resistivity could not be extracted due to electrical property degradation of the contact.

Stack (b), Pt/Ti/NCG/SiC, maintains low contact resistivity for a longer period than stack (a). The stability improvement seen in stack (b) is attributed to the introduction of NCG, which prevents Pt silicide formation, as has been reported previously being essential in maintaining the

contact stability [34,44]. The enhanced contact property of stack (b) is evident through comparison; stack (b) has a contact resistivity that is consistently below 0.01 Ω-cm^2 for the first 80 h, while with the equivalent structure obtained with UHV annealed NCG has a contact resistivity that exceeds 0.01 Ω-cm^2 after only 5 h of testing [34]. This difference is likely due to decreased structural defects (as evidenced by larger I_D/I_G ratio) and increased thickness, which in turn serves as a more efficient reaction barrier between the metal and SiC.

As for stack (c), which is protected from oxidation with an alumina layer, its contact resistivity remains on the order of 10^{-4} Ω-cm^2 for the entire duration of the test (500 h). The degradation of stack (b) during the testing is likely due to the oxidation of the entire stack, especially within the NCG layer. The structural integrity of Ni-induced NCG before and after testing with metal layers removed is characterized by Raman spectroscopy (Figure 2.5). After long-term testing, stack (b) no longer shows the presence of any NCG, which is in accordance with results concerning UHV-graphitized contacts, and can be attributed to its oxidation during the high temperature exposure to air [34]. On the other hand, the 10 nm alumina layer used in stack (c) preserves the NCG layer, maintaining a stable contact.

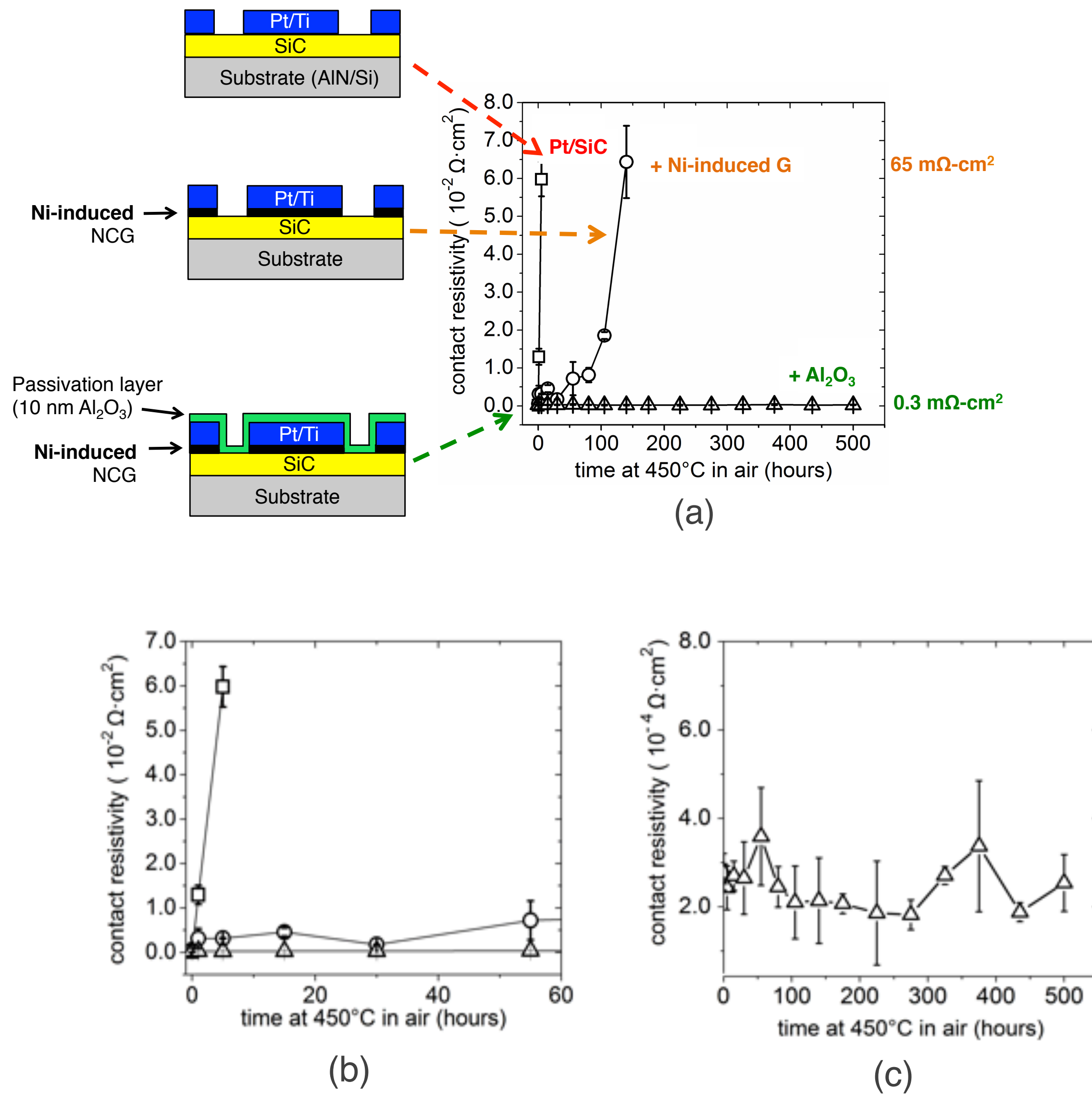

Figure 2.4. Contact resistivity as a function of time exposed to 450 °C in air for stack a (square), stack b (circle), and stack c (triangle). (a) Five hundred hours of thermal exposure with schematic of different stacks. Numbers on the secondary y axis correspond to averaged contact resistivity measured for stack b in orange and stack c in green; (b) zoomed-in data from the first 60 h of thermal exposure; and (c) zoomed-in data obtained from stack c after 500 h of thermal exposure.

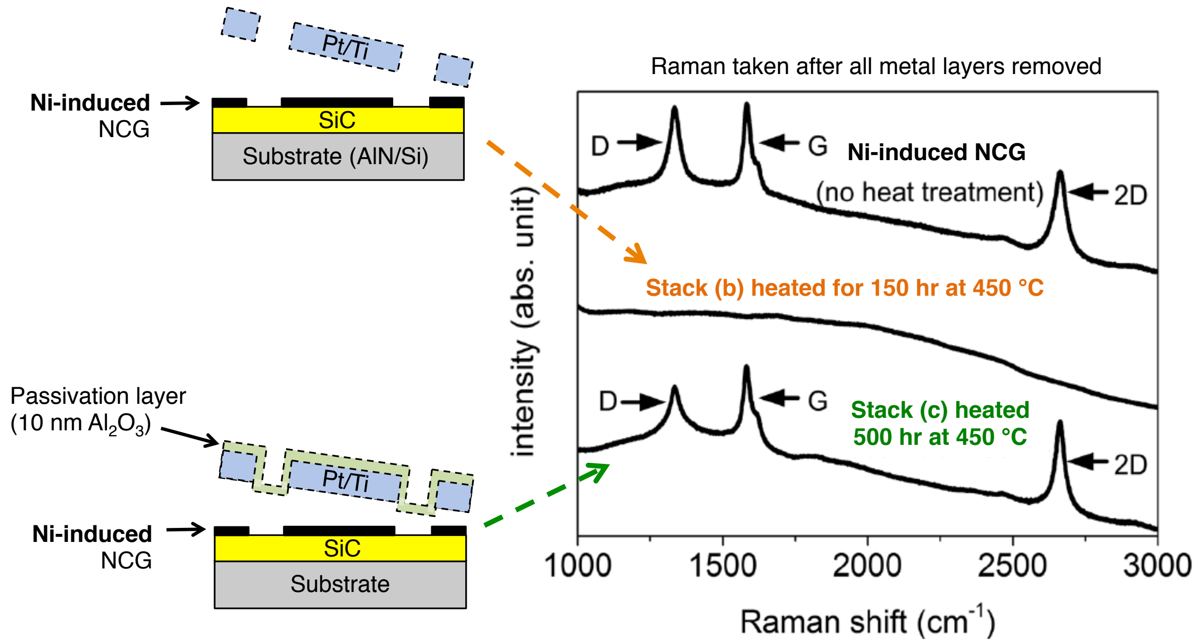

Figure 2.5. Raman spectra of the CTL devices designed with Ni-induced graphitized poly-SiC after removal of all metal layers. For reference, NCG obtained from Ni-induced graphitization without heat treatment is shown. NCG of stack (b) is completely removed after 150 h at 450 °C. NCG of stack (c) is intact after 500 h at 450 °C.

2.6. Summary

A Ni-induced nanocrystalline graphitic layer is used as a reaction barrier between Pt/Ti and SiC to maintain low contact stability at elevated temperatures in air. The Ni-induced NCG is thicker, has a lower compressive strain [52], and has fewer defects compared to previously published NCG obtained by UHV annealing of SiC. The Pt/Ti/NCG/SiC contact is further protected with an ALD alumina layer to prevent oxidation of the graphitic layer, and shows improved stability after 500 h of testing at 450 °C. In this metallization scheme, the graphitic layer plays a key role in maintaining low contact resistivity and the fabrication process presented here offers the advantage of easier manufacturability with respect to previously reported annealing in ultrahigh vacuum.

3. Nickel-induced silicon carbide nanowire growth on silicon carbide

The growth of silicon carbide (SiC) nanowires on 4H-SiC (0001) substrates via metal-catalyzed chemical vapor deposition is investigated. The process employs a 2-nm Ni film and methyltrichlorosilane (MTS) precursor in hydrogen carrier gas. Silicon carbide growth is observed at temperatures as low as 900 °C. Growth at 950 °C yields vertically aligned nanowires with 4H-like crystal structure and high aspect ratios. Higher growth temperatures result in decreased nanowire aspect ratio and reduced crystalline disorder.

Focusing on the growth at 950 °C, annealing a 2 nm nickel film in hydrogen gas and in the absence of MTS leads to the formation of embedded, hexagonally shaped Ni_2Si clusters surrounded by excess carbon. These Ni_2Si clusters, present prior to the introduction of MTS precursor, alone catalyze the nanowire growth and its 4H-like crystal structure. Without these clusters present, growth yields a 3C-SiC thin film. The key findings discussed shed light on the role of temperature and catalytic activity of Ni_2Si towards tailored nanowire morphologies and targeted crystallinity for device applications.

3.1. Introduction to metal-catalyzed semiconductor nanowire growth

Identifying the growth mechanism of CVD-grown semiconductors enables better control of nanowire growth and resulting properties for use in academia and industry. However, identification of the growth mechanism requires advanced microscopy to monitor the nanowire growth in-situ. For the SiC nanowires grown in this work, the corrosive gaseous precursors and high nanowire growth temperature (950 °C) prevent implementation of common in-situ methods, as the growth process would damage the equipment. Nonetheless, studies have shown that in general semiconducting nanowires are most commonly grown via vapor-liquid-solid (VLS)

mechanism, and possibly via vapor-solid-solid (VSS) depending on growth conditions [53]. VLS growth involves heating a deposited metal catalyst film on a substrate to form liquid droplets. Heating above the eutectic temperature allows alloy droplets to form. Upon precursor gas introduction the droplets become supersaturated with components from the vapor phase, precipitating out a single-crystalline wire [54]. Examples of semiconductor/catalyst nanowire systems utilizing this method include Si/Au [54], GaAs/Au [55], Ge/AuGa and Si/AuGa [56]. To confirm the VLS mechanism, the liquid droplet is visible on the nanowire tip during and after nanowire growth via in-situ transmission electron microscopy (TEM) [57]. VSS follows the same general process of VLS except the alloy catalyst is solid instead of liquid or nanowire growth occurs below the eutectic temperature. As Kodambaka et al. pointed out, there are several semiconductor/catalyst nanowire systems that can grow below its eutectic temperature, such that the alloy remains solid during nanowire growth. Examples of such nanowire/catalyst systems include Si/Al [58], Si/Ti [59], Ge/Au [53,60], and InAs/Au [61,62]; researchers have ruled out eutectic point depression [63] and affirmed that the catalyst is solid [64].

3.2. SiC nanowires on SiC substrates

The intrinsic physicochemical stability of SiC enables a robust material platform for the realization of devices that can operate in extreme environments, where more conventional semiconductor materials, such as Si, would fail. The added high surface area advantage of SiC nanowires provides a robust platform for biological sensors [18,65,66], field emission cathodes [19,20], and energy storage devices [22,23,67].

For such nanowire-based devices, the nanowires must either be transferred or grown directly on the device substrate. A common substrate for growth of SiC nanowires is single-crystalline Si [68–72]. However for harsh-environment devices, growth directly on substrates compatible with harsh-environment operating conditions eases fabrication by eliminating a transfer step. For a robust monolithic platform, SiC nanowires can be grown on single-crystalline 4H-SiC (0001) substrates to uniformly produce either cubic [8,73] or hexagonal SiC nanowires [9]. Although 4H-SiC is the industry standard for SiC substrates, a few studies show growth of SiC nanowires on 6H-SiC [74,75]. Aside from choosing a robust substrate, an additional interest is for vertical nanowire arrays that can guide cells [76] and electrons [77], function as vertical field effect transistors [78], and facilitate low-power electronics [79].

Here we report the effect of growth temperature on Ni-catalyzed chemical vapor deposition of SiC nanowires on 4H-SiC (0001) substrate. The growth temperature is identified as a way to optimize the morphology and crystallinity of the nanowires. The growth of vertically aligned 4H-like silicon carbide nanowire array is demonstrated. Additionally, we report on the role of Ni on SiC polytype deposition and discuss the morphology of nickel silicide clusters formed upon annealing Ni on SiC prior to the initiation of SiC growth. The results of this study serve to accelerate the adoption of SiC nanowires as a material platform for harsh-environment applications by addressing the role of temperature and catalyst in nanowire growth.

3.3. Experimental section

A general process flow for nickel-induced SiC nanowire growth studied in this dissertation is shown in Figure 3.1.

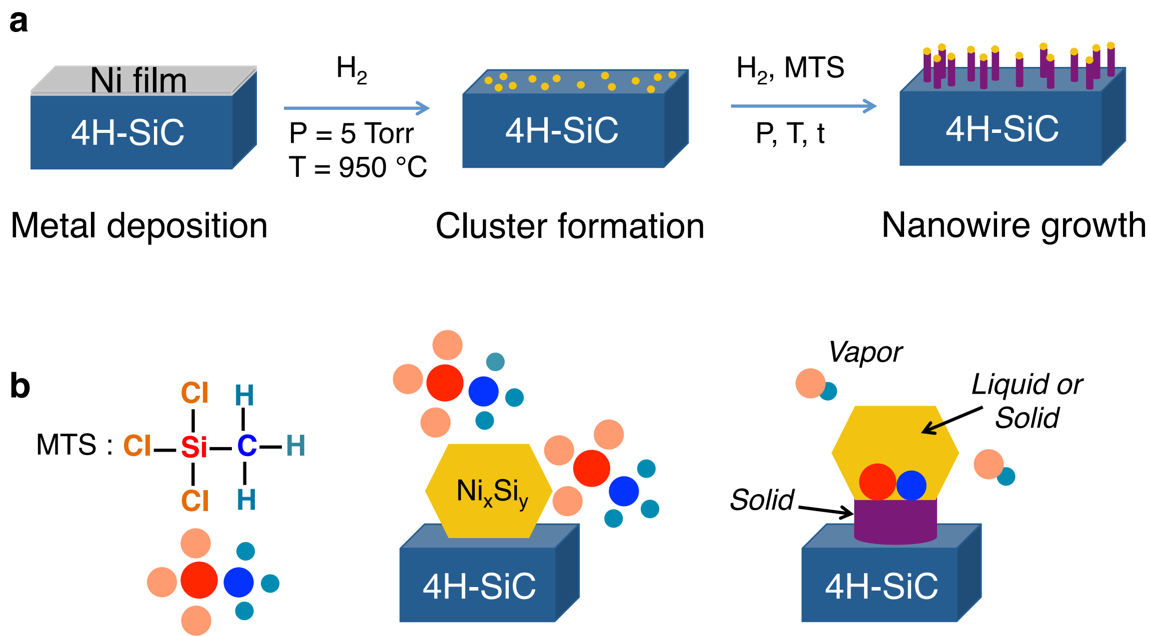

Figure 3.1. Chemical vapor deposition (CVD) metal-assisted nanowire growth. (a) A thin Ni film (~2 nm) is deposited via electron beam evaporation. A metal alloy is formed upon annealing to nanowire growth temperature. Nanowire growth begins upon introduction of the gaseous precursor methyltrichlorosilane (MTS). (b) MTS has a 1:1 ratio of Si and C atoms. MTS decomposes at the catalytic site, injecting Si and C atoms that supersaturate the catalyst, leading to the precipitation of solid SiC nanowire.

3.3.1. As-received 4H-SiC (0001) substrates

SiC nanowires were grown on research-grade n-type 4H-SiC (0001) substrates with 4° off-axis cut towards <1120> (Cree Research). The as-purchased SiC wafer was diced into 10 mm x 10 mm coupons. Prior to use, substrates were sonicated for 5 min in separate baths of acetone and isopropanol, and cleaned for 5 min in an ultra-violet ozone cleaner, followed by 10 s rinses in hydrofluoric (HF) acid and distilled water, and dried with N_2 gas.

As the substrate surface may play a role in epitaxial growth, the roughness and doping concentration were quantified. The as-received substrate has root mean squared roughness of 0.8

nm ± 0.2 nm and has scratches on the surface from chemical mechanical polishing (Figure 3.2a). To evaluate the doping concentration, the longitudinal optical phonon plasmon coupled (LOPC) signal was acquired with Raman spectroscopy from cleaned, bare substrates with no heat treatment. Following Harima et al. [80], the doping concentration is calculated to be 1.8×10^{18} cm^{-3} (Figure 3.2b and Table 3.1). This is further confirmed with the linear empirical relationship between carrier concentration, n, and the LOPC mode, as shown in equation 3.1:

$$n = 1.25\times10^{17}\ cm^{-3} \times \Delta\omega, \qquad \text{(eq. 3.1)}$$

where $\Delta\omega$ is the difference between the LOPC mode and bare LO phonon frequency in 4H-SiC [81]. This relationship yields a value of 1.3×10^{18} cm^{-3} for carrier concentration. In Section 3.8, this estimated doping concentration will be compared to another commercially available 4H-SiC (0001) substrate (SiCrystalAG).

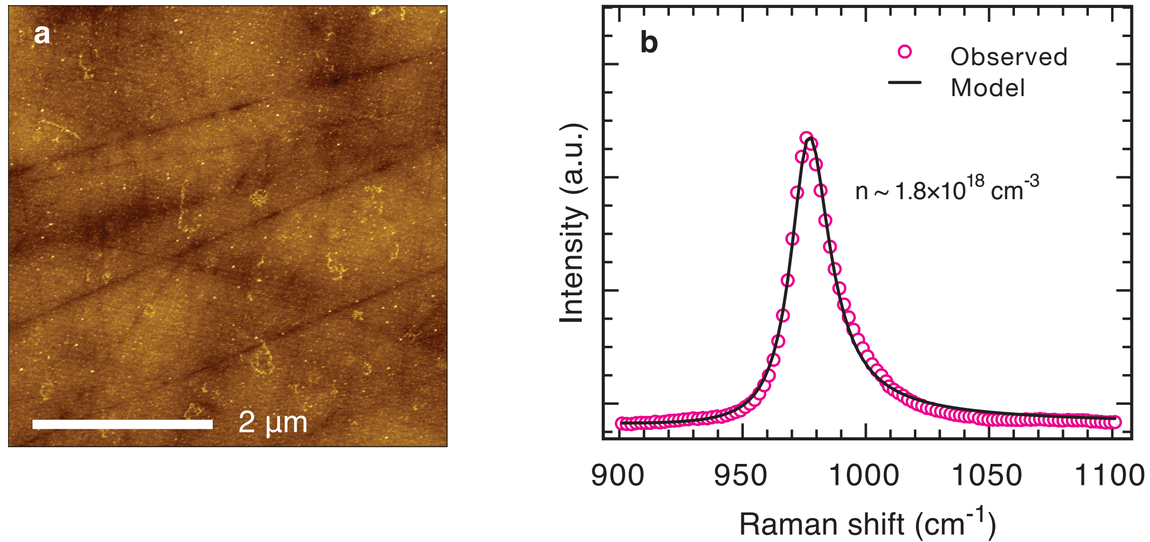

Figure 3.2. 4H-SiC (0001) substrate as received. (a) Atomic force micrograph of as-received 4H-SiC(0001) substrates. The z-scale ranges from -4 nm (black) to 4 nm (gold). Negative z value represents depth into the substrate. (b) Doping concentration of substrate estimated by LOPC Raman line shape.

Table 3.1. Fitted and calculated parameters from LOPC line shape shown in Figure 3.2.

		4H-SiC (0001) substrate (Cree)
Fitted parameters	Plasmon frequency, ω_P (cm^{-1})	271
	Plasmon damping constant, γ (cm^{-1})	312
	Phonon damping constants, Γ (cm^{-1})	11.4
Calculated parameter	Doping concentration, n (cm^{-3})	1.8×10^{18}

3.3.2. Nanowire synthesis and characterization

Thin nickel films (~2.6 nm) were deposited onto SiC substrates via electron beam evaporation (Thermionics VE-700 Vacuum Evaporator) of a nickel source (Alfa Aesar, 99.995%) at an operating pressure of 2×10^{-6} Torr. Substrates with evaporated nickel were sealed in a hot-wall chemical vapor deposition (CVD) tube furnace (Thermo Scientific Lindberg Blue M) and heated to growth temperature at a rate of 44 °C/min at 5 Torr under 10 sccm H_2 (Praxair, 99.99%). For the analysis of the surface prior to the initiation of the nanowire growth, the samples were maintained for 10 min at high temperature and then cooled to room temperature at a rate of 22 °C/min under H_2 ambient. For SiC nanowire growth, once the furnace reached growth temperature, 0.5 sccm methyltrichlorosilane (MTS, Sigma-Aldrich, 99%) was introduced for a specific length of time, after which the MTS was turned off and samples were cooled to room temperature at a rate of 22 °C/min under 10 sccm H_2.

Hydrogen annealing Ni-on-SiC produces nickel silicide and carbon at the surface of the SiC substrate. To assess the effect of carbon produced, it was removed with a 10 min oxygen plasma treatment. The oxygen plasma was generated with 50 W radio frequency at approximately 200 mTorr. To assess the role of nickel silicide formed during annealing, it was removed through two 5-second rinses in a 3:1 volume ratio of nitric acid (HNO_3) to hydrofluoric acid (HF) and a 3:1 volume ratio of HNO_3 to hydrochloric acid (HCl). The etch procedures were tested for selectivity using Raman spectroscopy and it was found that the silicide etch did not remove carbon and the carbon etch did not remove silicide.

Samples were characterized by scanning electron microscopy (SEM, Zeiss Gemini Ultra-55, accelerating voltage set to 2kV), tapping mode atomic force microscopy (AFM, Digital Instruments Nanoscope IIIa), Raman spectroscopy (Horiba Jobin Yvon LabRam, excitation line provided by a HeNe laser at 632.8 nm, through a 100X objective with 0.8 numerical aperture),

and X-ray diffraction (Bruker, AXS D8 Discover GADDS, operated at 40 kV and 20mA at the wavelength of Cu Ka).

High-resolution compositional analysis on NWs was performed by Dr. Burak Ozdol by means of energy dispersive X-ray spectroscopy (EDS) using FEI Titan 60-300 transmission electron microscope (TEM) equipped with a field emission electron source and four-quadrant silicon-drift detectors (Super-X, high collection efficiency < 0.9 sr solid angle). Simultaneous high-angle annular dark-field scanning TEM (STEM) images were acquired using 1 nm probe size at 200 kV acceleration voltage. Elemental maps were derived using Bruker's ESPRIT software.

3.4. Effect of growth temperature

Growth temperature is used to target SiC nanowire dimensions and crystallinity. Figures 3.3a-e are representative cross-sectional SEM images of SiC structures obtained at 900, 950, 1050, and 1150 °C after 64 minutes of growth time. The average nanowire diameters and lengths at these growth temperatures are plotted in Figure 3.3f. At low growth temperatures (900 °C and 950 °C) minimal deposition occurs on the nanowire sidewall, resulting in nanowire length to diameter ratio (aspect ratio) close to 100. Increasing temperature to 1050, 1100, and 1150 °C drastically decreases the aspect ratio to 62, 19, and 4, respectively. At higher growth temperatures, such as 1150 °C, the vapor-solid (VS) deposition of SiC on the sidewall dominates and produces SiC structures with smaller aspect ratios (Figure 3.3e).

Increasing the growth temperature from 900 to 1150 °C increases nanowire crystallinity, as evidenced by the reduction in the disorder-induced longitudinal optical (LO) phonon band between 835 and 970 cm^{-1} [82]. Additionally, the transverse optical (TO) phonon peaks at 764, 780, and 796 cm^{-1} (Figure 3.3g) become sharper; the peak location is very close to the position of the dominant TO peak in the 2H, 4H, and 3C polytypes, respectively. As the temperature approaches 1200 °C, higher quality 3C-SiC or 4H-SiC is expected [37,83]. Accordingly, nanowires grown at 1150 °C exhibit more distinct phases that encompass such hexagonal and cubic stacking patterns. Regardless of growth temperature, all SiC nanowires exhibit predominantly a 4H-like crystal structure, elaborated in Chapter 4.

In targeting specific crystalline or morphological properties, temperature must be optimized to strike a balance between nanowire aspect ratio and crystalline disorder (Figure 3.3f,g). Given the aspect ratio of 100 and the sharpness of the Raman signal, nanowires grown at 950 °C are of interest. To understand growth at 950 °C, catalyst evolution, crystallinity and morphology is also studied.

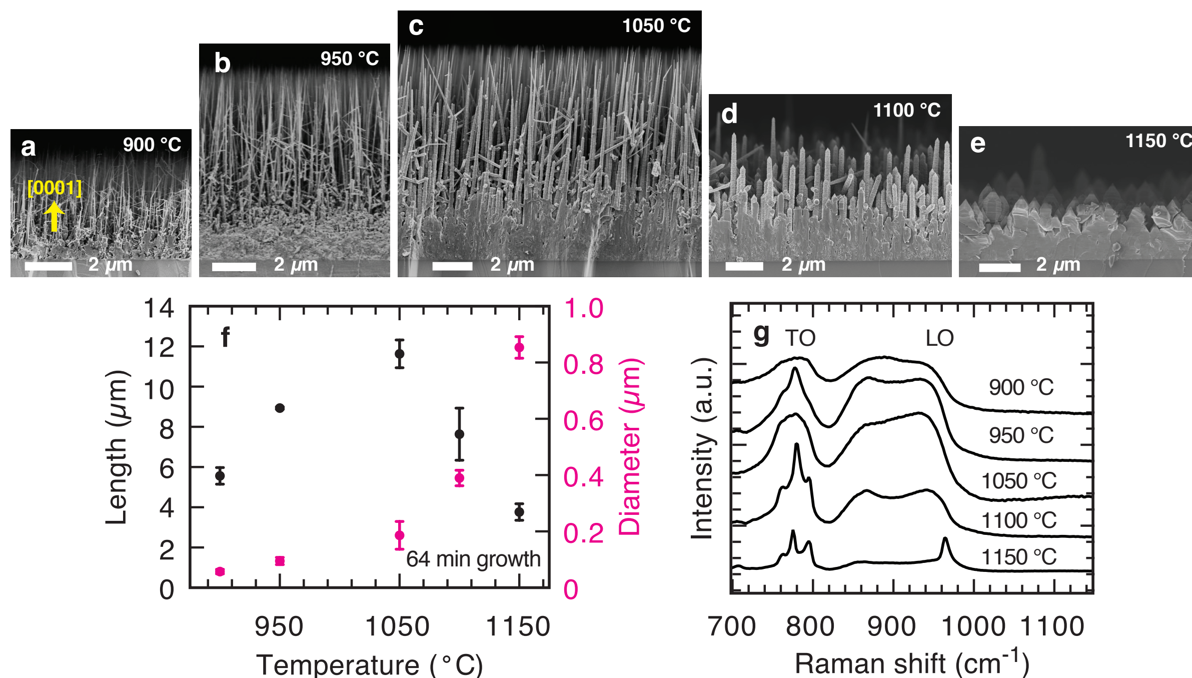

Figure 3.3. Growth temperature affects nanowire morphology and crystallinity. (a-e) Cross-sectional SEM images of nanowires grown at 900, 950, 1050, 1100, and 1150 °C for 64 min growth. (f) Averaged nanowire length and diameter vs. growth temperature. (g) Raman spectra obtained on samples grown at various temperatures.

3.5. Catalyst composition

Characterization of nanowires as a function of growth time is used to shed light on the growth mechanism. Figure 3.4 shows representative SEM images of the nanowires after 2 and 64 minutes of growth. After short growth times (2 min), the catalytic clusters are clearly visible at nanowire tips. Energy dispersive x-ray spectroscopy analysis performed on the catalyst at a nanowire tip yields a composition of 66.3 ± 2.5 at% Ni and 33.7 ± 0.3 at% Si, indicative of Ni_2Si (Figure 3.4c,d). After longer growth times (64 min), the cluster is no longer visible, likely due to etching by hydrochloric acid, a byproduct of the MTS decomposition reaction (Figure 3.4b). The reduction of cluster size due to hydrochloric acid, along with slow sidewall deposition, may be responsible for the nanowires tapering with longer growth times.

Prior to MTS introduction, as the temperature is raised, agglomerated nickel silicide clusters form and serve as catalytic sites for nanowire growth. AFM of annealed samples reveal clusters across the 4H-SiC surface. Figure 3.5 shows the clusters located across five different areas of 5 μm × 5 μm. Raman spectrum of Ni-on-SiC samples annealed at 950 °C in hydrogen show the presence of nickel silicide, specifically Ni_2Si (137 cm^{-1}), and carbon (1330 cm^{-1}) signals (Figure 3.6a). The Raman laser spot size is ~1 μm and collects data from an area spanning several

clusters. Although the Ni/SiC samples were annealed in hydrogen ambient (5 Torr) with 2 nm Ni film on SiC substrate, our findings are consistent with the literature, where Ni_2Si formation and carbon precipitation is seen after vacuum annealing of thicker Ni films (>50 nm) on SiC [84–86].

The hexagonal-shaped clusters visible after annealing Ni-on-SiC samples at 950 °C are identified as Ni_2Si through a series of etch steps (Figure 3.6a,b). First, the annealed Ni/4H-SiC was treated with oxygen plasma for 10 min, which is known to be an effective means for removing carbon [87]. Inspection of the Raman spectrum after plasma confirmed removal of the C footprint, while preserving the Ni_2Si signal at 137 cm^{-1}. Correspondingly, the hexagonal-like clusters were still visible with SEM; upon closer inspection, oxygen plasma removes wave-like features likely from C, resulting in a crisper micrograph (Figure 3.6b).

Second, the annealed Ni/4H-SiC treated with oxygen plasma was placed in acid baths of HNO_3:HF and HNO_3:HCl for 5 seconds etch to remove nickel silicide (Figure 3.7). Both rinses are oxidizing acid mixtures that have been shown experimentally to remove nickel silicides [84,88]. Inspection of the Raman spectrum after the acid etch confirmed removal of Ni_2Si, leaving behind bare SiC. Micrographs of acid-treated samples show structured hexagonal pits within the SiC substrate. The substrate pitting occurs from Si atoms in the SiC substrate reacting to form Ni_2Si with the deposited Ni thin film; this surface interaction results in Ni_2Si clusters with a mean equivalent disc radius of ~50 nm and a mean height of ~9 nm (Figures 3.6c,d). The shape of the pit depends on Si atom arrangement within the plane exposed to the Ni thin film. In this work, the hexagonal (0001) closed-packed plane, equivalent to the cubic (111) closed-packed plane, has Si atoms arranged in hexagons relative to each other. Thus, in agreement with the orientation of exposed Si atoms in the SiC substrate, we observe hexagonal pitting on the 4H-SiC (0001) surface.

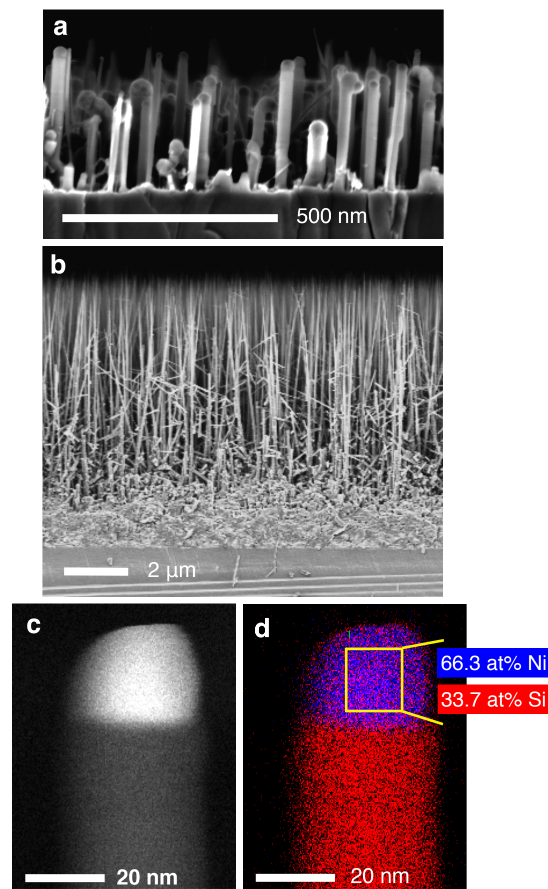

Figure 3.4. 4H-like SiC nanowires grown on 4H-SiC (0001) at 950 °C. (a) Cross-sectional SEM after 2 min of growth. (b) Cross-sectional SEM after 64 min of growth. (c) STEM image of nanowire grown for 30 min. (d) EDS of nanowire shown in c reveals Ni_2Si at nanowire tip.

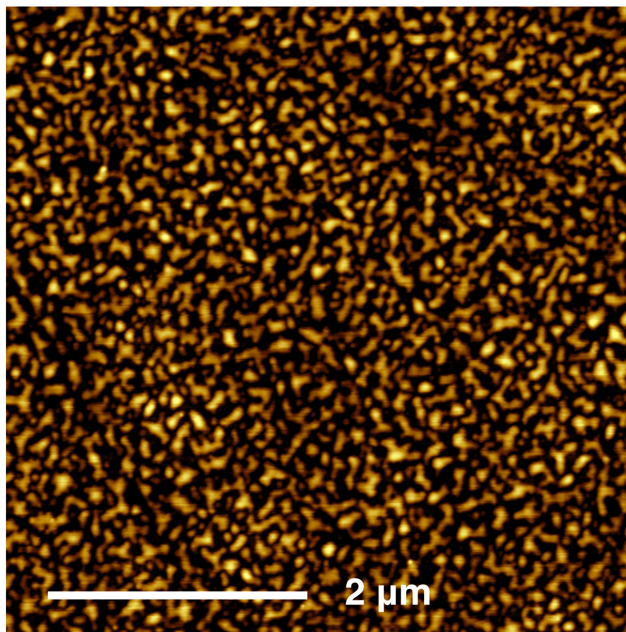

Figure 3.5. Representative AFM image of nickel silicide clusters formed after annealing 2 nm Ni on 4H-SiC for 10 min at 950 °C at 5 Torr (z range of 16 nm).

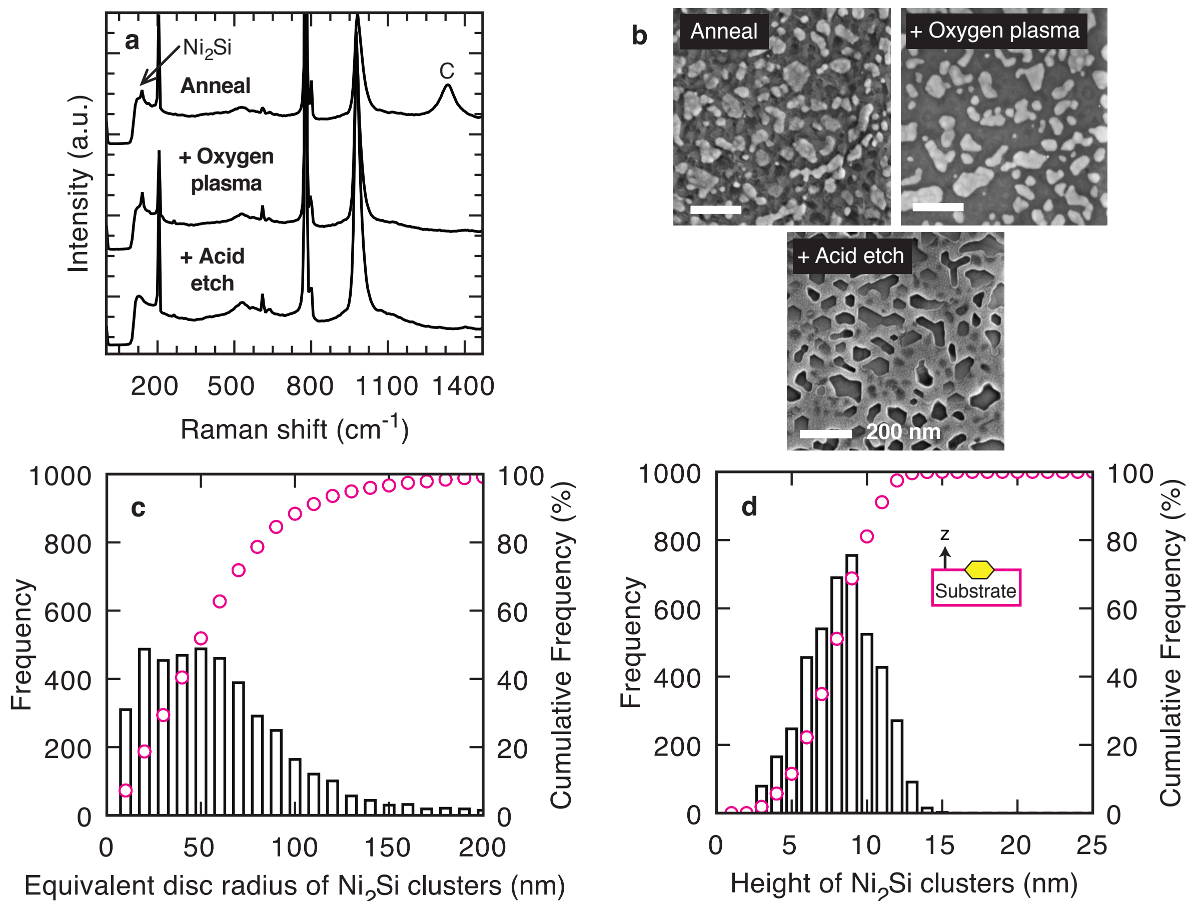

Figure 3.6. Characterization of nickel silicide clusters on 4H-SiC (0001). (a) Raman spectra of Ni/ 4H-SiC after annealing in H_2 for 10 min at 950 °C (top), with a subsequent oxygen plasma treatment (middle) and acid etch (bottom). (b) SEM images of annealed Ni/4H-SiC, annealed Ni/4H-SiC after subsequent C removal, and annealed Ni/4H-SiC after C and Ni_2Si removal. (c) Distribution of equivalent disc radii of Ni_2Si clusters. (d) Distribution of Ni_2Si cluster height. The bar graphs correspond to the frequency counts shown on left y-axis. The circles correspond to the cumulative frequency % shown on the right y-axis. All scale bars are 200 nm. Height of Ni_2Si clusters are estimated using AFM images before and after removal of C and Ni_2Si shown in Figures 3.5 and 3.7.

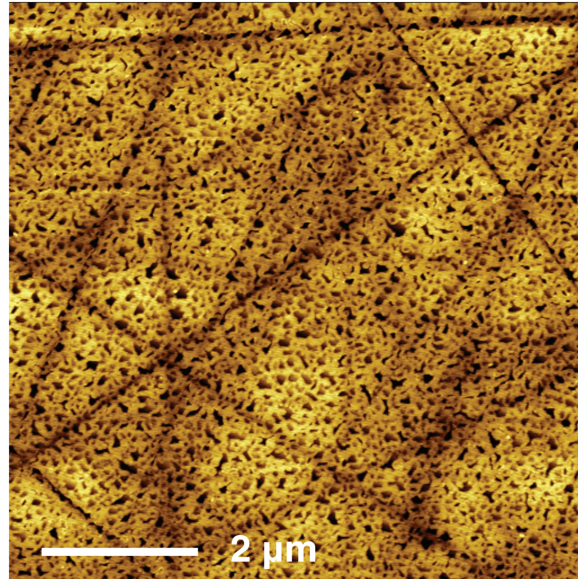

Figure 3.7. Representative AFM image of 4H-SiC (0001) after removing nickel silicide clusters (z range of 10 nm). Nickel silicide was removed with rinses in HCl:HNO_3 and HF:HNO_3. Nickel silicide clusters formed after annealing 2 nm Ni on 4H-SiC for 10 min at 950 °C at 5 Torr.

To characterize the nickel silicide formation on SiC further, a Ni volume analysis using the density and molecular weight of Ni, and the lattice parameters [89–91] of Ni_2Si in combination with topography information obtained with AFM was used to approximate the number of Ni atoms within the formed Ni_2Si clusters across a substrate area of 1.25×10^8 nm^2, based on five distinct 5 µm x 5 µm AFM images (Figures 3.5 and 3.7). The approximate number of Ni atoms within Ni_2Si clusters formed is 4.4×10^{10}. This compares well to the estimated number of deposited Ni atoms (3.0×10^{10}) within 2.6 nm of evaporated Ni film across the same substrate area and suggests that all nickel is consumed to form Ni_2Si during hydrogen anneal to 950 °C.

3.6. Effects of catalyst composition on SiC nanowire growth

Although Ni_2Si particles and excess C are both present before MTS introduction, Ni_2Si is identified as the primary site for nanowire growth. Selective etching of Ni_2Si clusters, leaving behind only C, results in no significant nanowire growth after 2 min (Figure 3.8a,b). On the other hand, removing excess C to leave behind only Ni_2Si (as shown in Figure 3.8a, middle spectrum) results in significant nanowire growth after 2 and 64 min (Figure 3.8c,d). The resulting nanowire arrays are very similar to the case without removing the excess carbon.

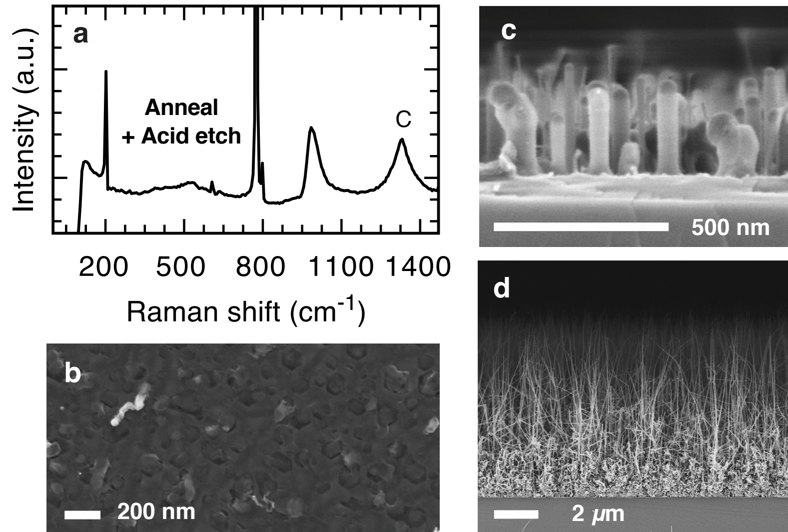

Figure 3.8. Ni_2Si is the primary site for nanowire growth. (a) Raman spectrum of annealed Ni/4H-SiC after an acid etch to remove Ni_2Si. (b) No nanowire growth with only C present before MTS introduction. (c, d) Cross-sectional SEM images of 2 and 64 min of growth with only Ni_2Si present before MTS introduction, respectively.

3.7. Catalyzed *vs.* uncatalyzed SiC growth

The growth conditions employed in this work show that Ni_2Si yields both nanowire and film growth, albeit at different rates. For example, a 2-μm thick film and 8-μm tall nanowires are grown simultaneously within 64 min (Figure 3.4b). This continuous film growth is attributed to catalyzed growth, since without deposition of a 2 nm Ni film, only sparse SiC clusters with diameters of ~200 nm are observed under the same conditions (Figure 3.9a,b). To characterize the polytype of the uncatalyzed film, Raman mapping in the z-direction is employed (Figure 3.9d). A scan from -15 μm to +15 μm, where z = 0 μm corresponds to the uncatalyzed film surface, reveals a region with increased signal from the 3C-SiC TO phonon mode (796 cm^{-1}) near z = 0 μm, suggesting that the film grown in the absence of Ni catalyst is predominantly cubic in structure. 3C-SiC heteroepitaxy on 4H-SiC has been attributed to the low temperature growth (800 °C) [83], but also shown at much higher growth temperatures as well (>1600 °C) [92]. In contrast, Ni-induced nanowire growth detailed in Chapter 4 results in predominantly hexagonal SiC, attributed to high supersaturation within the Ni_2Si catalyst. Without Ni present to form Ni_2Si clusters with low C solubility, a highly supersaturated state is not achieved, and cubic film growth ensues, according to established kinetic models [93].

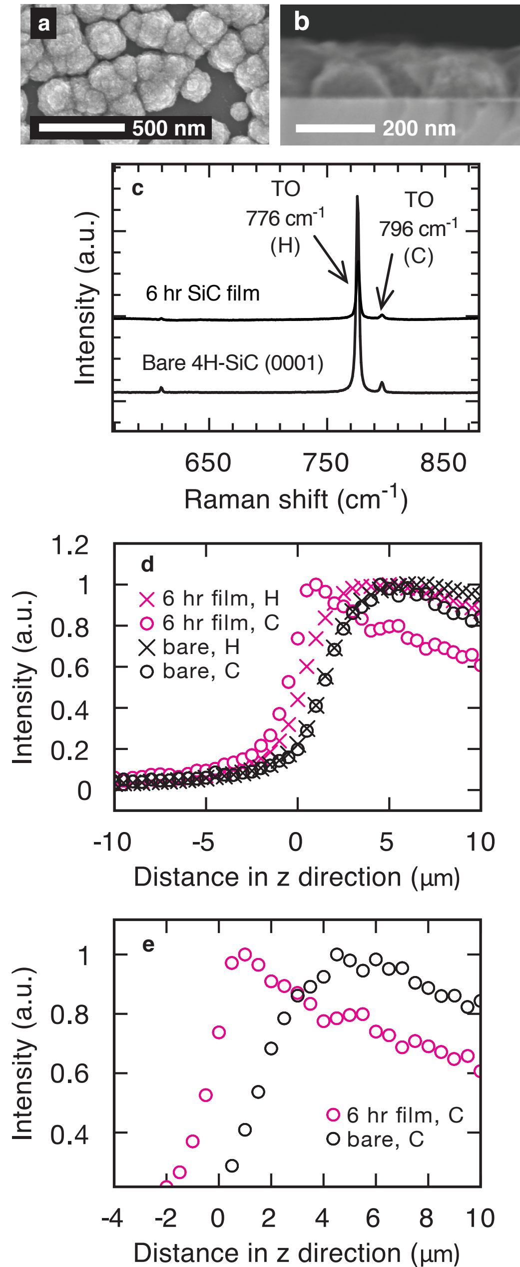

Figure 3.9. Effect of Ni on SiC deposition and polytype. (a) Top-view SEM image of 64 min growth without evaporated Ni thin film. (b) Cross-sectional, zoomed-in SEM image of clusters shown in (a). (c) Raman spectroscopy comparing uncatalyzed SiC film grown on 4H-SiC (0001) under nanowire conditions without Ni (top) and bare 4H-SiC (0001) substrate (bottom). (d-e) Raman z-maps of TO phonon modes positioned at 776 (triangles) and 796 cm^{-1} (circles) for bare substrate 4H-SiC (black, filled symbols) and 6 hr SiC film (magenta, open symbols). The positive z-direction corresponds to movement into the 4H-SiC (0001) substrate, with the film surface located at $z = 0$ μm.

3.8. Effect of substrate

The growth method employed here produces SiC nanowires on SiC substrates with crystal structures similar to the 4H polytype. Details concerning the 4H-like crystal structure classification are elaborated in Chapter 4. Comparison between two commercially available 4H-SiC (0001) substrates highlights differences in catalyst agglomeration and nanowire orientation. The following sections detail the effects of 4H-SiC substrates purchased from Cree Research and SiCrystalAG on nanowire growth. The two substrates will be distinguished by their surface roughness: smooth (purchased from Cree) and rough (purchased from SiCrystalAG). Nanowires grown on smooth and rough substrates produce 4H-like SiC growth (Figure 3.10).

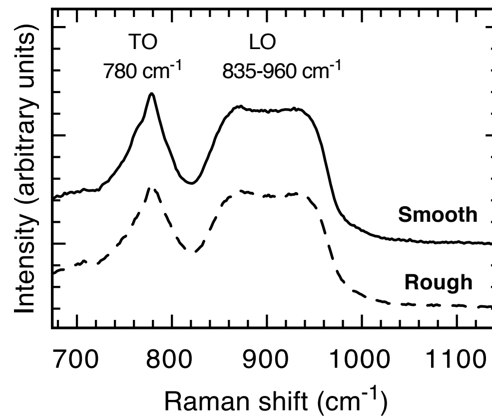

Figure 3.10. SiC nanowires grown on smooth (solid line, purchased from Cree Research) and rough (dashed line, purchased from SiCrystalAG) 4H-SiC (0001) substrates.

The smooth 4H-SiC(0001) substrates have a root mean squared roughness of 0.8 nm ± 0.2 nm and yield vertically aligned nanowires, evident at both at short and long growth times (Figure 3.4a,b). The same growth method and experimental set-up produces different wire orientations, depending on substrate. Contrary to the smooth substrates, the rough 4H-SiC (0001) substrates with a root mean squared roughness of 2.4 nm ± 0.2 nm yield nanowires that display 60° azimuth angles after short times and dense non-vertical growth after long times (Figure 3.11). This orientation difference underlines the importance of the substrate's surface quality. In addition to surface roughness, salient differences between these two substrates include doping concentration and catalyst agglomeration, determined by the line shape of the LO phonon plasmon coupled (LOPC) mode and microscopy, respectively.

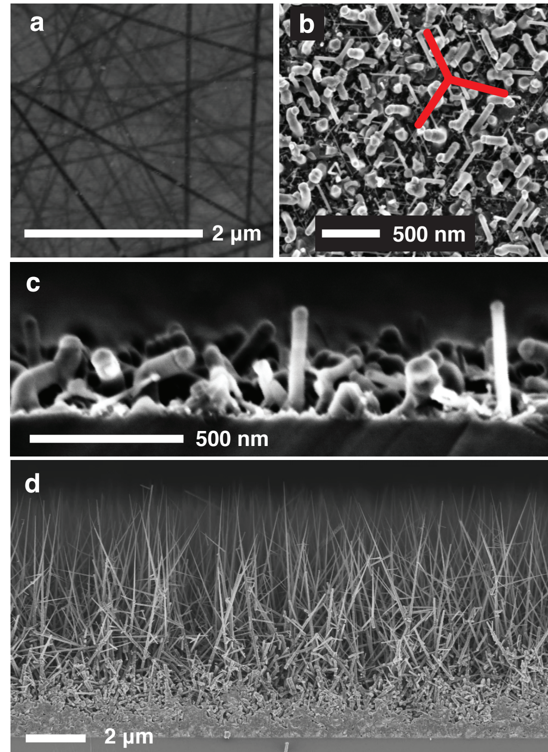

Figure 3.11. Microscopy of SiC nanowires grown on rough substrates. (a) AFM image of as-received substrate. Top-view (b) and cross-sectional SEM images (c) of nanowires grown for 2 min. (d) Cross-sectional SEM image of nanowires grown for 64 min.

As described Section 3.3.1, LOPC Raman signals were used to compare the doping concentrations of the smooth and rough 4H-SiC (0001) substrates. Following Harima et al. [80], the rough substrate is calculated to have a carrier concentration two times greater than the smooth substrate with values of 3.6×10^{18} and 1.8×10^{18} cm^{-3}, respectively (Figure 3.12a and Table 3.2). This is further confirmed with the linear empirical relationship between carrier concentration and the LOPC mode (1.25×10^{17} cm^{-3} $\times$ $\Delta\omega$), which estimates 2.9×10^{18} and 1.3×10^{18} cm^{-3} for the rough and smooth substrates, also yielding a multiplicative factor of approximately two [81]. Increased carrier concentration follows from increased nitrogen concentration in nitrogen-doped 4H-SiC crystals and contracts lattice constants in the magnitude of 10^{-5} Å [94]. Furthermore, Sasaki et al., showed the presence of lattice contraction by heavy nitrogen doping at temperatures above 800 °C and calculated the lattice mismatch between lightly-doped epitaxial layer on heavily doped 4H-SiC (0001) as 1.7×10^{-4} at 1100 °C [95,96]. Lattice mismatch between substrate and epitaxial growth of 4H-like SiC nanowires at 950 °C could explain the discrepancy between vertical and non-vertical growth seen on 4H-SiC (0001).

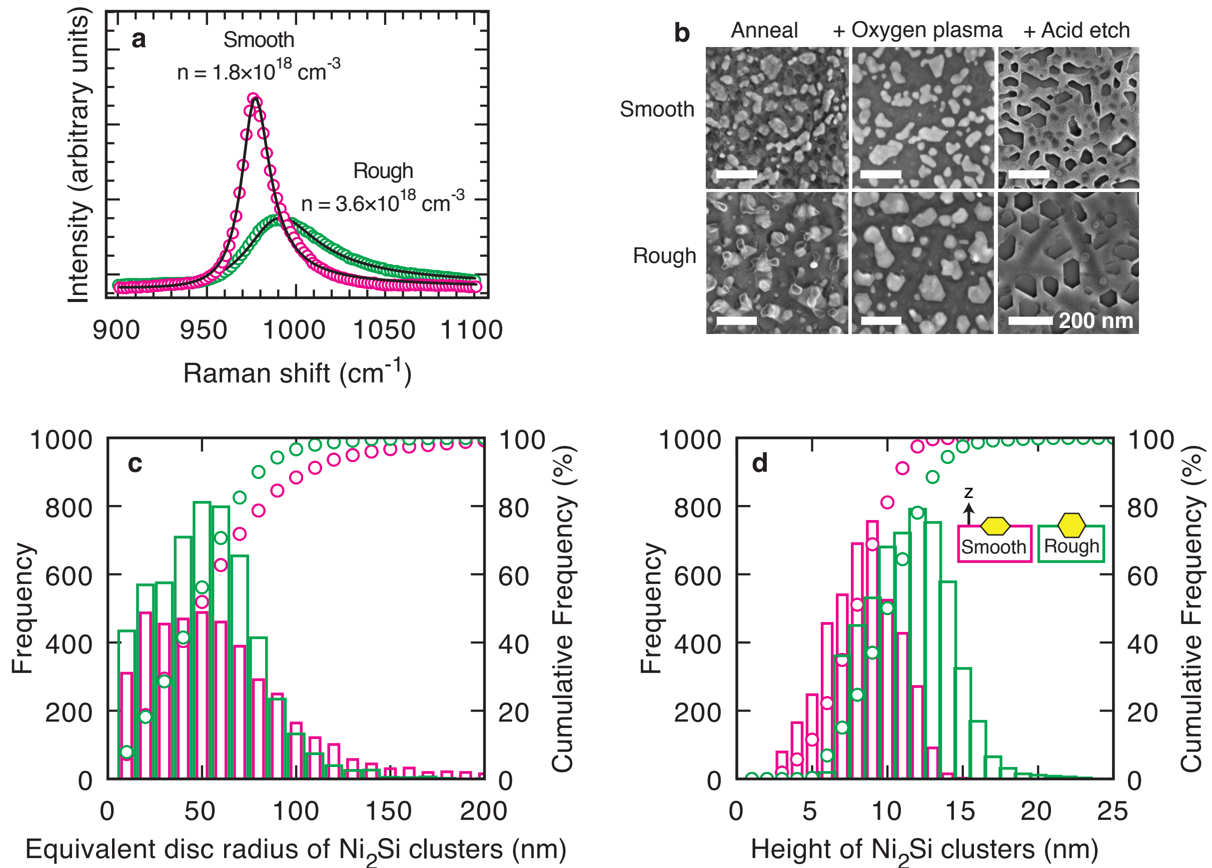

Figure 3.12. Comparison of Ni_2Si agglomeration on smooth and rough substrates. (a) Raman spectra highlighting LOPC mode and fitted to calculate substrate doping concentration (b) SEM images of 2 nm Ni/4H-SiC annealed to 950°C with 10 sccm H_2 for 10 min at 5 Torr, and after subsequent C removal and Ni_2Si removal. Ni_2Si clusters formed on smooth substrates show similar equivalent disc radii (c) with smaller heights in the z-direction (d) compared to Ni_2Si clusters formed on rough substrates. The bar graphs correspond to the frequency counts shown on left y-axis. The circles correspond to the cumulative frequency % shown on the right y-axis. Magenta = smooth substrate. Green = rough substrate.

Table 3.2. Fitted and calculated parameters from LOPC line shape shown in Figure 3.12.

		Smooth 4H-SiC substrate (Cree)	Rough 4H-SiC substrate (SiCrystalAG)
Fitted parameters	Plasmon frequency, ω_P (cm^{-1})	271	384
	Plasmon damping constant, γ (cm^{-1})	312	482
	Phonon damping constants, Γ (cm^{-1})	11.4	25.3
Calculated parameter	Doping concentration, n (cm^{-3})	1.8×10^{18}	3.6×10^{18}

Catalyst agglomeration, induced by surface roughness may also contribute to different nanowire orientations. The nickel silicide formed on both smooth and rough 4H-SiC(0001) substrates during hydrogen anneal to 950 °C (prior to precursor introduction) is crystalline Ni_2Si (Figure 3.13). Ni_2Si clusters formed on smooth substrates show a smaller equivalent disc radius (a) and a larger mean height (b) compared to Ni_2Si clusters formed on rough substrates (Figure 3.12c,d). A Ni volume analysis using the density and molecular weight of Ni, and the lattice parameters of Ni_2Si [89–91] in combination with topography information obtained with AFM were used to approximate the number of Ni atoms within the formed Ni_2Si clusters across a substrate area of 1.25×10^8 nm^2. The approximate number of Ni atoms within Ni_2Si clusters formed on smooth and rough substrates are 4.37×10^{10} and 4.58×10^{10}, respectively. This compares well to the estimated number of deposited Ni atoms (2.97×10^{10}) within 2.6 nm of evaporated Ni film across the same substrate area and suggests that all nickel is consumed during anneal to 950 °C for both substrate types.

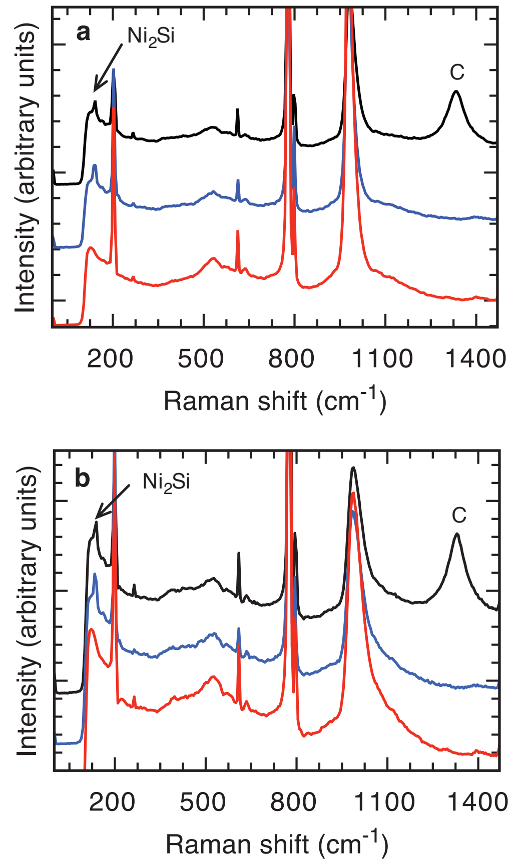

Figure 3.13. Raman spectra of thin Ni film annealed on 4H-SiC (0001) substrates (black) with subsequent oxygen plasma treatment (blue) and acid etch (red). (a) Smooth 4H-SiC (0001) substrate. (b) Rough 4H-SiC (0001) substrate.

Although the formation of Ni_2Si and C is similar on smooth and rough 4H-SiC (0001) surfaces, the same growth process yields vertical and non-vertical nanowire alignment, respectively. As received, the rough substrates lead to nanowire growth with 60° azimuthal angles. This orientation is visible with top-view SEM images of 2 min nanowires (Figure 3.14a.). The cross-sectional SEM image confirms that these nanowires do not grow vertical (Figure 3.14c). However removal of C and thus exposure of the Ni_2Si clusters before MTS introduction proved promising in achieving more vertical growth on rough substrates (Figure 3.14b,d). The C was removed by oxygen plasma as described in Section 3.3.2. During the high temperature treatment of Ni-on-SiC, C precipitates out and diffuses to the surface of the nickel silicide for Ni thickness ranging from 3 and 6 nm [97]. Cao et al. showed that if thicker Ni films are used (17 and 50 nm), the surface profile of carbon becomes more complex and may peak within the silicide in addition to its surface. In this work, approximately 2 nm of Ni is annealed on SiC. Thus it is expected that carbon is primarily located on the surface of the silicide. When carbon is removed after silicide cluster formation, but before MTS introduction, there is no longer a top layer of carbon hindering

potential nanowire growth. Another advantage of removing the carbon is that the less dense growth enables a closer examination at the nanowire base. The area of the nanowire base is smaller than the area of the original Ni_2Si cluster (Figure 3.15).

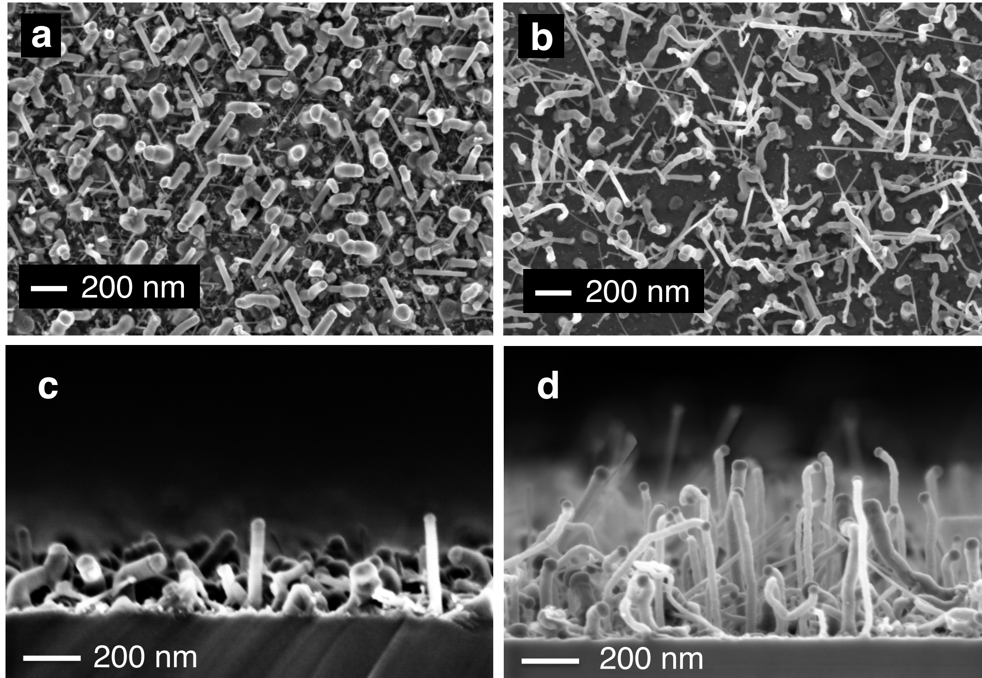

Figure 3.14. Non-vertical growth on rough 4H-SiC (0001) substrates. (a) Top-view SEM image of 2 min SiC nanowires. The nanowires show a 60° azimuthal relationship. (b) Top-view SEM image of 2 min SiC nanowires grown with Ni_2Si only. C was removed with oxygen plasma after Ni_2Si formation. (c,d) Cross-sectional SEM images corresponding to a and b, respectively.

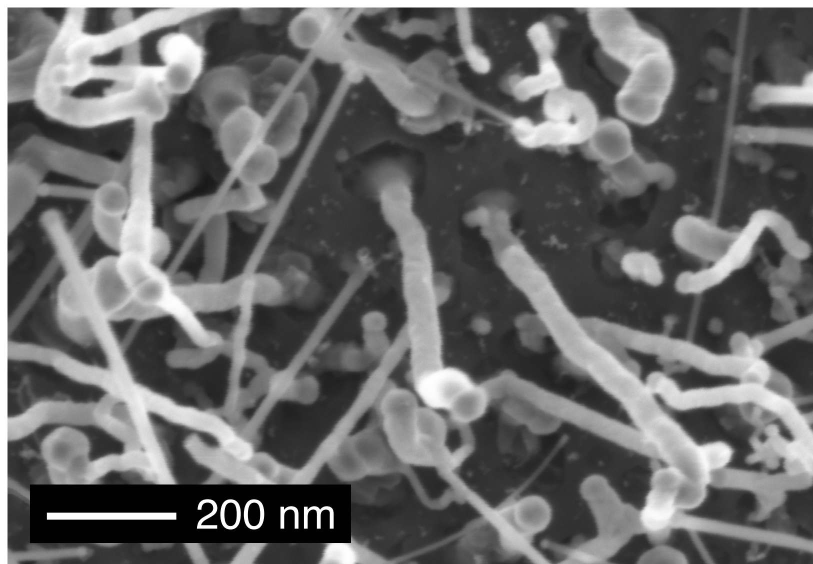

Figure 3.15. SiC growth from hexagonal pit. Zoom in of Figure 3.14b showing that the nanowire stems from a hexagonal pit formed by Ni_2Si formation on SiC.

3.9. Summary

Full understanding of a reproducible, controlled nanowire growth process can accelerate the adoption of SiC nanowires grown on SiC substrates as a robust monolithic platform and thus enable the use of SiC nanowires for biomedical, energy, nanoelectromechanical, optical, and sensor devices that can reliably operate in harsh environments. The nanowire growth process investigated here yields vertically aligned 4H-like SiC nanowires on 4H-SiC (0001). This study reveals that hexagonally shaped Ni_2Si clusters are formed on 4H-SiC (0001) at 950 °C. These clusters, formed prior to gaseous MTS precursor introduction, serve as the primary catalyst for SiC nanowire growth and play a role in the polytype of deposited SiC. The absence and presence of Ni under nanowire growth conditions lead to cubic and hexagonal phase SiC deposition, respectively. Moreover, growth temperature is identified as a facile way to target specific nanowire aspect ratios and crystallinity.

Preliminary surface studies indicate distinct differences in surface roughness and doping concentration between the 4H-SiC (0001) substrates that grow vertical SiC nanowires and those that grow non-vertical. Both of which may in turn affect catalyst agglomeration prior to nanowire growth, and thus nanowire orientation.

4. Demonstration of 4H-like SiC nanowires with vertical alignment[2]

In Chapter 3, the optimum growth temperature for Ni-assisted silicon carbide (SiC) nanowires with methyltrichlorosilane (MTS) was identified as 950 °C. At this temperature, the nanowire aspect ratio is approximately 100 and good nanowire crystallinity is observed with Raman spectroscopy. Continued efforts to push forward SiC nanowire based electronics necessitates a growth method that allows strict control of nanowire crystal structure and orientation for reliable production and performance. Towards such efforts, this chapter details the growth of hexagonal phase SiC nanowire arrays grown with vertical alignment on commercially available single crystalline SiC substrates. The nanowire hexagonality, confirmed with Raman spectroscopy and atomic resolution microscopy, displays a polytypic distribution of predominantly 2H and 4H. Employing a theoretical growth model, the polytypic distribution of hexagonal phase nanowires is accurately predicted in the regime of high supersaturation. Additionally, the reduction of disorder-induced phonon density of states is achieved while maintaining nanowire morphology through a post-growth anneal. The results of this work expand the repertoire of SiC nanowires by implementing a low-temperature method that promotes polytypes outside the well-studied cubic phase and introduces uniform, vertical alignment on device-ready SiC substrates.

4.1. SiC nanowire orientation on SiC substrates

SiC nanostructures provide the resiliency for pushing past the limits of current technology to achieve small, durable, efficient devices that can function in high temperature, high power, reactive, or biological environments [17,98]. In particular, SiC nanowires attract interest as

---

[2] A modified version of this work was published in L.E. Luna, C. Ophus, J. Johansson, R. Maboudian, C. Carraro. "Demonstration of hexagonal phase silicon carbide nanowire arrays with vertical alignment." *Cryst. Growth Des.* 16 (2016) 2887-2892. DOI: 10.1021/acs.cgd.6b00203.

biological sensors [18], field emission cathodes [99,100], nanoelectromechanical switches [101], optical circuits [102], and energy storage devices [23,67,103]. Further advancement of SiC-based nanotechnology requires growth on industry standard 4H-SiC (0001) substrates and manipulation of electrical and optical properties through polytype control. Yet non-vertical, non-aligned, cubic 3C-SiC nanowires constitute the only report of uniform growth of a single-polytype nanowire array, wherein all nanowires display similar polytype across the surface of this substrate [8,104]. In addition to polytype control, the robust nature of SiC presents difficulties for SiC nanofabrication and it highlights the important issue of developing feasible, large-scale nanofabrication of SiC materials for next generation nanodevices. This work addresses both of these issues through demonstration of vertically aligned arrays of hexagonal phase silicon carbide nanowires, grown uniformly across the industry standard 4H-SiC (0001) surface. The isolation of hexagonal phase SiC nanowire growth on 4H-SiC (0001) taps into the polytypic nature of SiC to present a facile fabrication method for hexagonal, vertically aligned SiC nanowire arrays, assembled as a monolithic structure for robust nanoelectronics.

SiC is characterized by extreme polytypism, consisting of over two hundred different polytypes that differ only in the atomic stacking of Si-C bilayers [105]. These SiC polytypes have different electronic properties (such as band gap and mobility), which if controlled, would facilitate heteropolytype [106] and superlattice quantum structures [107] capable of operating in harsh environments. To understand SiC polytypism, Cheng et al. applied the axial next nearest neighbor Ising (ANNNI) model to describe the interlayer interactions and constructed phase diagrams detailing the lowest energy structures based on interaction parameter J_i [108]. Building on this earlier work, polytypism in a different system, namely III-V nanowires [109], was modeled with ANNNI and nucleation theory to identify key growth parameters (such as supersaturation and impurities) that affect wurtzite (hexagonal) or zinc-blende (cubic) nucleation [110,111].

In the case of SiC nanowires, choice of substrate and growth method hold promise for controlling SiC nanowire polytypism. The use of single-crystalline SiC substrates can affect nanowire polytype and growth orientation through epitaxial lattice matching (Figure 4.1). Krishnan et al. showed that SiC nanowires could be grown with well-defined epitaxial relation on the 4H-SiC (0001) surface [104] but the nanowires were predominately cubic 3C-SiC, with their axes inclined at 70° with respect to the [0001] direction perpendicular to the surface and oriented azimuthally along six directions at 60° with respect to each other, while very few nanowires grew vertically with axes parallel to the [0001] direction (Figure 4.1b). The authors proposed that the few vertically aligned nanowires were 4H-SiC. A later study achieved vapor-liquid-solid growth of aligned, but non-vertical cubic 3C-SiC nanowires grown on 4H-SiC faces that were exposed by reactive ion etching of 4H-SiC (0001) substrates to form mesas [8].

In this chapter, vertically aligned arrays of hexagonal phase SiC nanowires are grown directly on the device-ready 4H-SiC (0001) substrate and an ANNNI/nucleation theory model is employed to predict SiC polytypism. The growth procedure utilizes Ni thin films as the catalyst, MTS as the single precursor, and a growth temperature of 950 °C. Experimental evidence presented in this dissertation suggests that nickel silicide clusters catalyze growth. Due to low solubility and low diffusion coefficient of carbon in nickel silicide [112], a low growth rate and a high

supersaturation are expected to promote the formation of hexagonal polytypes. The observation of the hexagonal phase with Raman spectroscopy and high-resolution scanning transmission electron microscopy (STEM) is in agreement with the predictions of a growth model based on the ANNNI model and classical nucleation theory, developed originally to explain polytypism in III-V nanowires [113] and adapted here to describe SiC nanowire growth.

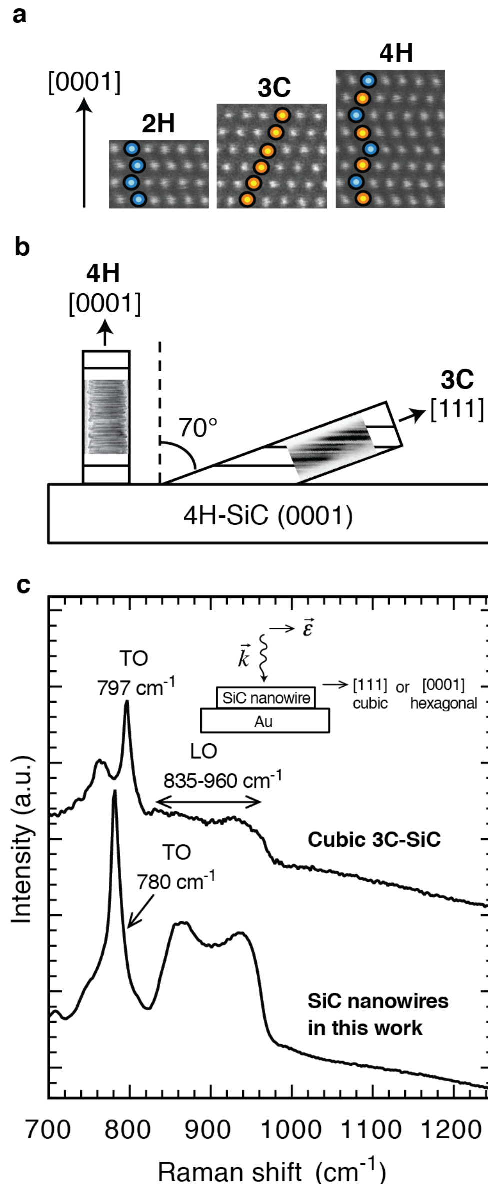

Figure 4.1. Characteristic differences between common SiC polytypes. (a) STEM micrographs of selected regions of SiC nanowires with local 2H (100% hexagonality, h=1), 3C (0% hexagonality, h=0, 100% cubic), and 4H (50% hexagonality, h=0.5) crystal structures. Local cubic sites consist of a translation of subsequent layer, whereas local hexagonal sites consist of

both a translation and rotation of subsequent layer. Local cubic and hexagonal Si-C units are indicated in orange and blue, respectively. (b) 4H-SiC and 3C-SiC nanowire alignment on 4H-SiC (0001). TEM insets show that the stacking faults are parallel to the [0001] substrate direction for 3C- and 4H-SiC nanowires. (c) Raman spectrum of cubic 3C-SiC nanowire (top, Fréchette et al. [114]) and hexagonal SiC nanowire (bottom). Inset shows the Raman scattering geometry where $\vec{k}$ is the momentum and $\vec{\varepsilon}$ is the polarization of the light.

4.2. Experimental Section

SiC nanowires were grown on research-grade n-type 4H-SiC (0001) substrates with 4° off-axis cut towards <1120>, low micropipe density (≤ 15 micropipes/cm^2), and 0.015-0.028 Ω-cm resistivity range (Cree Research). Prior to use, substrates were sonicated for 5 minutes in separate baths of acetone and isopropanol, and cleaned for 5 minutes in an ultra-violet ozone cleaner, followed by 10 s rinses in hydrofluoric acid (HF) and distilled water, and dried with N_2 gas.

Thin nickel films (~2.6 nm) were deposited onto SiC substrates via electron beam evaporation (Thermionics VE-700 Vacuum Evaporator) of a nickel source (Alfa Aesar, 99.995%). Substrates were then transported to and sealed in a hot-wall chemical vapor deposition (CVD) tube furnace (Thermo Scientific Lindberg Blue M) to a base pressure of 20×10^{-3} Torr, wherein they were heated to 950°C at a rate of 44°C/min at 5 Torr under 10 sccm flow of H_2 (Praxair, 99.99%). For SiC nanowire growth, once the furnace reached 950°C, MTS (Sigma-Aldrich, 99%) at a flow rate of 0.5 sccm was introduced for a specific length of time, ranging between 2 and 64 min, after which the MTS was turned off and samples were cooled to room temperature at a rate of ~22°C/min under 10 sccm H_2.

Samples were characterized by scanning electron microscopy (SEM, Zeiss Gemini Ultra-55, accelerating voltage set to 2 kV), scanning transmission electron microscopy (STEM with high-angle annular dark field detector, FEI/Titan transmission electron aberration-corrected microscope, at 300 kV), and Raman spectroscopy (Horiba Jobin Yvon LabRam, excitation line provided by a HeNe laser at 632.8 nm, through a 100X objective with 0.8 numerical aperture). For single nanowire Raman spectroscopy, substrates with nanowires were sonicated in 3 mL ethanol for 10 s and 3-5 µL of sonicated solution was pipetted onto a Au substrate.

For STEM analysis, nanowires were sonicated in 250 µL of ethanol for 1-3 minutes. A low volume of ethanol is used to deposit a large enough concentration of nanowires for easier viewing in the microscope. Below are three possible ways to place nanowires on TEM grid (ultra-thin carbon film on holey support) with little to no carbon contamination. All approaches require pre-heating a hotplate to 100 °C and cleaning a glass slide (for example, using a UVO cleaner for 3 min).

First, the nanowires can be drop casted (3-5 μL) from the sonicated solution onto a suspended TEM grid gripped by self-closing TEM tweezers. Placing the TEM grid, while gripped by self-closing tweezers, above the pre-heated hot plate will ensure that residual ethanol quickly evaporates and thus reduce the amount of carbon contamination during imaging. If the nanowires are on the order of several microns long, then the optical microscope can be used to verify that nanowires are secured on the grid. It might be necessary to continue drop casting (1-3 more times) until a sufficient number of nanowires have been drop casted. Increasing the number of drops increases the likelihood of carbon contamination within the microscope.

Second, the nanowires can be scooped onto a TEM from the sonicated solution. With this approach, the TEM grid is dipped into the sonicated solution with self-closing tweezers. Still gripped by self-closing tweezers, the TEM grid is placed on the pre-heated hotplate for at least 10 min.

The first and second approaches involve ethanol, which makes the TEM grid prone to carbon contamination. After drying grid on the pre-heated hotplate, placing the grid on a cleaned glass slide within a UVO chamber and cleaning for 2 min gets rid of residual carbon.

The third approach does not involve ethanol. It involves taking a TEM grid and dragging it across the sample/nanowire surface. If the TEM grid has a film on one side, then its preferable to drag the grid on the non-film side as the dragging motion will rip the film.

4.3. Raman spectroscopy characterization

Figure 4.1c shows the Raman spectrum of a single SiC nanowire grown in this work, with the scattering geometry indicated in the inset. Although the longitudinal optical (LO) mode is forbidden in backscattering configuration at 90° from the c-axis, disorder-induced LO density of states is usually visible [82]. The transverse optical (TO) mode of A_1 symmetry is the most prominent in the spectrum. For comparison, the spectrum of a cubic 3C-SiC nanowire is also shown [114]. The most striking difference between the two spectra is the shift in the TO phonon peak position form 797 cm^{-1} for the 3C wires to 780 cm^{-1} with a standard deviation of ± 2 cm^{-1} for the wires grown in this work. This shift arises due to local bonding environment of Si and C atoms, which is different in a cubic site versus a hexagonal site and is apparent in Raman scattering. Specifically, hexagonal symmetry lifts the degeneracy between the planar and axial optical phonons, so that in hexagonal polytypes, the frequency of TO phonons with A_1 symmetry, $\omega(A_{1t})$, is redshifted with respect to the frequency of the E symmetry phonons, $\omega(E_t)$, by an amount proportional to the fraction of hexagonal sites, h. By comparing the spectra of numerous SiC polytypes, Nakashima and coworkers [115] derived the following empirical relation for h:

$$\omega(E_t) - \omega(A_{1t}) = 29.4h \,, \qquad \text{(eq. 4.1)}$$

with frequencies given in cm^{-1}. Here, $\omega(E_t) \approx 797$ cm^{-1} is constant, regardless of polytype. From equation 4.1, the fraction of hexagonal sites for nanowires presented here is 58%; this is slightly larger than expected for the 4H polytype (50%), but less than expected for the 2H polytype (100%).

4.4. Atomic resolution transmission electron microscopy (TEM) characterization

The high hexagonality content of these wires is further confirmed with atomically resolved transmission electron microscopy. The low resolution STEM (Figure 4.2a) reveals the high density of stacking faults that are perpendicular to the nanowire growth axis. This finding agrees with the stacking fault orientation observed previously in 4H-SiC nanowires [104]. Figure 4.2b shows a high-resolution STEM image of a typical nanowire from which further analysis was done to investigate its polytypic nature. Classification of the stacking sequence as either hexagonal or cubic (as explained in Figure 4.1) revealed that 61% of 645 Si-C units reside in hexagonal sites (Figure 4.2c). More specifically, polytype color maps show that Si-C units form instances of isolated and sometimes overlapping stacking patterns corresponding to the 3C, 2H, and 4H polytypes (Figure 4.2d-f).

The identification of 3C, 2H and 4H polytypes within single SiC nanowires was done by Dr. Colin Ophus using a custom MATLAB processing routine. In this routine, a mean unit cell along the wire growth direction was calculated using lattice fitting (averaged perpendicular to the growth direction) from the scanning electron micrographs of SiC nanowires shown in Figure 4.3. Each plane was identified as A, B or C based on an in-plane offset of 0, 1/3 or 2/3 respectively, and was assigned either a hexagonal or cubic identity based on its neighboring plane. The entire set of planes was compared to all permutations of ABC (3C), AB (2H), and ABCB (4H) stacking. Each cluster of planes of length 4 or greater were assigned the appropriate polytype, after removing the 2 terminating planes, to prevent ambiguities such as hexagonal terminating planes on the 3C polytype. In other words, polytype differentiation was obtained from electron micrograph analysis, with the minimum length of a polytype as four Si-C bilayers. Note that a small number of stacking clusters could be classified into these three categories, and that some configurations allow neighboring polytypes to share a single plane. The tabulated results of polytype classification are reported in Table 4.1.

Although a polytypic mixture is expected due to the high stacking fault density, combined statistics over 645 Si-C layers identify the 2H and 4H polytypes as most prevalent with an overall distribution of 47% as 2H, 39% as 4H, and 16% as 3C. Since the hexagonality values obtained both by equation 4.1 and Figure 4.2 are closest to the 4H polytype (50%), these nanowires are referred to as 4H-like.

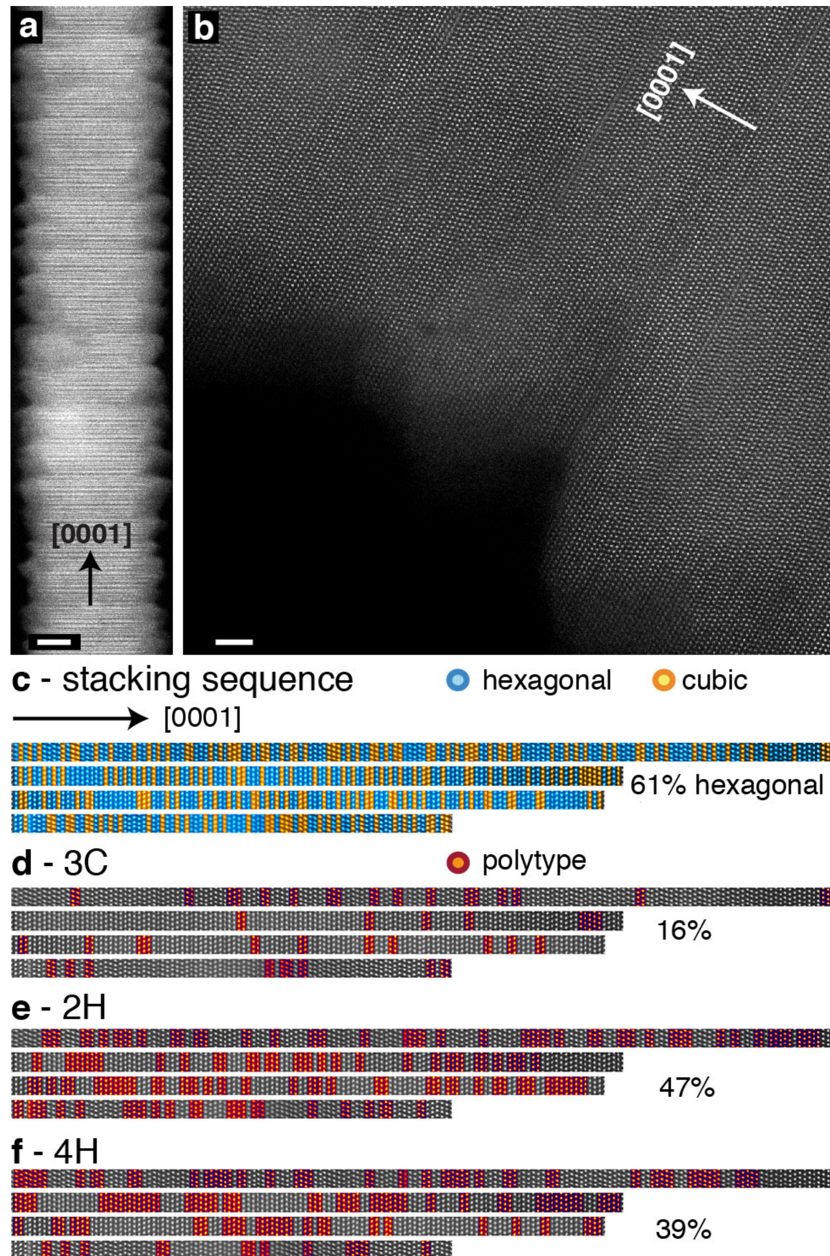

Figure 4.2. Existence of polytypic mixture within nanowire confirmed by high resolution STEM. (a) Low resolution STEM micrograph shows stacking faults are perpendicular to nanowire axis, indicated by the black arrow. Scale bar is 20 nm. (b) High resolution STEM micrograph shows good atomic resolution for stacking fault analysis. Scale bar is 2 nm. (c) Hexagonality maps of 4 different nanowire segments highlighting local cubic (orange) and hexagonal (blue) Si-C units along the nanowire axis. (d-f) Polytype maps of nanowire segments shown in (c), highlighting instances of 3C, 2H, and 4H, respectively (red) along nanowire axis. The percentages listed to the right of c-f are combined statistics across 645 Si-C units. The sum of percent polytype appearance is slightly larger than 100% due to overlapping or shared layers.

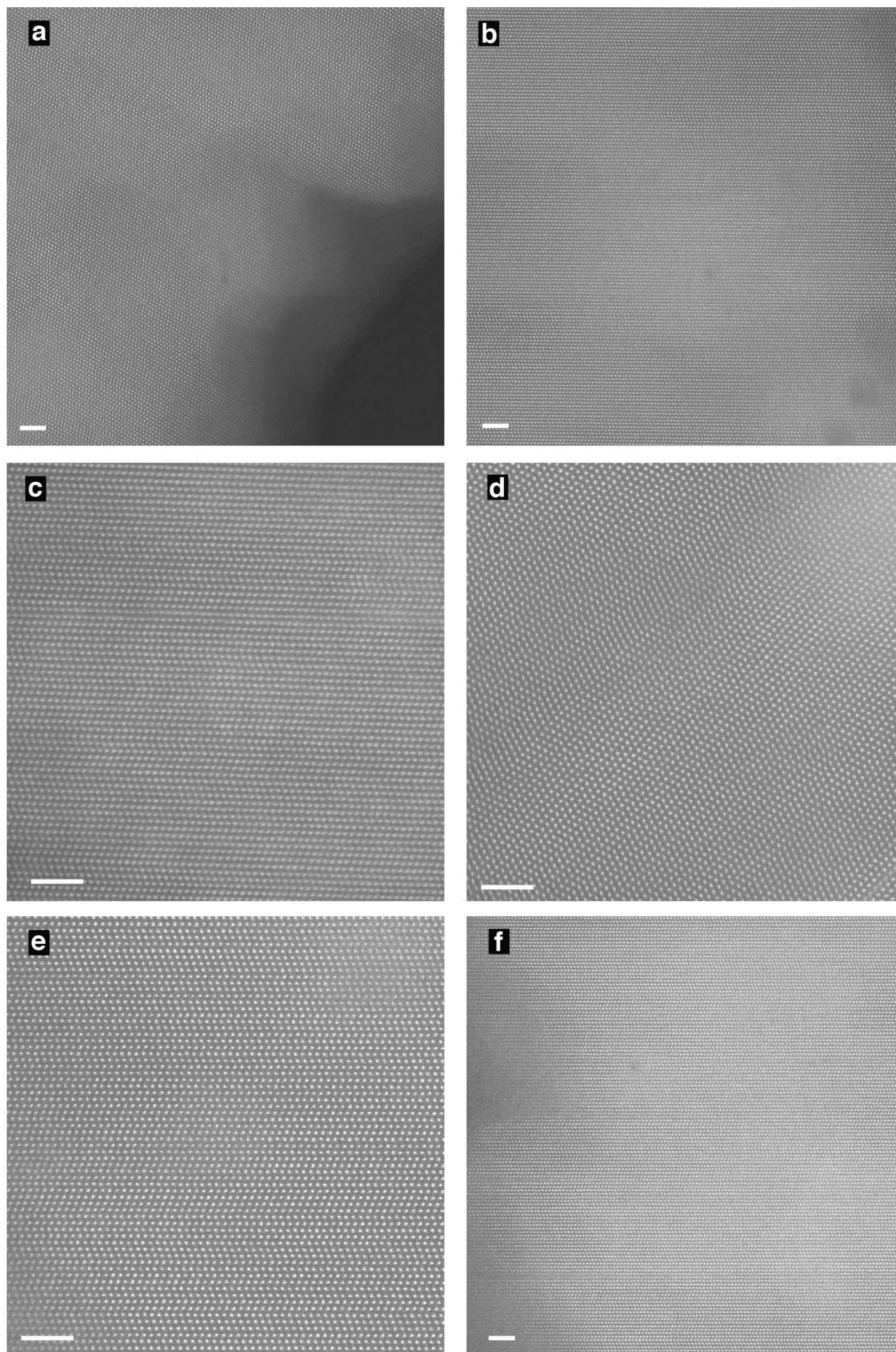

Figure 4.3. Unaltered atomic resolution by high-resolution STEM micrographs used to characterize polytype mixture of different nanowire regions. Different magnifications are used,

but all result in atomic resolution of the SiC nanowire. All images were taken close to nanowire edge, as the nanowire edge tends to be thinner, thus better for atomic resolution (a-f). The combined statistics over 645 Si-C units in Figure 4.2 were obtained from these micrographs. All scale bars are 2 nm.

Table 4.1. Identification of polytypes and local hexagonal planes.

Panel in Figure 4.3	Total No. of planes	No. of 3C planes	No. of 2H planes	No. of 4H planes	No. of locally hexagonal planes
a	172	31	78	70	104
b	128	13	52	67	77
c	64	13	21	29	35
d	92	17	40	23	54
e	65	10	49	19	43
f	124	21	64	44	79
Combined statistic (sum)	645	105	304	252	392
Combined statistic	-	16.3 %	47.1 %	39.1 %	60.8 %

4.5. Structure modeled by axial next nearest neighbor Ising and nucleation models

To understand polytypism in nanowires, Johansson et al. developed a theoretical model based on the axial next nearest neighbor Ising model and classical nucleation theory [113]. The model defines a sequence of four stacked bilayers as 2H, 4H, or 3C and accurately predicts polytypes seen in GaAs and Sb-containing III-V nanowires as a function of supersaturation. The following SiC parameters were used to adapt the model to SiC nanowire growth: nanowire growth temperature, twin plane energy σ_t, cubic 3C step energy γ_{3C}, and interaction range parameter η. The SiC twin plane energy is approximated as half the stacking fault energy [116,117], yielding σ_t = 17.5 mJ/m^2. Due to a lack of step energy data for SiC, the step energy for 3C-SiC is approximated as 245 mJ/cm^2, the average step energy between silicon [116] and diamond (Table 4.2). The step energies of hexagonal polytypes are approximated as $\gamma_{2H} = 0.3\gamma_{3C}$, $\gamma_{4H'} = 0.6\gamma_{3C}$, $\gamma_{4H''} = \gamma_{3C}$, adapted from Johansson et al. [113]. The two values for the 4H polytype arise because in 4H, every other layer is hexagonally stacked (4H') and every other layer is cubically stacked (4H''). The interaction range parameter η equals $-J_1/J_2$ where J_i is the interaction energy between

the ith neighboring layers, with $J_1 > 0$ and $J_2 < 0$. A value of $\eta = 2.8$ represents our experimental data well and agrees with a previous study that reports SiC is characterized by $J_1 \approx -2J_2$ [108].

The adapted model predicts SiC polytype formation probability as a function of the supersaturation, measured as the ratio of chemical potential difference ($\Delta\mu$) and atomic site area (s) (Figure 4.4a). Similar to III-V nanowires, SiC polytype formation probability shows that the 3C, 4H, and 2H polytype dominate at relatively low supersaturation, intermediate supersaturation, and high supersaturation, respectively. For comparison, the combined statistics of polytype assignments from analyzed STEM images are shown in dashed lines in Figure 4.4a. The model and experimental data begin to converge in the regime of high supersaturation for all displayed polytypes.

Table 4.2. Estimated step energy for SiC.

	Equation	**Diamond**	**Si***	**SiC**
Lattice constant, *a*	-	3.57×10^{-8} cm	-	-
Density, ρ	-	3.515 g/cm^3	-	-
Molecular weight, *MW*	-	12.01 g/mol	-	-
Atomic density, *q*	$\rho \times N_A / MW$	1.76×10^{23} cm^{-3}	-	-
Heat of fusion, ΔH †	-	120 kJ/mol	-	-
		1.99×10^{-12} erg/atom	-	-
Melting temperature, T_m ††	-	4100 K	-	-
Excess energy of interfacial bond, *W*	$0.45 \times \Delta H$	8.96×10^{-13} erg/atom	-	-
Step energy**, γ_{3C}	$1.5^{1/2} q^{2/3} \left\{ \frac{W}{3} - k_B T_m \ln\left[1 + 2\exp\left(\frac{-W}{k_B T_m}\right)\right]\right\}$	402.6 erg/cm^2	87.6 erg/cm^2	245*** erg/cm^2

* See Hurle et al. [116].
** The step energy for diamond was calculated using equation given in Hurle et al. [116], adapted from Voronkov et al. [118].
*** Taken as the average value of diamond and Si.
† Heat of fusion of diamond is estimated as graphite's heat of fusion, measured by Heremans et al. [119].
†† Melting temperature of diamond is estimated as the diamond/graphite/liquid triple point at 125 kbar, given in Bundy et al. [120,121].

The appearance of the 2H polytype induced by high supersaturation in III-V nanowire systems has been reported previously [93]. In these systems, the change from high to low supersaturation may be controlled by the presence of impurities that either decrease or increase the equilibrium concentration of the group III species within the catalytic cluster of III-V nanowires [93,122]. For the 4H-like IV-IV SiC nanowires produced in this work, we believe instead that high supersaturation is enabled by the low solubility of carbon within the nickel silicide catalytic cluster. Ex-situ room temperature Raman measurements suggest that nickel-rich silicide, Ni_2Si, is present upon annealing to 950 °C and after short nanowire growth times (Fig. 4.4b). The presence of Ni_2Si before and after MTS precursor introduction strongly suggests that Ni_2Si is the catalyst during nanowire growth.

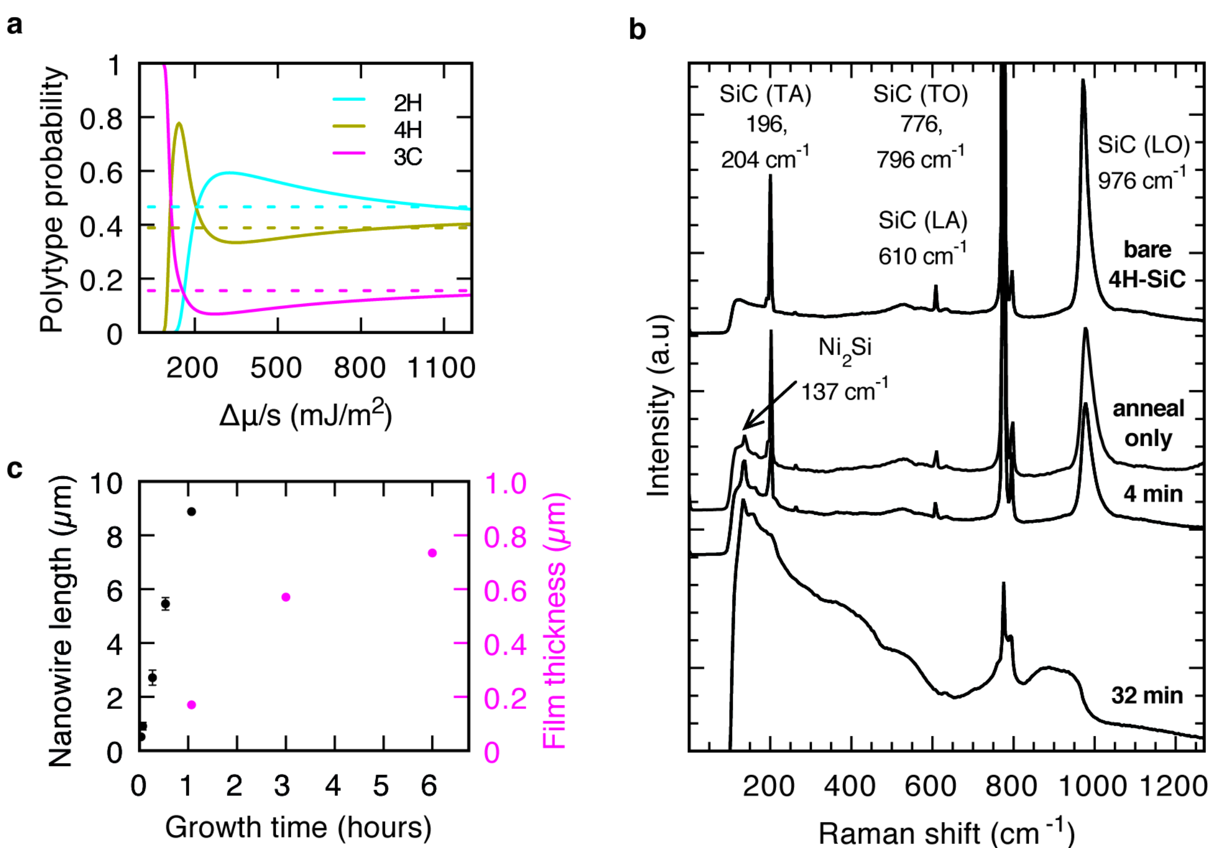

Figure 4.4. Hexagonal SiC nanowire growth is explained by high supersaturation within the catalytic cluster during growth. (a) Polytype formation probability as a function of supersaturation. Above 600 mJ/m^2, a polytypic mixture ranging from 71% to 66% is predicted. (b) Raman reveals Ni_2Si as catalyst. As the Raman laser has a penetration depth of ~1 μm, for short growth times (4 min), the 4H-SiC substrate signal is strong, but weakens with longer growth times (32 min) while the Raman scattering of the SiC nanowires is strengthened. The evolution of a TO phonon shoulder and broad peaks between 835-960 cm^{-1} is also apparent and likely due to nanowire disorder. (c) Nanowire length (filled black circles) and uncatalyzed film

thickness (filled magenta circles) as a function of growth time at 950 °C. For each growth time, wire length is obtained from an average of 30 nanowires. Error bars show one standard deviation.

4.6. Substrate induced vertical growth

The growth rate of the 4H-like SiC nanowires is approximately 8.6 µm/h (Figure 4.4c). This is much slower than the nanowire growth rate of 40 µm/h or greater reported elsewhere for vapor-liquid-solid growth process [104]. However, our measured growth rate is comparable to the vapor-solid growth rate of 5-6 µm/h for low-temperature SiC epitaxial layers [123], perhaps not surprisingly, given the low carbon solubility and diffusion in nickel and nickel silicide [112]. Nevertheless, in this system, the vapor-solid or uncatalyzed film growth at 950 °C results in even slower growth rate (Figure 4.4c). It is proposed that the low carbon solubility and diffusion through the catalytic Ni_2Si clusters affords the large degree of supersaturation necessary for the growth of hexagonal polytype. In our high-supersaturated system, the low growth rates likely arise from the lower growth temperature (compared to 1100 °C and higher [73,104] combined with low precursor diffusion rate within the nickel silicide catalyst.

Given the 4H-like structure of the nanowire, vertical alignment is expected on 4H-SiC substrates for epitaxial growth (Figure 4.1b). This expectation is borne out in our SEM analysis, demonstrating vertical SiC nanowire growth (Figure 4.5a,b). Vertical SiC nanowire growth on the 4H-SiC (0001) face, enabled by the high supersaturation growth regime as demonstrated here, opens a new avenue for efficient fabrication and processing of SiC nanostructures that takes advantage of a monolithic structure with low lattice mismatch. Moreover, residual crystal defects can be reduced by post-growth annealing without affecting nanowire alignment (Figure 4.5c). The results of a 3-minute anneal at 1700 °C under inert gas include a dramatic decrease in the disorder-induced LO phonon density of states, evidenced by the significantly reduced signal within 835-960 cm^{-1} (Figure 4.5d). The post-growth anneal also transforms the broad TO signal (780 cm^{-1}) into a triplet with peaks at 764 cm^{-1}, 780 cm^{-1}, 797 cm^{-1}, indicative of 2H-, 4H-like, and 3C-SiC regions, respectively. However, the 780 cm^{-1} 4H-like signal still dominates as in before heat treatment. The ability to improve SiC hexagonality through minimization of 3C layers is still underway.

Although nanowire alignment is maintained after the 1700 °C post-anneal, it is evident the physical appearance of the nanowires is altered (Figure 4.5c,d). The nanowires transform from the originally densely packed tapered nanowires with sharp tips to bulkier nanowires with blunt tips. This transformation is likely due to sintering of nanowires during the 3 min anneal at 1700 °C, as well as during the 1 hour ramp time to 1700 °C, as reported under similar conditions [124]. A closer look at the treated nanowires reveals junctions formed at nanowire tips (Figure 4.6). The Si-C units formed at the junction maintain high hexagonality of 63%, similar to original 4H-like nanowires grown at 950 °C. Thus, the nanowires maintain alignment and hexagonality, while reducing disorder when exposed to 1700 °C for 3 min.

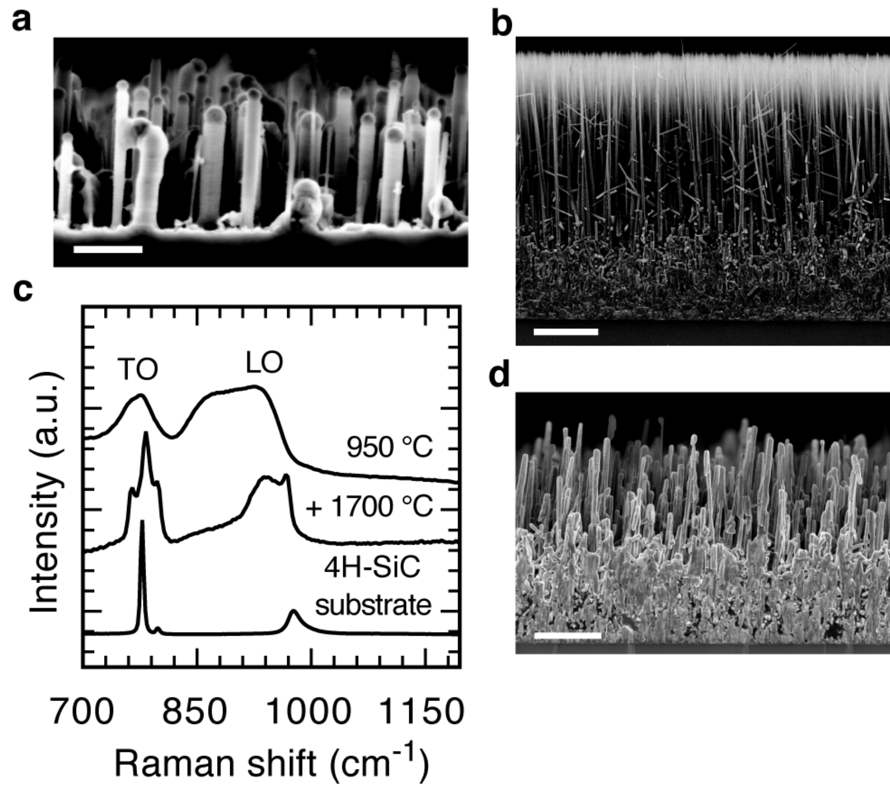

Figure 4.5. Orientation and crystalline integrity of SiC nanowire array grown on high-quality 4H-SiC (0001). (a) Cross-sectional SEM micrograph of nanowires grown for 2 min. Scale bar is 200 nm. (b) Cross-sectional SEM micrograph of nanowires grown for 64 min. Scale bar is 2 µm. (c) Raman spectra highlighting crystalline repair of SiC nanowires with 3-minute post-growth anneal at 1700 °C under inert Argon gas. Single crystalline 4H-SiC (0001) is shown for reference. Raman scattering was collected from nanowire array with incident light parallel to nanowire axis. (d) Cross-sectional SEM image of SiC nanowires heat-treated to 1700 °C retain vertical alignment and nanowire morphology. Scale bar is 2 µm.

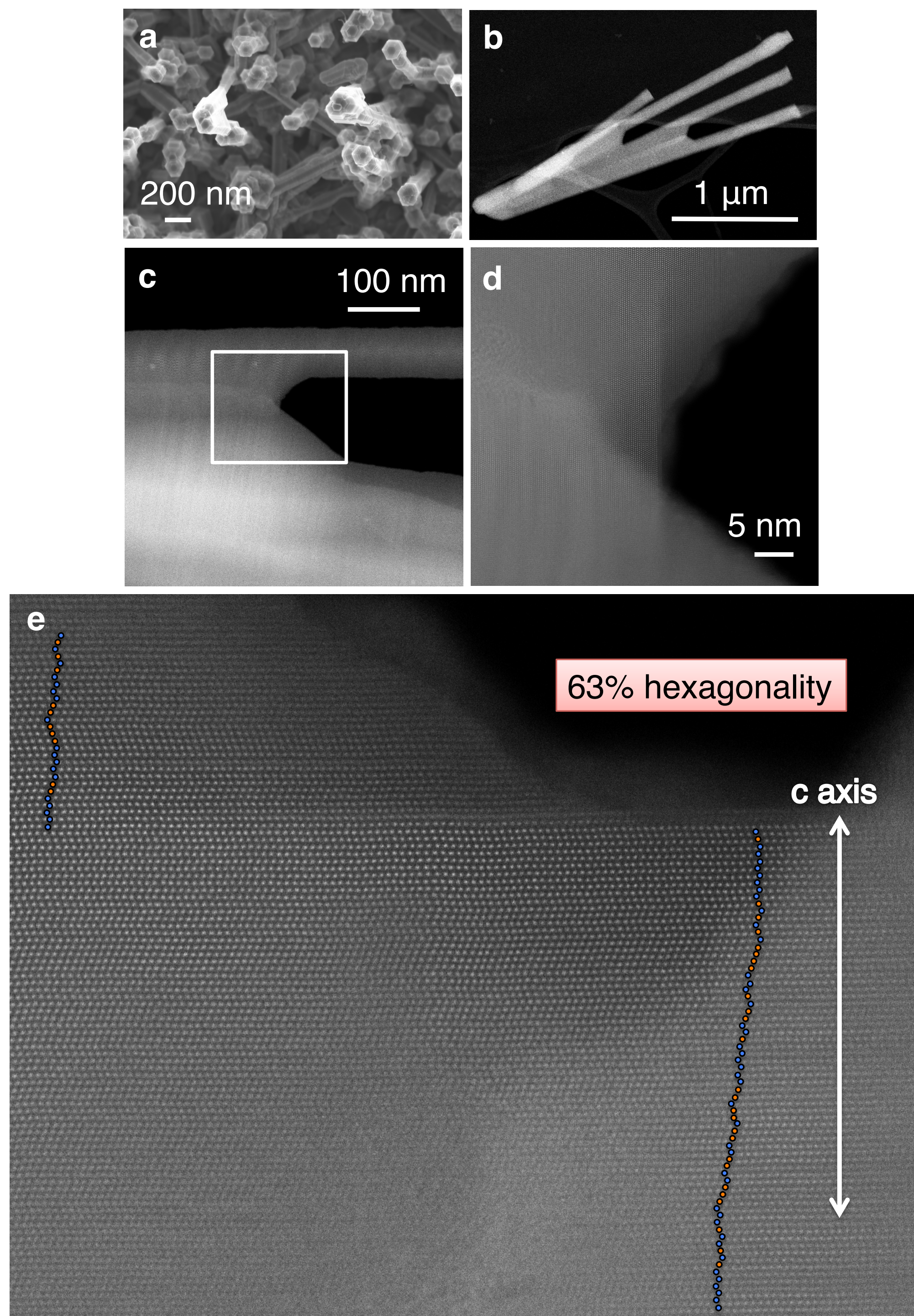

Figure 4.6. Microscopy of nanowires heat-treated to 1700 °C. (a) Top-view SEM shows nanowire tips bundle together. (b) STEM image showing bundled nanowires. (c,d) Junction of bundled nanowires. (e) Identification of locally hexagonal (blue) and cubic (orange) Si-C units after 1700 °C treatment. Panel e is a magnified version of d, rotated 90° counterclockwise.

4.7. Nanowire morphology

Low resolution scanning transmission microscopy micrographs reveals nanowire tapering and that stacking faults are perpendicular to nanowire axis (Figure 4.7) [9,104]. The stacking faults are more clearly visible in Figure 4.7b obtained with high resolution TEM.

SiC generates a rich Raman spectrum of induced phonon modes (atomic lattice vibrations) when subjected to incident visible light. The most dominant phonon modes are out-of-phase or optical lattice vibrations described as the transverse (TO) and longitudinal optical (LO) modes. The TO mode in particular is commonly used to identify the polytypes of SiC. For 3C-SiC, the TO and LO peak positions are centered at 796 and 964 cm^{-1}. On the other hand for 4H-SiC, the primary TO and LO peak positions are centered at 776 and 972 cm^{-1}. The 4H-like SiC nanowires display a TO peak positioned at 780 cm^{-1} and a broad LO signal ranging from (Figure 4.8a). Comparing TO peak position, hexagonality can be estimated [115]. The 780 cm^{-1} is 4 cm^{-1} away from 4H and 16 cm^{-1} away from 3C and thus is expected to be more 4H-like than 3C-like. The appearance of second-order SiC signals at approximately 1510 cm^{-1} and 1710 cm^{-1} indicate good crystallinity.

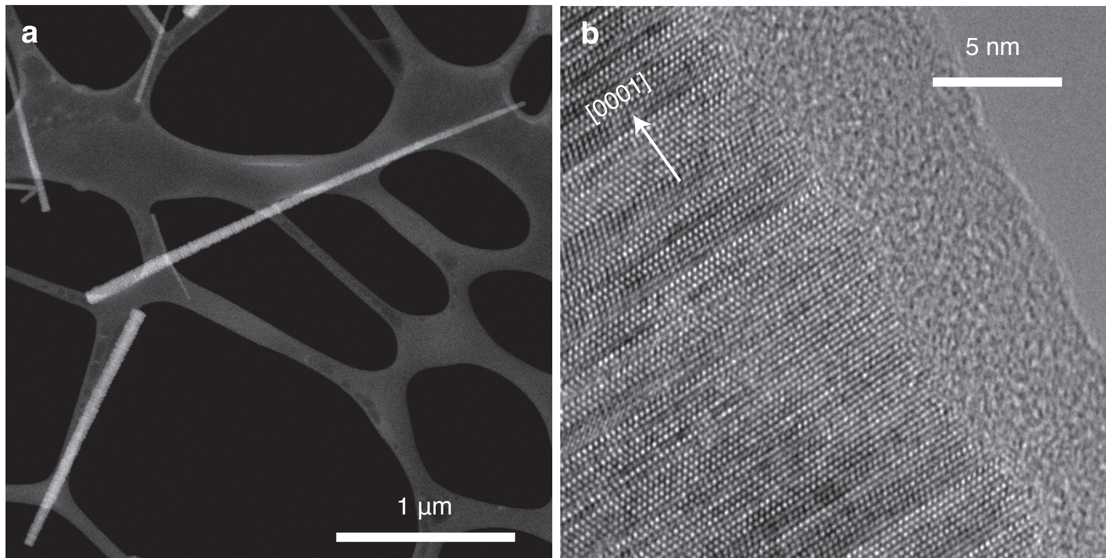

Figure 4.7. Morphology and atomic stacking of SiC nanowires. (a) Low resolution STEM image of SiC nanowires on TEM grid. (b) High resolution TEM image of SiC nanowire lattice planes.

4.8. Electronic characterization

Structural characterization via Raman spectroscopy and atomic resolution microscopy identify that the hexagonal phase SiC nanowires grown on 4H-SiC resemble that of the 4H polytype, hence the name 4H-like (Sections 4.1-4.6). For nanowire-based devices that rely on optical and

electronic performance, structural characterization is only part of the picture. The full picture needs to include electronic characterization. As the energy band gap is an important electronic characteristic, the following sections report band gap measurements on the 4H-like SiC nanowires via electron energy loss spectroscopy. In this section, it is shown that although the 4H-like nanowires include cubic 3C-SiC stacking faults, the band gap across a nanowire is effectively that of hexagonal phase SiC, as opposed to cubic.

4.8.1. Sample preparation for electron energy loss spectroscopy (EELS)

Nanowires characterized in this work are grown on 4H-SiC (0001) substrates (Cree Research). Substrates are cleaned with acetone, isopropanol, hydrofluoric acid (HF), distilled water, finally and dried with nitrogen gas. Electron beam evaporation (Thermionics VE-700 Vacuum Evaporator) is used to deposit 2 nm of nickel source (Alfa Aesar, 99.995%) onto clean substrates. The Ni-on-SiC sample is heated to 950 °C under 10 sccm hydrogen gas (Praxair, 99.99%) in a hot-wall chemical vapor deposition (CVD) quartz tube furnace (Thermo Scientific Lindberg Blue M). Once at 950 °C, 0.5 sccm of methyltrichlorosilane (MTS, Sigma-Aldrich, 99%), single-source precursor, is introduced to begin nanowire growth. After 64 min of nanowire growth, MTS is turned off and tube furnace cooled to room temperature at ~22 °C/min.

4.8.2. Nanowire EELS analysis

TEAM 0.5 at the National Center for Electron Microscopy (NCEM) was used to obtain EEL spectrum of single SiC nanowires. EEL spectra were obtained by Dr. Velimir Radmilović. The measurement involves exposing the sample to an electron beam with a narrow energy range. The electrons can scatter elastically or inelastically. The zero-loss (ZL) peak is a result of elastic scattering and the energy loss spectra is a result of inelastic scattering. For SiC band gap determination, the low energy loss spectra (<5 eV) is important, thus the ZL peak which occurs at 0 eV is removed from raw EEL spectrum by the subtraction or deconvolution method. The deconvolution is done using Thermo GRAMS Electronic Structure Tools (EST, version G9) software with multiple-scattering correction. Both the subtracted and deconvoluted valence EELS spectrum is fitted to equation 4.2:

$$y = y_0 + A(x - x_0)^P, \qquad \text{(eq. 4.2)}$$

where (x_0, y_0) are the band gap coordinates, A is the fitting parameter, and P is set for either direct or indirect band gap semiconductors.

An alternative to ZL removal is the Auger electron spectroscopy – reflective EELS (AES-EELS) linear fit method applied to STEM-EELS. With the linear fit method, the band gap is estimated without data manipulation by the intersection of two straight lines, one originating from the

background level and the other from the loss spectrum [125]. Park et al. showed that the linear fit method proved reliable for SiO_2, but not for SiN_x samples.

The ability to estimate nanowire band gaps and correlate it with structural information such as polytype is essential for designing state-of-the-art nanowire-based electronic devices. However, there are several artifacts in EELS imaging and analysis that render band gap determination difficult, such as beam size, sample thickness, delocalization phenomena, zero-loss deconvolution, and Cerenkov loss [125–127]. In addition, as mentioned earlier there are several methods to interpret EELS: ZL subtraction, ZL deconvolution, and linear fit model. Each method may result in a different band gap estimate, so it is vital to reaffirm a good fit with statistical data.

Nonetheless, attempts at band gap determination for SiC nanowires have been made. Minella et al. showed that cubic SiC nanowires with diameters 10 – 15 nm displayed band gap broadening. The SiC nanowire band gap was measured to be 5.5 eV, 0.9 eV higher than the experimental value of 4.6 eV obtained from bulk SiC [128]. Here, preliminary results show that the 4H-like SiC nanowires perform as hexagonal SiC, despite having few stacking faults that correspond to the cubic 3C polytype. Comparison is made between two ZL removal processes: subtraction and deconvolution.

Figure 4.8b shows the band gap fit to subtracted valence EEL spectrum. The fit parameters are A = 31.5, P = 1.5 (as SiC is an indirect band gap material) and yield a band gap of x_0 = 3.2 eV. This energy is higher than cubic (2.3 eV), but very close to that of hexagonal SiC (3.3 eV). Measuring valence EELS spectrum across 2 additional nanowires also yield band gap energies higher than the cubic polytype (Figure 4.9). The residual between the subtracted EEL spectrum and its corresponding band gap fit is also shown in Figures 4.8 and 4.9.

For this system, the ZL subtraction is more reliable than the ZL deconvolution method using GRAMS AI software. Comparison of the ZL removal methods of subtraction and deconvolution and the band gap fits are shown in Figure 4.10. Although the band fits of the deconvoluted data look plausible, the corresponding residual plots prove the fit unreliable in that there is a linear relationship in the residual plot near the band gap energy. No such pattern is seen with the band gap fits to the subtracted data.

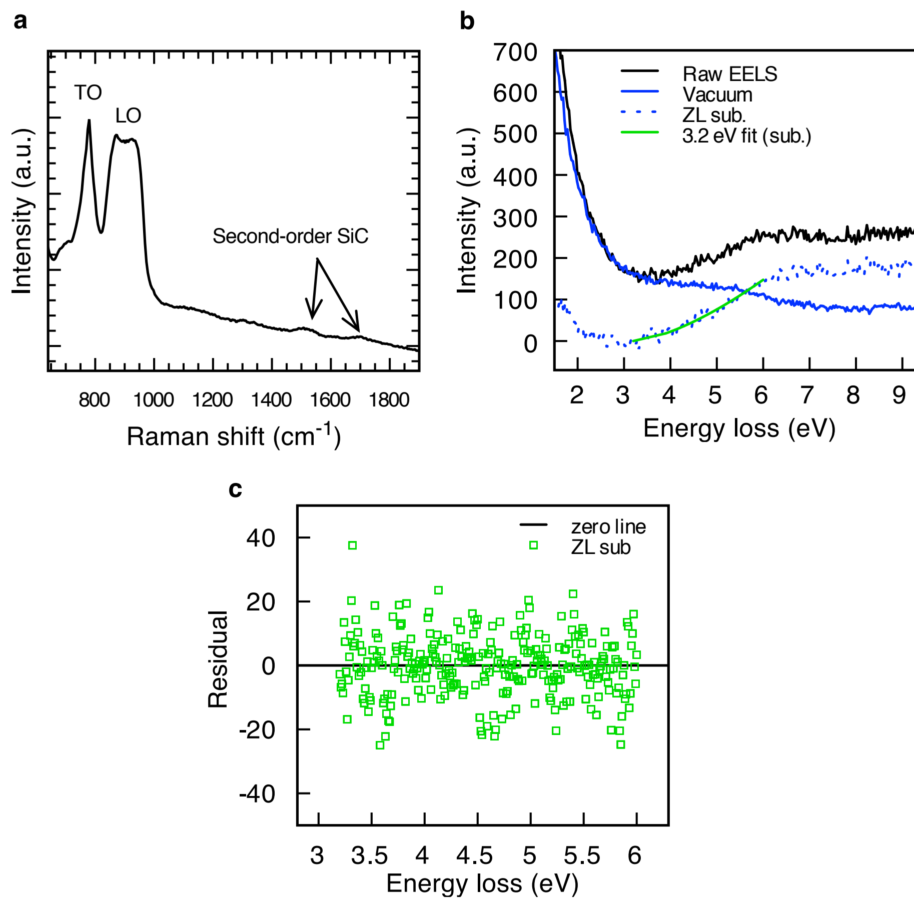

Figure 4.8. SiC structural and electronic hexagonality. (a) Raman spectrum of SiC nanowires with laser parallel to nanowire axis. (b) Raw EELS and valence EELS with ZL peak removed for nanowire #1. Band gap is estimated as 3.2 eV. (c) Corresponding residual plot between ZL subtracted data and model fit shown in b.

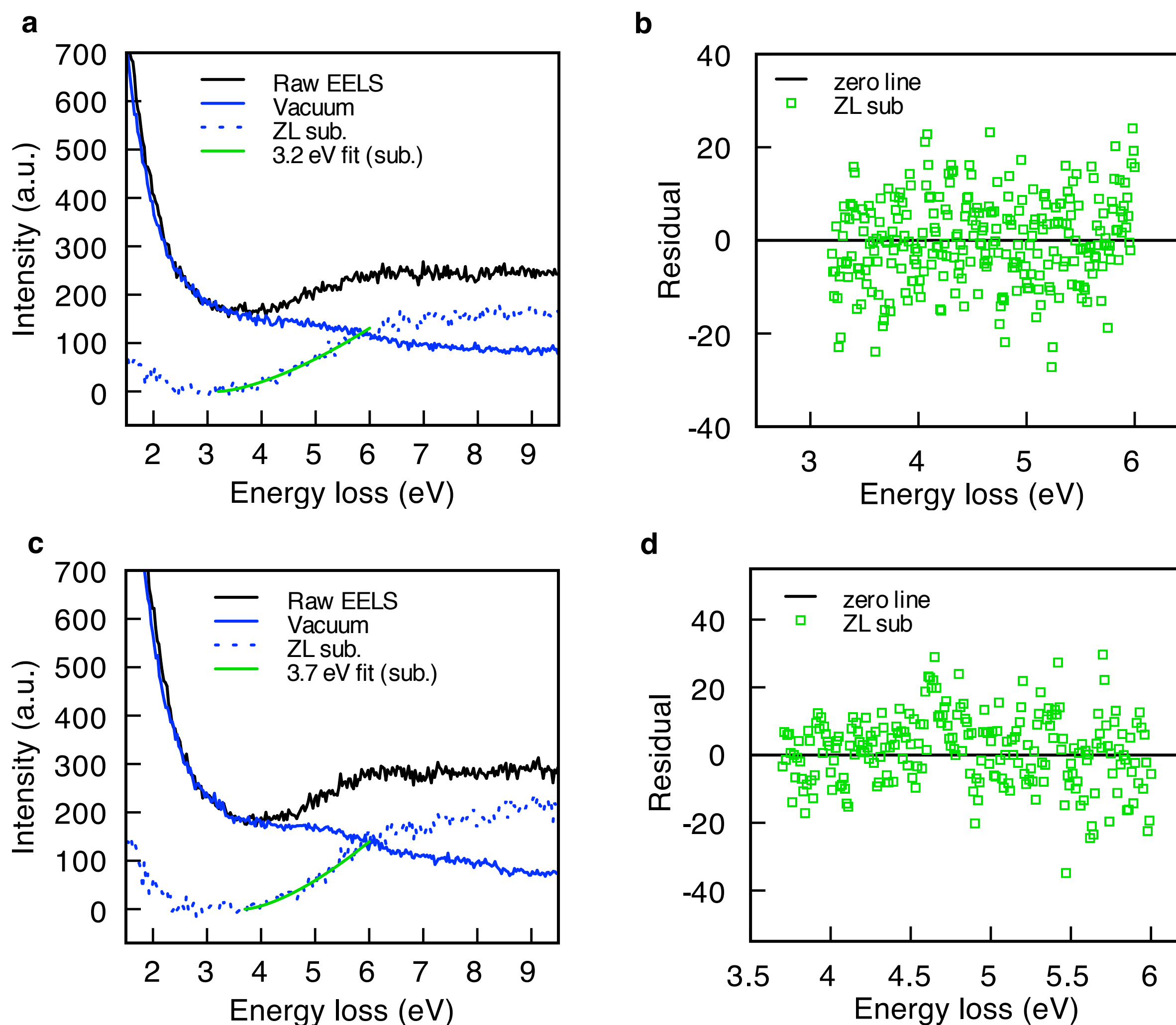

Figure 4.9. Band gap energy measurements on two distinct SiC nanowires. (a) Raw and ZL subtracted valence EELS spectra taken from SiC nanowire #2. Band gap fit to subtracted spectrum shown in green. Fit parameters are A = 28, P = 1.5, and x_0 = 3.2 eV. (b) Residual plot between ZL subtracted data and band gap fit shown in a. (c) Raw and ZL subtracted valence EELS spectra taken from SiC nanowire #3. Band gap fit to subtracted spectrum shown in green. Fit parameters are A = 40, P = 1.5, and x_0 = 3.7 eV. (d) Residual plot between ZL subtracted data and band gap fit shown in c.

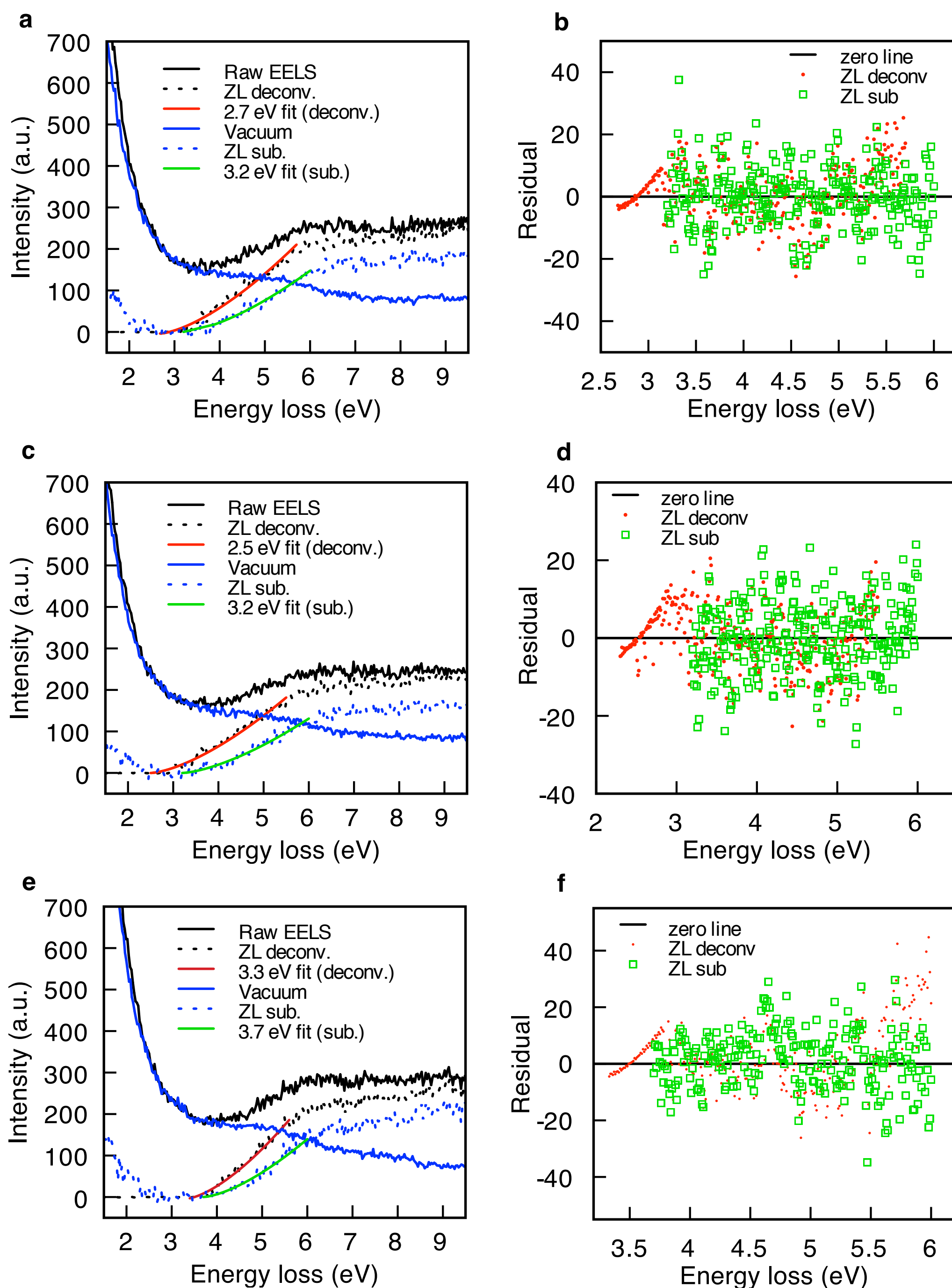

Figure 4.10. Comparison between ZL removal methods: subtraction and deconvolution. Superimposed residual plots from subtracted and deconvoluted data show that the subtraction method gives more reliable data, as the residual plot is random. (a-b) EELS spectra and residual plots from SiC nanowire #1. (b-c) EELS spectra and residual plots from SiC nanowire #2. (d-e)

EELS spectra and residual plots from SiC nanowire #3. *Note: SiC nanowire #1, 2, and 3 correspond to NW4, 3, and 8 in raw data files.

4.9. Summary

SiC nanowires grown in this work exhibit a hexagonal crystal structure that lies between the 4H and 2H polytypes. EEL spectra indicate that the 4H-like SiC nanowires perform as hexagonal SiC, despite having few stacking faults that correspond to the cubic 3C polytype. Strong experimental and theoretical evidence suggests that Ni_2Si clusters catalyze the growth, and that high supersaturation within the cluster promotes the hexagonal phase. Vertical alignment, induced by substrate, is achieved uniformly across the surface of high quality 4H-SiC (0001) substrates. These results demonstrate that substrate and precursor supersaturation within the catalyst affect SiC nanowire alignment and crystal structure, respectively. The connection between growth supersaturation, nanowire polytype, and substrate shown in this work serves as an additional stepping-stone towards targeting specific SiC nanowire polytype and alignment in efforts to expand the use of SiC nanostructures for robust electronics.

5. Catalyst cluster formation

5.1. Introduction

The state of the catalyst determines the growth mechanism as either vapor-liquid-solid (VLS) or vapor-solid-solid (VSS) (see Section 3.1). Previous chapters addressed investigative questions concerning Ni-assisted SiC nanowire growth with MTS. Chapter 3 described the growth of vertically aligned SiC nanowires on single crystalline 4H-SiC substrates. Chapter 4 used spectroscopy, microscopy, and modeling to elucidate that Ni_2Si catalytic cluster enables hexagonal phase SiC nanowire growth. The low C solubility within Ni_2Si supports the high-supersaturated state that is hypothesized to promote hexagonal SiC growth. However, still unanswered is the state of the catalyst, in particular whether it is a liquid or a solid. The primary nanowire growth temperature within this body of work is 950 °C, which was chosen based on nanowire crystallinity and aspect ratio (Section 3.4). Although there is no available Ni-Si-C phase diagram at this particular temperature, there are bulk phase diagrams that bracket 950 °C. These available phase diagrams are calculated for 900 and 1150 °C. The phase diagram at 900 °C shows no liquid phase, while the 1150 °C diagram shows one liquid phase with ~10% C solubility, but not for Ni_2Si (Figure 5.1).

The difference between bulk and nano-sized nickel silicide on SiC is also unclear. Bulk Ni_2Si melts at 1239 °C, thus it is expected to be solid during our growth process at 950 °C. In this work, after 4 min of nanowire growth, the Ni_2Si clusters are approximately 20 nm or less in diameter (Figure 5.2). Previous studies modeled the melting of small particle systems and showed significant melting temperature depression for indium and gold with radius less than 20 nm [129]. In systems alloys such as Cu-Pb and Cu-Bi, the melting temperature depression is signification for diameters of 40, 20, and 10 nm [130]. Lee et al. point out that since the substrate plays a role in interface and surface tension, the effect of substrates should be taken into account explicitly to fully understand changes in melting temperature [63]. The following sections investigate the state of the catalyst and its relationship with the substrate via ex-situ and in-situ studies.

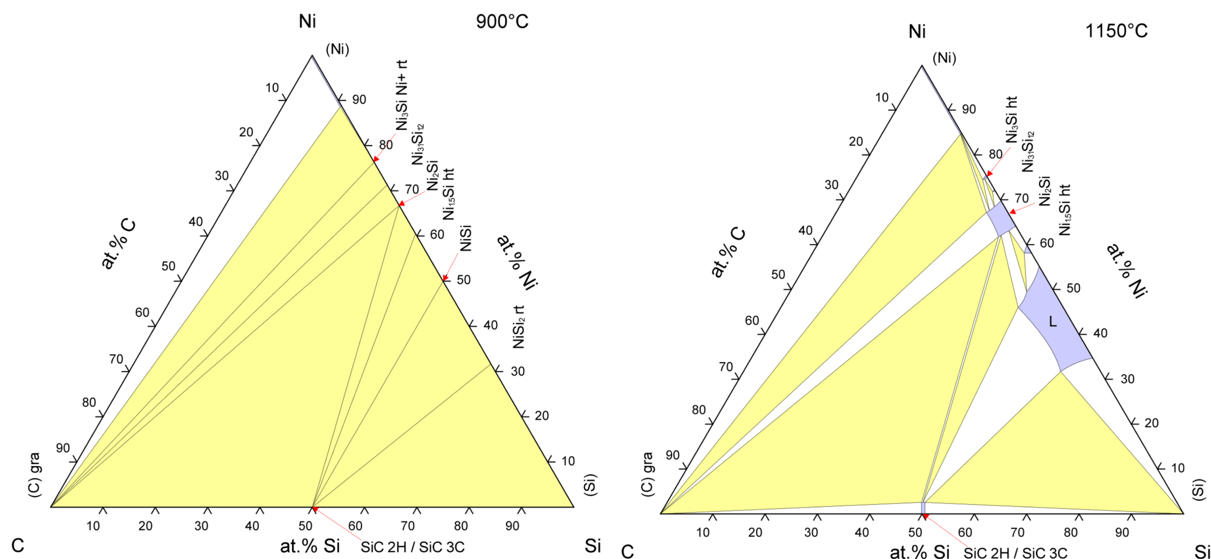

Figure 5.1. Phase diagram for Ni-Si-C ternary system at 900 and 1150 °C, reprinted by copyright permission from ASM International [131,132].

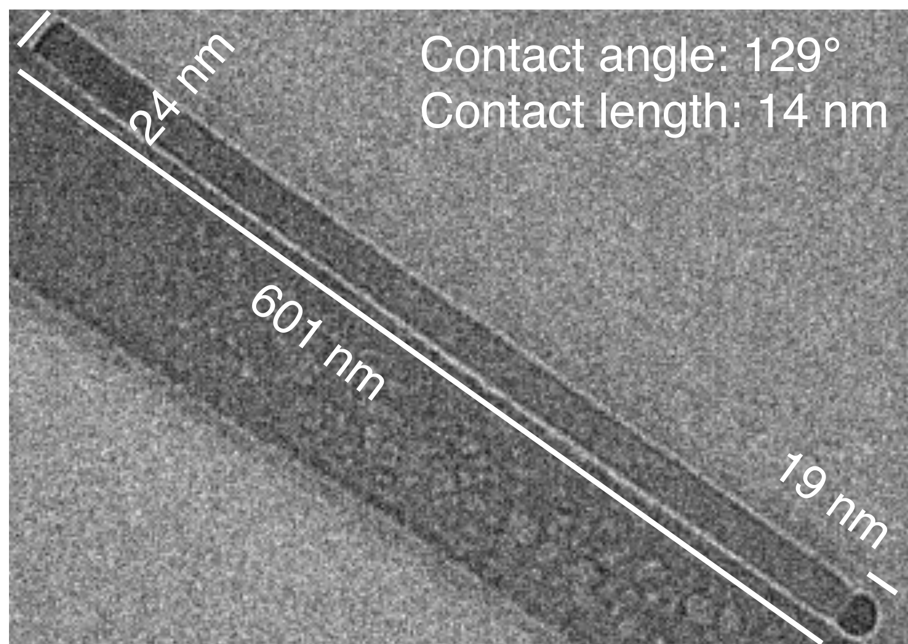

Figure 5.2. TEM image of SiC nanowire grown for 4 min on 4H-SiC (0001), purchased from Cree. The nanowire was sonicated in ethanol and drop casted onto TEM grid. The contact angle between nanowire and catalyst is 129° with a contact length of 14 nm.

5.2. Ex-situ studies of Ni-on-SiC

As shown in Chapter 3, upon heating a 2-nm Ni film on SiC (0001) at 950 °C, Ni_2Si clusters and excess C are evident. Below, the effects of temperature, pressure, and polytype are investigated using scanning transmission microscopy (SEM) and Raman spectroscopy.

5.2.1. Varying temperature

The transformation of the ~2 nm Ni film on SiC into Ni_2Si clusters is surveyed through a series of lower temperature anneals, starting from 150 °C. Raman spectrum after heat treatment at 150, 250, 350, 550, and 750 °C do not show significant differences from bare 4H-SiC until 550 °C (Figure 5.3). At 550 °C, there is a slight presence of C around 1310 cm^{-1} with no recognizable silicide signal. At 750 °C, both Ni_2Si and C signals are present. Top-view SEM images of annealed Ni-on-SiC samples show an island-like morphology as a result of film agglomeration. The formation of small circular islands occurs at temperatures much lower than the growth temperature and at temperatures that show no nickel silicide or C present via Raman (Figure 5.4). The islands get bigger as the temperature is increased to 350, 550, and 750 °C. This island formation below the melting point of thin metal films on a substrate is a result of surface energy minimization [133–135] and is well documented in thin metal films including Ni [136], Au [137], and Pt [138,139]. The phenomena of island formation or dewetting has also been used to transition patterned Au films to patterned arrays of nanoparticles on SiC [140]. At 550 and 750 °C, there are areas which are hypothesized to be the onset of Ni_2Si formation. Representative areas are highlighted in yellow. Increasing magnification reveals that the particles begin to disrupt SiC surface, comparable to the hexagonal pit formation discussed in Sections 3.5 and 3.8 (Figure 5.4f).

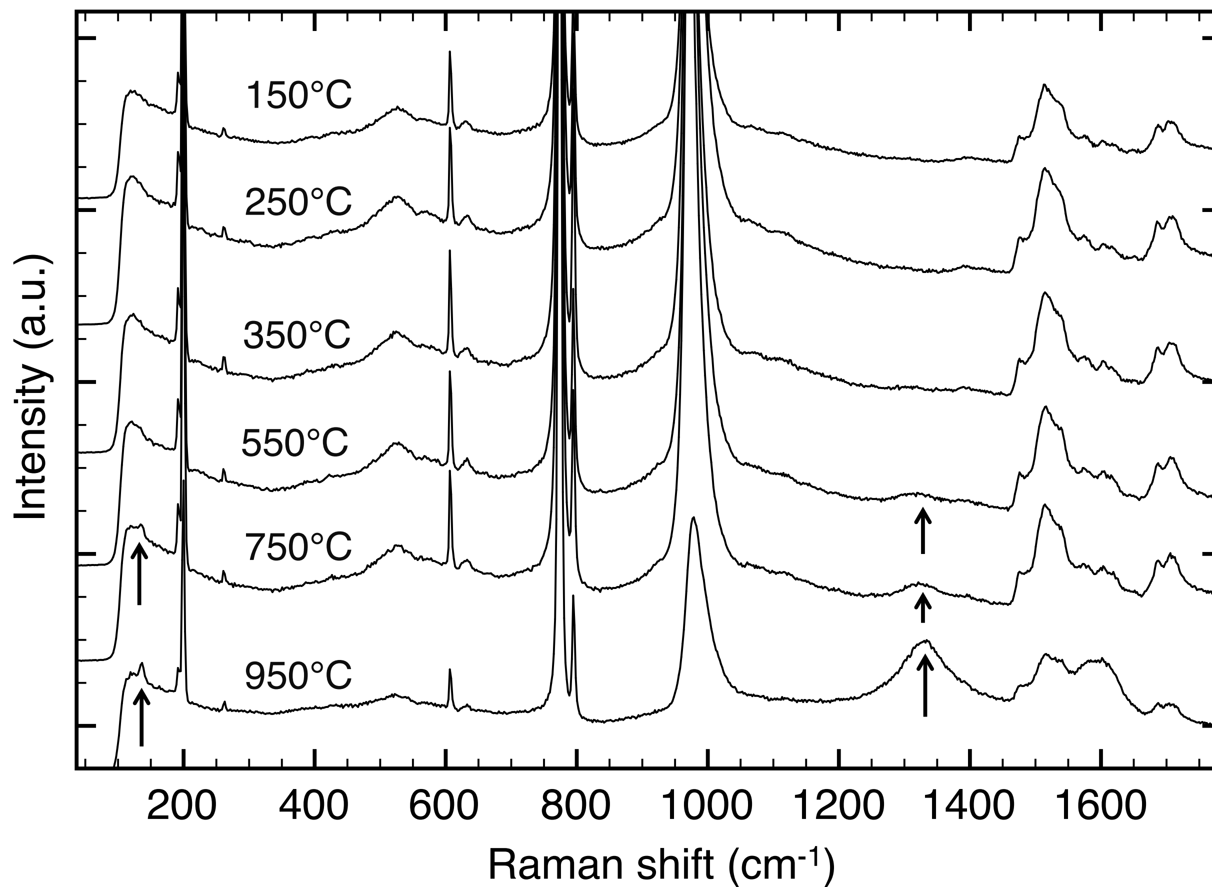

Figure 5.3. Raman spectra of ~2 nm Ni annealed on 4H-SiC (0001) for 10 min under 10 sccm H_2 at 5 Torr.

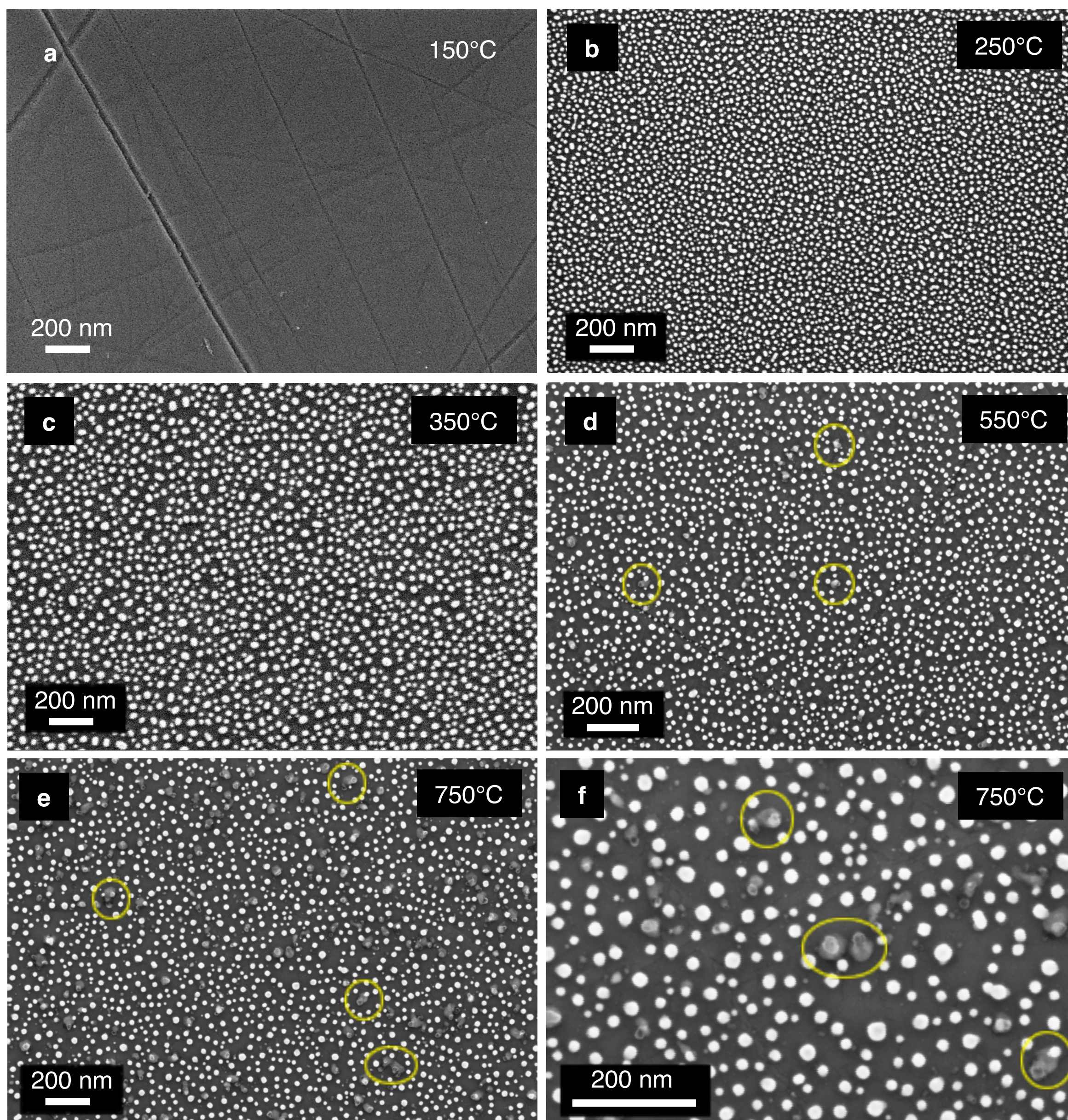

Figure 5.4. Top-view SEM images of ~2 nm Ni annealed on 4H-SiC (0001) for 10 min under 10 sccm H_2 at 5 Torr. The yellow highlights regions where circular particles are proposed to have begun reacting with the SiC to form Ni_2Si.

For a full temperature profile of Ni-on-SiC, temperatures above 950 °C were also explored. Based on the ternary Ni-Si-C phase diagrams, a liquid phase is present at 1150 °C (Figure 5.1). Ni-on-SiC samples were annealed to 1170 and 1200 °C to investigate if there is evidence of melting. Both of these samples do not show Ni_2Si Raman signals at 137 cm^{-1}, but preserve the C footprint at ~1310 and 1600 cm^{-1} (Figure 5.5a). The morphology of the surface at 1170 and

1200 °C differ from samples annealed to 950 °C (Figures 5.5 and 5.6). The SiC surface outside of the hexagonal-like features look more rough for the 1170 °C sample than the 950 °C sample (Figure 5.5 and 5.6). This roughening is likely from the increased production of C through solid-state graphitization of SiC and etching of SiC in H_2 at 1200 °C.

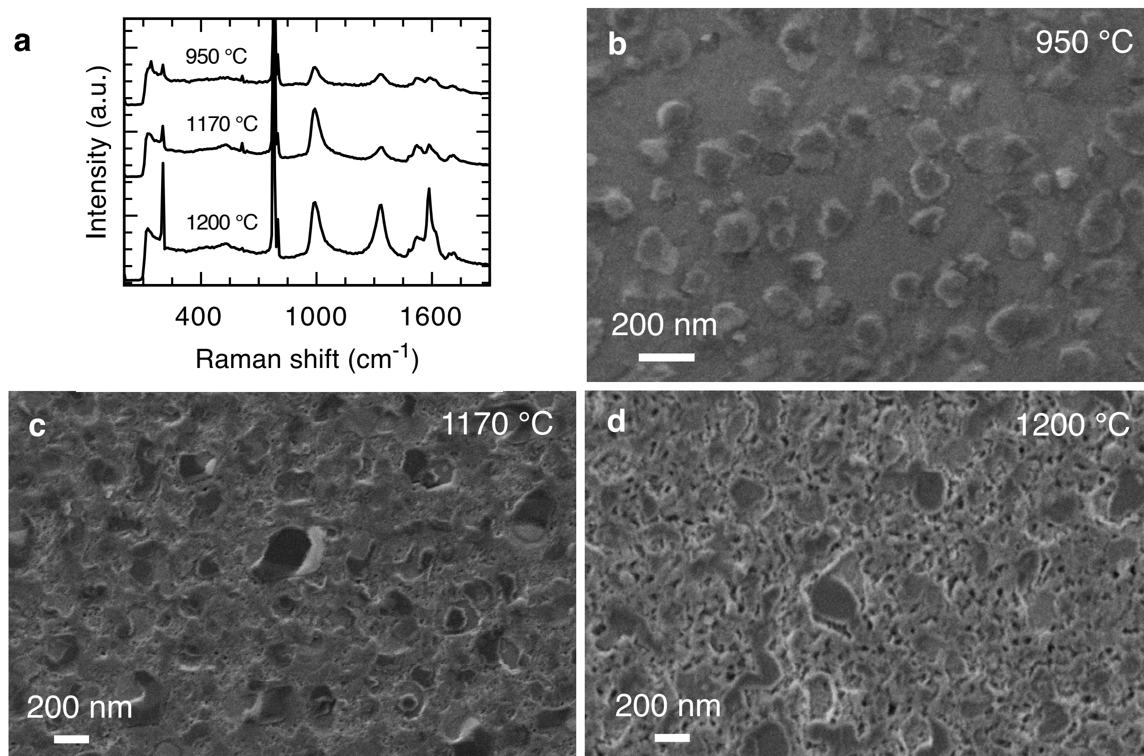

Figure 5.5. (a) Raman spectra of Ni-on-SiC annealed to 950, 1170, and 1200 °C for 10 min in 10 sccm H_2 at 5 Torr. (b-d) Corresponding top-view SEM images of annealed Ni-on-SiC.

Although surface roughness may affect cluster size and morphology, there is no observed pattern that would indicate Ni_2Si clusters prefer to nucleate at or away from the scratches at these conditions. Due to the increased C and possible decreased Ni content from evaporation at 1170 °C, microscopy imaging proves more difficult with charging of the substrate (Figure 5.6c-d). The 4H-SiC substrate charges under the electron beam as well, even though they are nitrogen doped. To overcome challenges with charging and avoid using additional metal film deposition to distribute charge on the samples, SEM at 1 - 2 keV accelerating voltage is used with fast acquisition scanning rates.

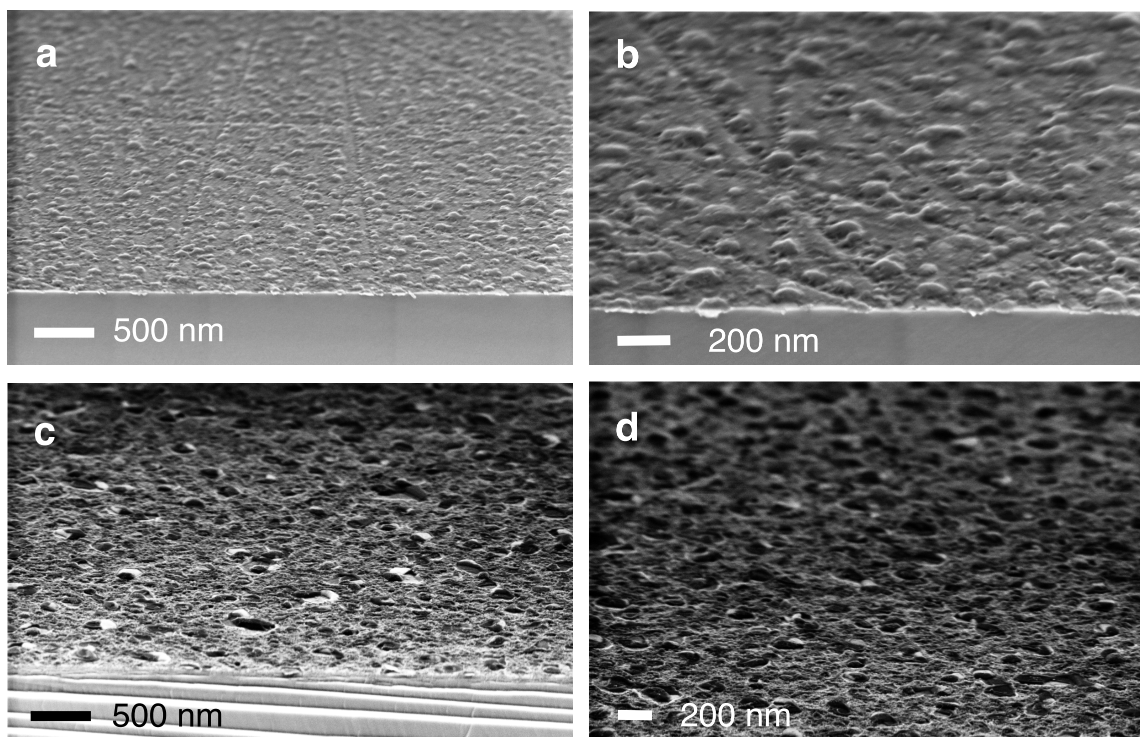

Figure 5.6. SEM of Ni_2Si clusters on 4H-SiC (0001) substrates. (a) Clusters formed after heating 2 nm Ni on SiC for 10 min at 950 °C under 10 sccm H_2 at 5 Torr. (b) Zoomed-in image of a. (c) Morphology formed after heating 2 nm Ni on SiC for 10 min at 1170 °C under 10 sccm H_2 at 5 Torr. The striations at the bottom of panel c are a result of the dicing process with a diamond cutter. (d) Zoomed-in image of c.

Rinses in acid baths of HF:HNO_3 and HCl:HNO_3 expose structured pits within the SiC. For the Ni-on-SiC samples heat-treated to 950 °C, a closer, angled look at the pits reveal that the bottom of the pits are flat with sharp boundaries (Figure 5.7). Likewise, the Ni-on-SiC samples heat-treated to 1170 °C also show a pits with flat bottom surfaces. Etching of anisotropic (triangular) pits on n-type 4H-SiC (without the use of nickel film) has been reported via photoelectrochemical methods, wherein crystallographic planes terminated with silicon atoms are more resistant to electrolytic attack than the planes terminated with carbon and mixed silicon-carbon atoms [141]. In addition to distinctive Raman spectra (Figure 5.5a), the 1170 °C samples have less sharp pit boundaries (Figure 5.7b,d). One possible explanation could be continued nickel silicide reaction with SiC, wherein the nickel silicide is melted, thus reacting more isotropically with the SiC planes perpendicular to the basal plane. The dark shadows visible in Figure 5.7 are due to charging of the surface as mentioned above.

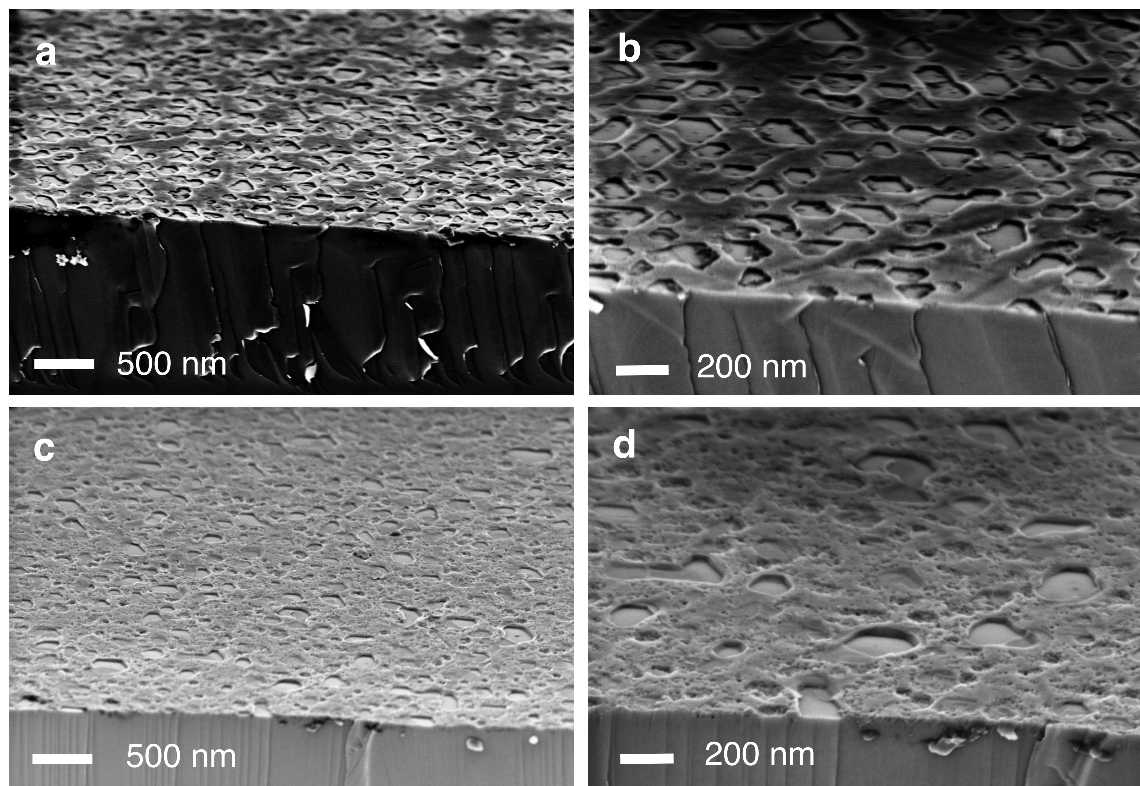

Figure 5.7. SEM of pits within 4H-SiC (0001) substrates. (a) Clusters formed after heating 2 nm Ni on SiC for 10 min at 950 °C under 10 sccm H_2 at 5 Torr were removed with 3:1 volume ratio of $HF:HNO_3$ and $HCl:HNO_3$. (b) Zoomed-in image of a. (c) Clusters formed after heating 2 nm Ni on SiC for 10 min at 1170 °C under 10 sccm H_2 were removed with 3:1 volume ratio of $HF:HNO_3$ and $HCl:HNO_3$. (d) Zoomed-in image of c.

5.2.2. Varying pressure

The system pressure within the CVD quartz tube furnace is varied to examine the effect of pressure on Ni_2Si cluster size. Backed by an Edwards 12 rotary mechanical pump, the base pressure of the furnace without gases flowing is approximately ~10 mTorr. The base pressure can be reached when the quartz tube is properly installed, such that the inlet is connected to desired gas lines and outlet is connected to the pump inlet. For the experiments in this dissertation, the base pressure is maintained at ~10 mTorr. In the event a good base pressure is not readily attainable, troubleshooting can be performed until ~10 mTorr is reached. Primary reasons for an inadequate pressure include: 1) Previous user routed the tube outlet to exhaust into the hood without using the pump, 2) The pump is low on oil, 3) The pump requires an oil change. The use of chlorinated precursor MTS is hard on the pump and thus frequent MTS use requires more regular oil changes to prevent pump from underperforming and overheating. 4) Less likely is that the convectron gauge needs to be recalibrated. All of the above can be addressed to

reached a base pressure of ~10 mTorr. 5) The pump may require extensive cleaning. This procedure includes: emptying used oil from pump, disassembling pump to expose oil-containing unit, using paper towels and acetone (on non plastic pieces) to wipe up the materials built-up within the pump. If a good pressure is not attainable even after pump cleaning, a rebuild kit wherein all rotary vanes, o-rings, gaskets, etc are replaced might be necessary.

Before ramping to 950 °C under 10 sccm H_2, the speed valve located between the tube outlet and pump inlet is closed until convectron pressure gauge reads stable desired pressure. In previous chapters, all experimental set-ups used 5 Torr for nanowire growth and cluster analysis. To investigate the effect of pressure on cluster size, 1 and 12 Torr were chosen as they bracket 5 Torr (Figure 5.8). From these preliminary experiments, there is a clear increase in cluster size with increased pressure. This trend has been reported previously for thin nickel films annealed in hydrogen at 600 °C at 2.5 and 20 Torr [142]. Thus, pressure could be used to control nanowire density as long as MTS decomposition is not negatively affected with increased pressure.

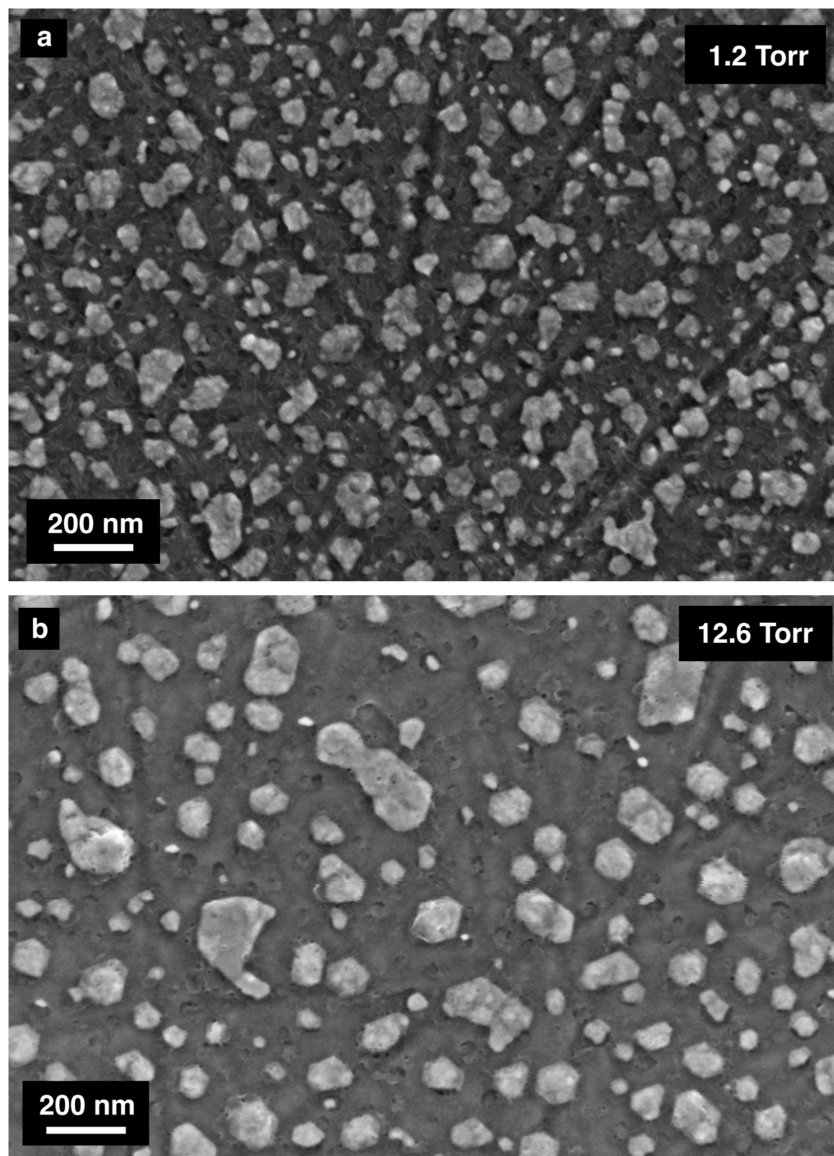

Figure 5.8. SEM of Ni_2Si clusters on 4H-SiC (0001) substrates. (a) Clusters formed after heating 2 nm Ni on SiC for 10 min at 950 °C under 10 sccm H_2 at 1.2 Torr. (b) Clusters formed after heating 2 nm Ni on SiC for 10 min at 950 °C under 10 sccm H_2 at 12.6 Torr.

5.2.3. Polytype

Substrate pitting occurs from Si atoms in the SiC substrate reacting to form Ni_2Si with the deposited Ni thin film. The shape of the pit depends on Si atom arrangement within the plane exposed to the Ni thin film. The cubic (100) plane, similar to the cubic (001) plane in terms of atomic arrangement, has Si atoms arranged in squares relative to each other [143]. The hexagonal (0001) closed-packed plane, equivalent to the cubic (111) closed-packed plane, has Si atoms arranged in hexagons relative to each other [143]. In agreement with the orientation of exposed Si atoms in the SiC substrate, we observed hexagonal pitting in the hexagonal (4H-SiC (0001)) as shown in Figures 5.5 - 5.8 and rectangular pitting in the cubic (3C-SiC (100)) substrate as shown in Figure 5.9.

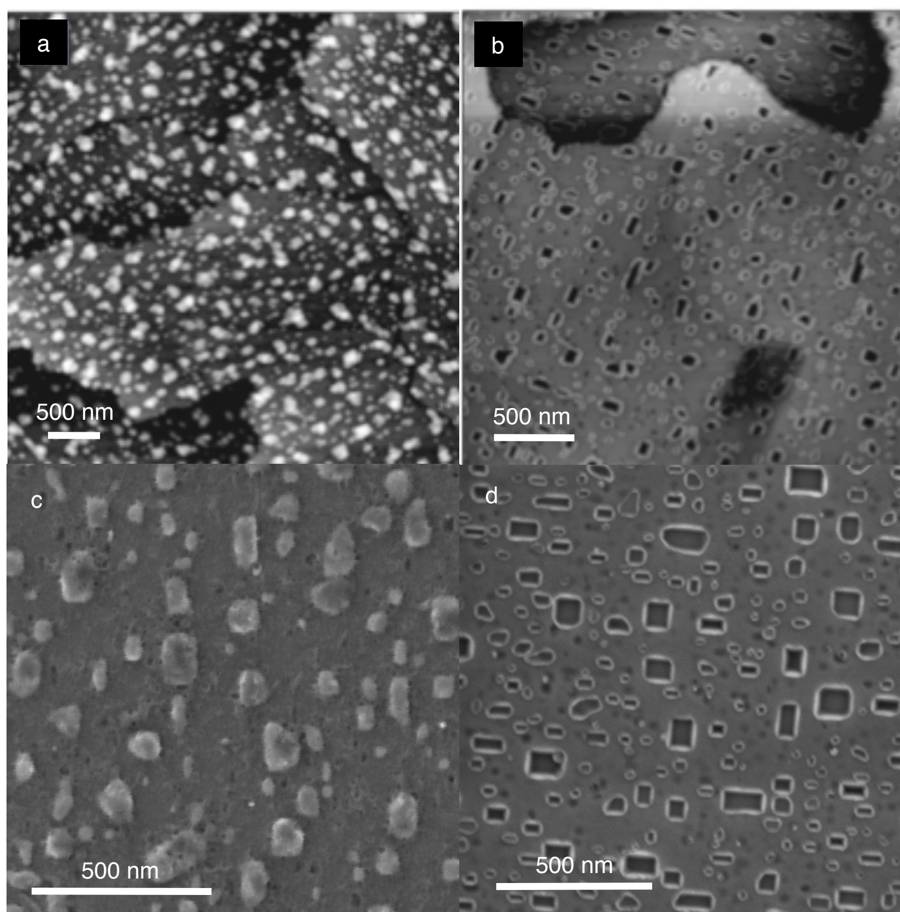

Figure 5.9. Substrate's crystal structure affects pit shape. (a) AFM of annealed Ni on 3C-SiC (100) results in rectangular-like Ni_2Si clusters (b) Pits revealed with silicide removal of sample shown in a. (c-d) High magnification SEM images show clearer rectangular silicide and pits, respectively.

5.2.4. Preliminary cross-sectional TEM

SEM images of Ni_2Si clusters on SiC substrates shown so far are limited to morphological characterization. Using cross-sectional TEM, the crystalline relationship between cluster and SiC can be identified. Preparation of a cross-sectional Ni_2Si/SiC TEM sample requires several mechanical processing steps. The primary goal of the mechanical processing is shown in Figure 5.10 as a simplified schematic. A detailed process flow to create a cross-sectional electron transparent sample is described in Appendix A.

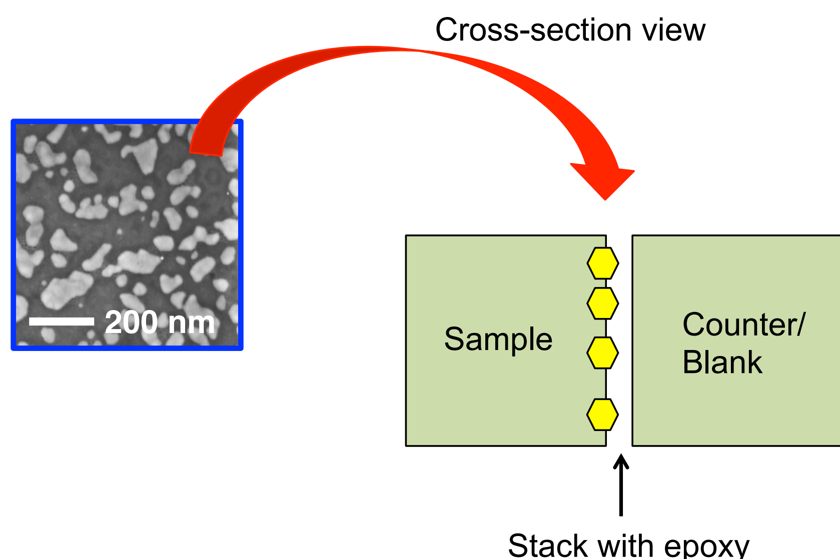

Figure 5.10. Simplified schematic showing the overall idea of cross-sectional TEM sample preparation.

Sandwiching the Ni_2Si clusters / 4H-SiC (0001) with a 4H-SiC (0001) counter coupon increased the time needed to ion mill a hole in the center of the stack (Figure 5.10, Appendix A). Longer etch time for SiC also equates to longer etch time for the epoxy/glue line. Etching through two SiC substrates etched most of the glue and left the surface of interest vulnerable to contamination or redeposition of Si or SiC (Figure 5.11). To remove redeposition, additional ion milling is used. Future experiments with a Si counter may be more effective at maintaining a good glue line during the ion milling process. Also, since Si ion mills at a faster rate than SiC, one could etch from the SiC side to prevent etching away too much Si.

Figure 5.12 shows the lattice plane resolution of a nickel silicide cluster on 4H-SiC (0001). The dark bands visible between the catalyst and substrate could be overlapping crystal structures. More analysis is needed to determine the crystalline relationship between the cluster and substrate.

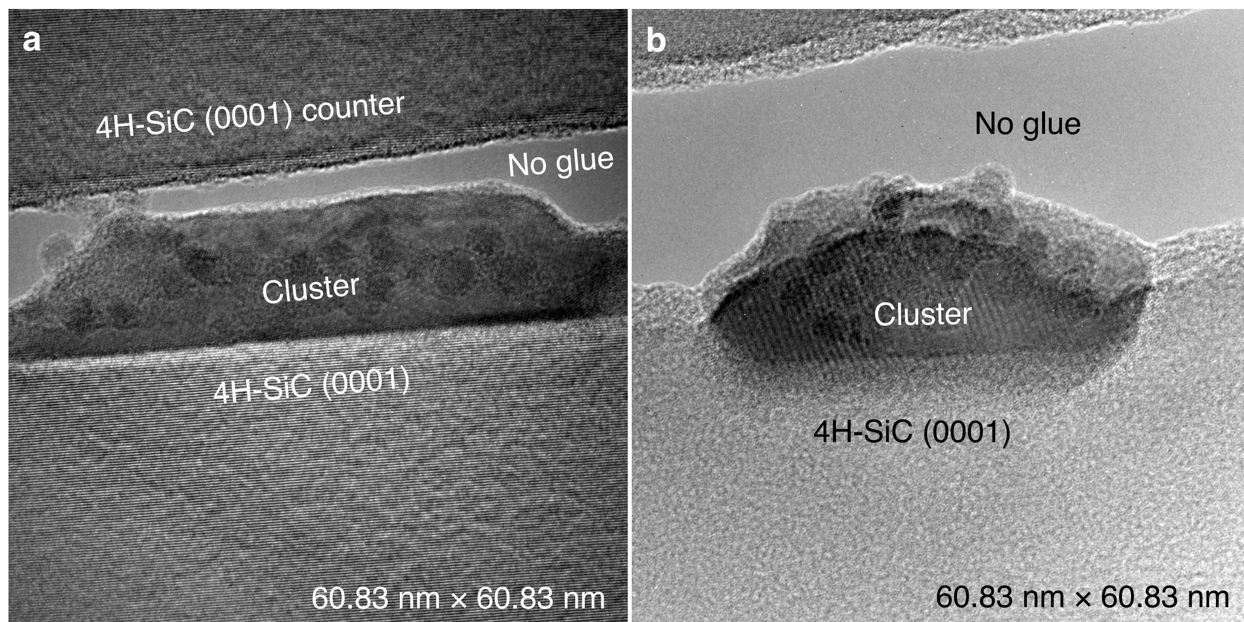

Figure 5.11. TEM micrographs showing no glue coverage around cluster. The smaller crystalline spherical particles on cluster are indicative of contamination of redeposition.

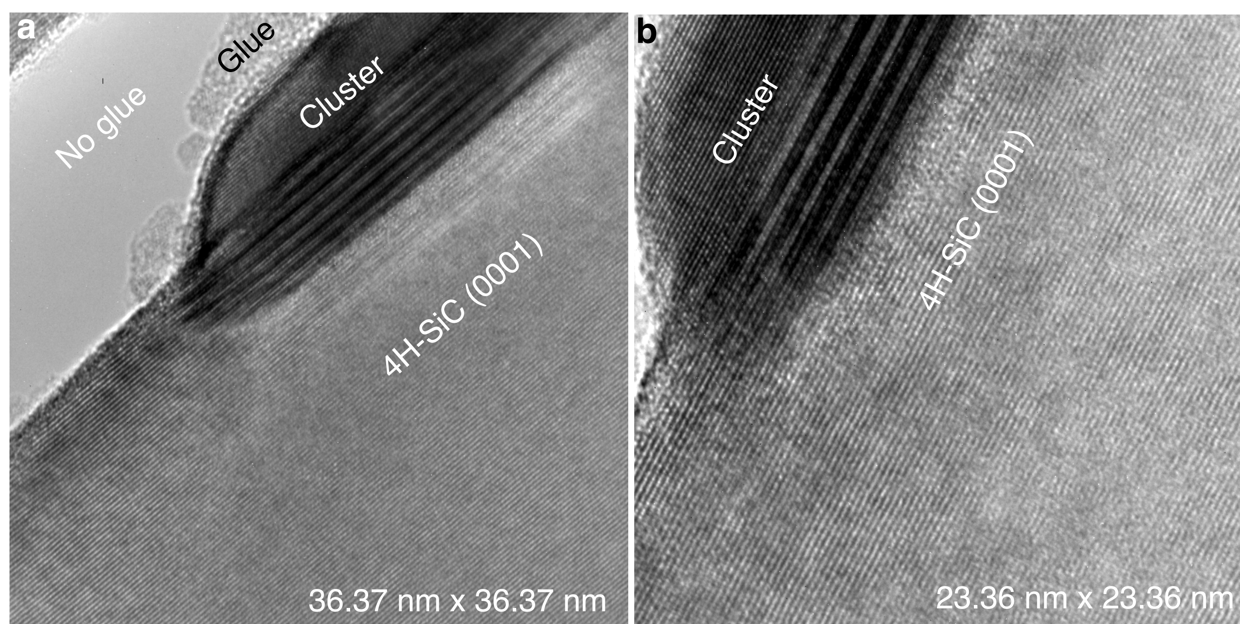

Figure 5.12. TEM micrographs showing glue surrounding cluster. No contamination or redeposition is seen.

5.3. Preliminary low energy electron microscopy (LEEM) studies of Ni-on-SiC

Broadly speaking, microscopy techniques (SEM and TEM) serve different purposes and thus have different operating conditions. In this work, SEM operating at 1 - 2 kV provides morphological information, while TEM operating at 200 - 300 kV elucidates crystalline relationships. A remaining question concerning this SiC nanowire growth system is whether the nickel silicide clusters are liquid or solid during nanowire growth. To answer this question, an in-situ technique is necessary to monitor the crystalline phases or lack thereof during anneal and growth. Two in-situ techniques include TEM [53] and low-energy electron microscopy (LEEM) [144]. LEEM is a surface technique that uses very low accelerating voltages (0 - 20 V) compared to SEM and TEM to investigate various surface dynamics [145]. This section describes preliminary heating studies of Ni-on-SiC within a LEEM chamber.

5.3.1. Temperature calibration

For in-situ heating, the sample temperature must be known and controlled. Si has been studied extensively in LEEM chambers and has identifiable transitions that can serve to calibrate the temperature at the sample surface [144]. A Si (111) substrate is used to calibrate the temperature at the sample surface (Figure 5.13). The sample of interest for these experiments is Ni-on-SiC. The use of epitaxial 3C-SiC on Si (111) would enable better estimate of surface temperature based on the well-known temperature controlled Si (111) phase transitions. However, for these preliminary studies, off-axis 4H-SiC is used instead of the epitaxial 3C-SiC for comparison with the near atmosphere tube furnace experiments described in previous chapters.

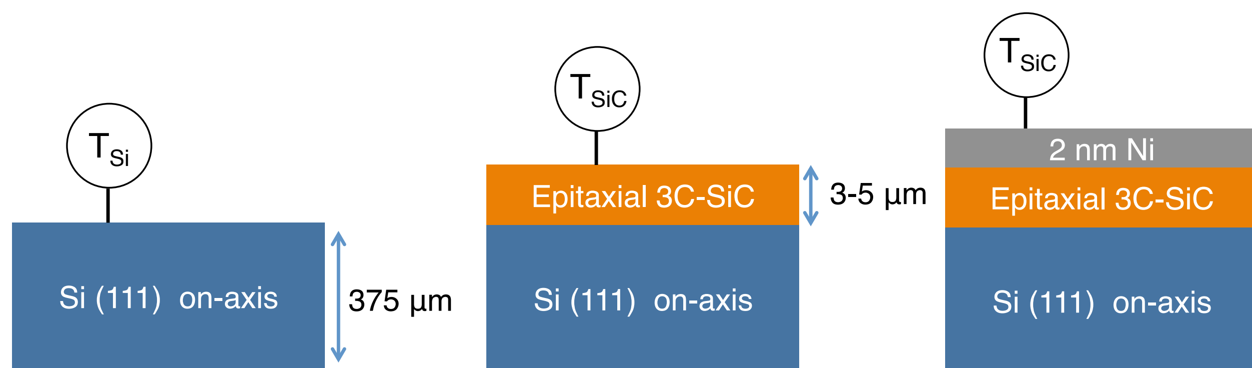

Figure 5.13. Temperature calibration using well-studied Si (111). The assumption here is the $T_{Si} \approx T_{SiC} \approx T_{Ni}$.

5.3.2. Mimicking ex-situ experiments with in-situ LEEM

In previous chapters, the standard substrate was 4H-SiC (0001) with a 4° off-axis cut towards <1120>. The high angle off-axis cut poses a problem for LEEM. For good imaging, the substrate needs to be positioned to maximize electron reflection close to 0 V and is easily attainable with on-axis samples. The LEEM sample holder does have the ability to tilt to overcome an off-axis cut, but not enough for ideal imaging with 4° off-axis substrate. Given this drawback, the intensity profile of electron reflection as a function of starting voltage was not obtained. Instead, LEEM was used to identify morphological and contrast changes due to temperature.

LEEM requires ultra-high vacuum (UHV) and extremely clean surfaces to image well with low accelerating voltages (0 - 20 V). Thus, the tube furnace experiments described in Chapter 4 can only be reproduced in principal, but not in exactness. The base pressure in the LEEM chamber is 1×10^{-11} Torr, whereas the base pressure in the hot-wall CVD quartz tube furnace is 20×10^{-3} Torr. Another difference is that hydrogen was not introduced into the LEEM chamber, contrary to the 10 sccm of hydrogen used in the tube furnace. To achieve a clean surface, 10 mm × 10 mm SiC coupons were loaded in a UHV cleaning chamber connected to the LEEM chamber and heated to 500 - 600° for 10 min with 500 V. A more aggressive cleaning was avoided to prevent graphitic carbon on the surface [146]. Once cleaned, the sample was transferred to the LEEM chamber for Ni evaporation (28 W) and subsequent heating experiments.

The LEEM projector lens gives a circular screen view of radius ~12 μm, which makes it difficult to view the expected high density of nanometer-sized nickel silicide clusters with good resolution (Figure 3.6). After deposition of 2 nm Ni and subsequent annealing to 950 °C in the LEEM, small clusters formed (~100-200 nm in diameter), but they can not be imaged clearly due to the resolution limitations of the microscope. Another 3 nm Ni was added to this sample and annealed again to 950 °C in hopes to produce larger clusters. Although the nickel silicide particles were larger, the 2 nm + 3 nm sample showed a morphology vastly different from the 2 nm furnace-annealed samples (Figure 3.6, 5.14a). Due to these morphological differences and the low resolution of the LEEM, new samples were fabricated in attempt to make larger nickel silicide clusters with increased Ni thickness of 3 and 7 nm. The 3 and 7 nm Ni on SiC samples annealed in UHV do not exhibit a hexagonal-like shape and prefer to aggregate at the surface scratches from industrial chemical mechanical polishing (Figure 5.14). This is in contrast to the furnace-annealed samples that form hexagonal-like shaped nickel silicide clusters that do not show a preference for aggregation at the scratches (Figures 5.6a-b, 5.8). Overall, larger clusters were achieved with increased Ni thickness.

To isolate a single nickel silicide cluster that is large enough to resolve in the LEEM, spherical Ni powder (diameter range from 80-150 nm) is used. The idea here is to monitor the interaction of a single Ni particle and the SiC substrate. Such studies could indicate how SiC in contact and not in contact with the Ni differ upon heat treatment. The Ni was dispersed on clean 4H-SiC substrates with nitrogen gas in the fume hood (Figure 5.15a). Heating the Ni-on-SiC to approximately 950 °C in the LEEM chamber resulted in a halo formation with bright contrast surrounding the Ni/Ni silicide cluster (Figure 5.15b).

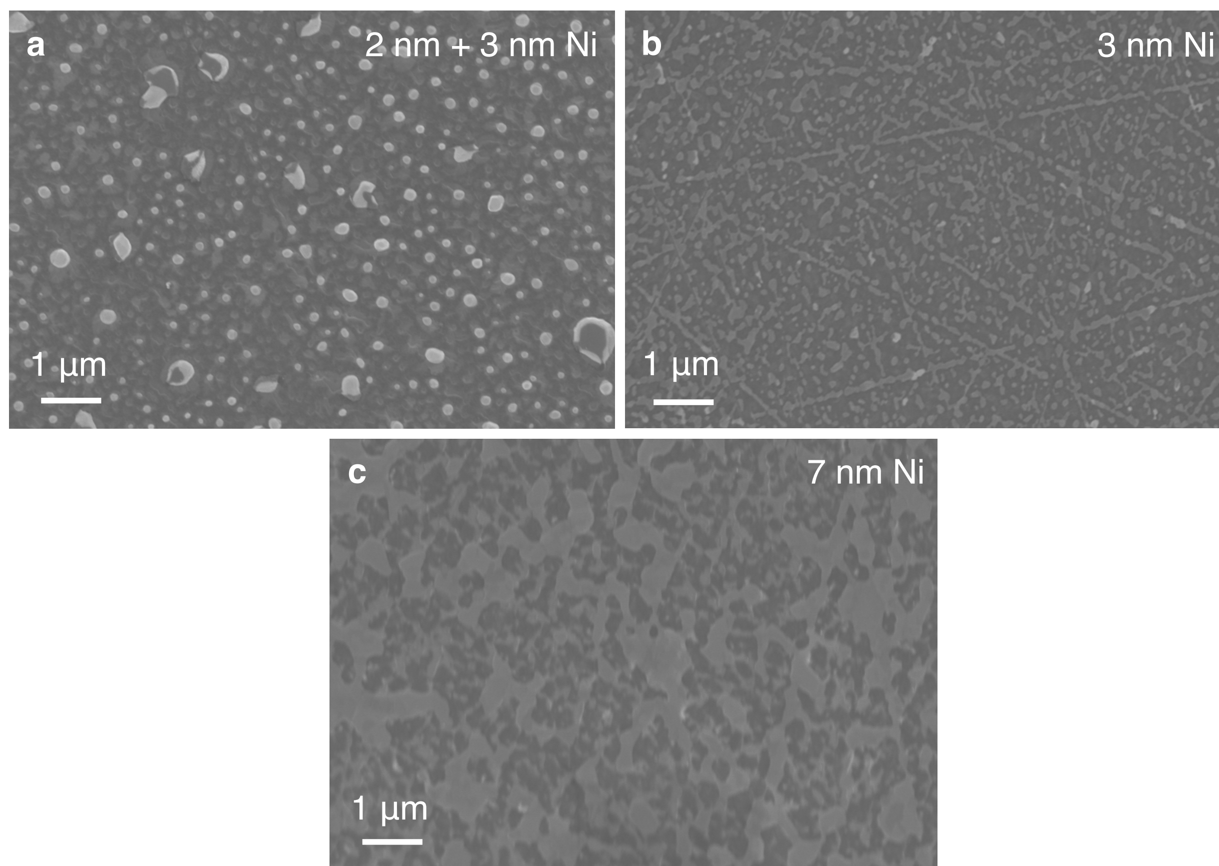

Figure 5.14. SEM of nickel silicide morphology on 4H-SiC (0001) annealed in UHV. Samples were annealed in UHV LEEM chamber to 950 °C.

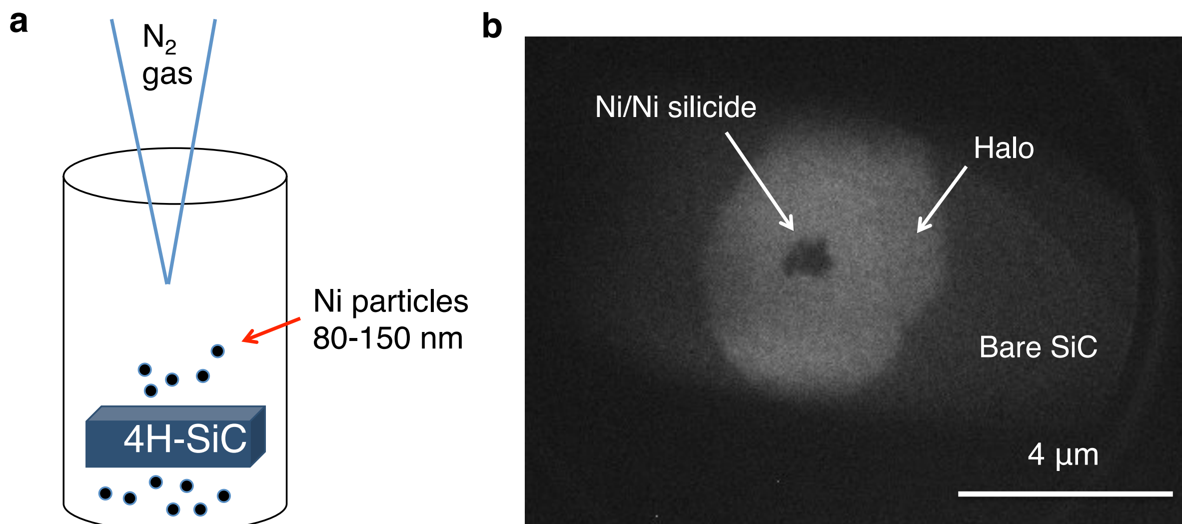

Figure 5.15. Large Ni particles can be imaged clearly in the LEEM. (a) Spherical Ni powder was used to deposit particles of Ni onto SiC in the fume hood. (b) Halo formation on SiC as a result of heating Ni-on-SiC to ~ 950 °C.

The halo formation occurred at a temperature possibly lower than 950 °C. The uncertainty of temperature stems from the thermocouple readout error and the fact that the temperature calibration was done with Si (111), instead of 4H-SiC (0001). A time series was taken to capture halo growth around the Ni particle when heated in the LEEM (Figure 5.16). The sample temperature was stabilized to ~ 850 °C for 20 min, corresponding to t = 0 s. The sample surface at room temperature and 850 °C look similar. Time t > 0 s marks the onset of additional heating to ~855 °C. From the time snapshots in Figure 5.16, it is evident that there are two types of halo formation: 1) A bright contrast halo immediately surrounding Ni/Ni silicide, 2) A dark contrast halo surrounding the bright halo (Figure 5.16b). Additionally, the halo growth is affected by the larger SiC surface scratches and lasts approximately 22 s.

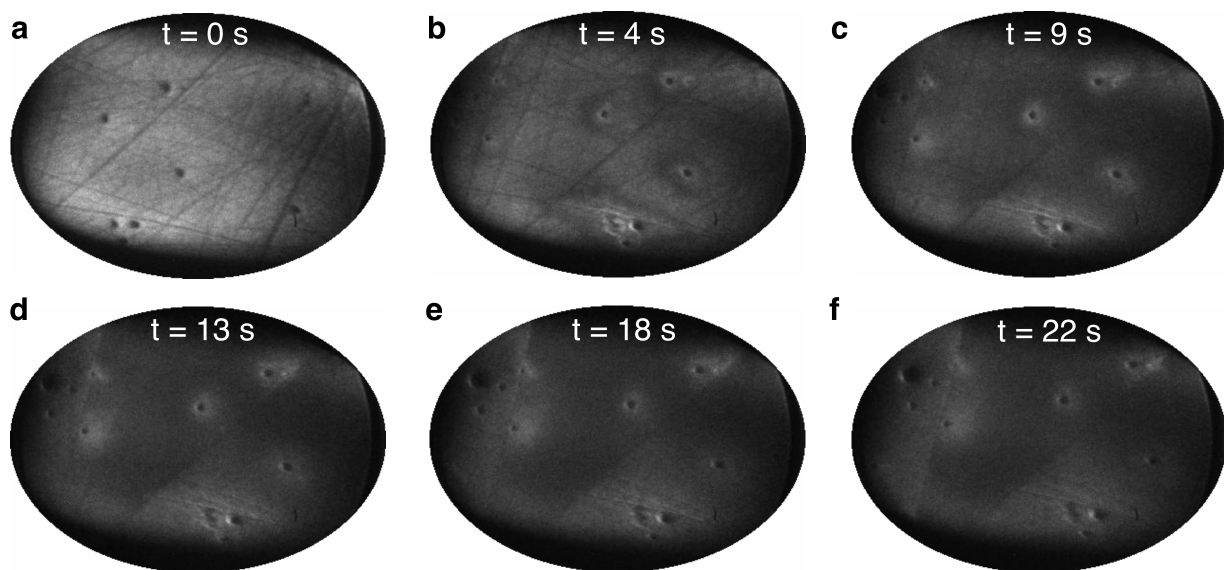

Figure 5.16. Time series of LEEM images. Time t = 0 s corresponds to ~850 °C and t > 0 s shows heating to ~855 °C. The major axis in all images is 12 μm.

Raman x-y mapping reveal that the bright contrast halo consists of nickel silicide and C, just like the cluster itself (Figure 5.17). The bright or dark contrast halos could be a result of a SiC surface reconstruction (Appendix B). Further studies are needed to identify the mechanism of halo growth and its implications on nickel silicide cluster formation on 4H-SiC (0001).

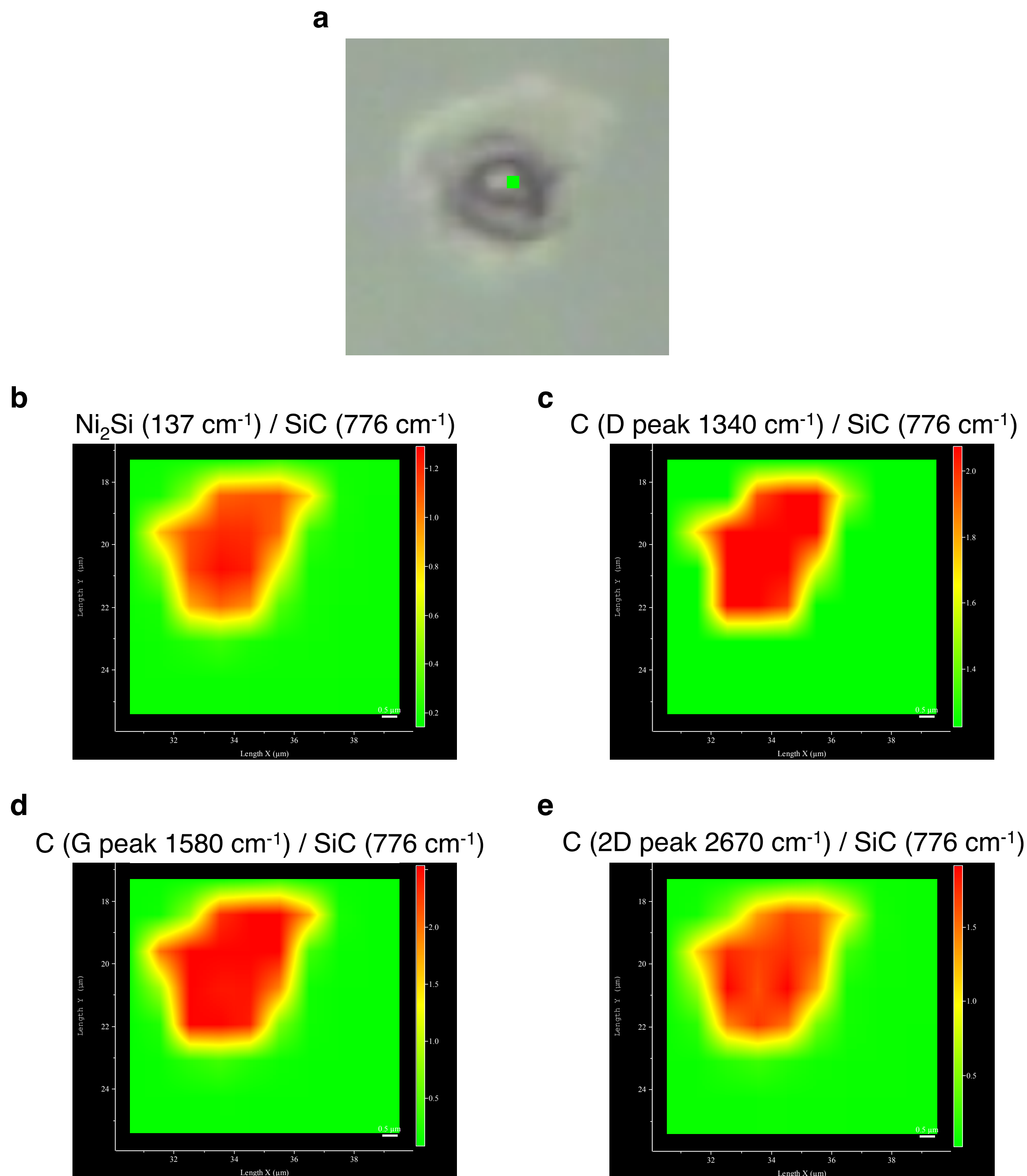

Figure 5.17. Raman x-y mapping of spherical Ni powder annealed on SiC to ~ 855 °C in UHV. (a) Optical micrograph annealed Ni-on-SiC. Equivalent radius of particle is 3 μm. The bright green square indicates laser alignment. (b-e) Color intensity maps of Ni_2Si, C (D peak), C (G peak) and C (2D peak) with respect to the primary 4H-SiC signal. Red, yellow, and green indicate high, intermediate, and low intensity ratios.

5.4. Summary

Control of the cluster formation, size, shape, and distribution of Ni annealed on SiC is essential for patterned SiC nanowire growth. Ex-situ studies of Ni-on-SiC reveal several findings that affect Ni-induced silicon carbide nanowire growth on SiC substrates. Annealing thin Ni films on SiC in hydrogen at the nanowire growth pressure of 5 Torr shows evidence of cluster formation below the bulk Ni and Ni_2Si melting temperature (1455 °C and 1239 °C) and below the expected bulk Ni_2Si formation (~500 °C). Additionally, during the anneal, the system pressure can be used to change the size of the clusters formed on SiC, whereas SiC substrate polytype can be used to dictate the shape of the clusters.

Preliminary in-situ LEEM studies give a different perspective of the Ni-on-SiC system. As LEEM is surface sensitive, utilizing low accelerating voltages (0 - 20 eV), the interaction between the Ni and SiC at elevated temperatures is identified by spreading fronts in the form of halos surrounding the original Ni particle. Time snapshots during heating show that the surface scratches on SiC affect the spreading or halo formation. Ex-situ Raman confirms that the inner halo is composed of Ni_2Si. The outer halo is only visible in the LEEM and could be the result of another surface phenomena, such as SiC reconstruction.

6. Conclusions and future work

Silicon carbide (SiC) has great potential for innovative harsh-environment devices, but faces challenges in terms SiC film stability when in contact with metals at high temperatures and polytype control for SiC nanomaterials. This dissertation presents efforts to address these challenges by way of introducing a SiC metallization scheme that can withstand prolonged exposure to high temperature in air, and by introducing methods to achieve vertically aligned 4H-like SiC nanowires. The growth of 4H-like SiC nanowires is further investigated by analyzing the effect of growth parameters on the catalyst formation prior to nanowire growth. Electronic characterization of the 4H-like SiC nanowires is also discussed.

Nanowire placement relies on the ability to control nickel silicide cluster agglomeration on SiC substrates prior to nanowire growth, not yet established using the chemical vapor deposition growth method employed in this work. Control of the cluster formation, size, shape, and distribution of nickel annealed on SiC is essential for patterned SiC nanowire growth. Thus, expansion on the nanowire vertical alignment to incorporate periodic or user-defined nanowire placement on industry standard SiC substrate remains an area of interest. Further areas of study include in-depth in-situ heating studies of Ni-on-SiC to identify the state of the nickel silicide catalyst at the nanowire growth temperature. The catalyst state informs the nanowire growth mechanism which affects nanowire morphology, dopant concentration, and polytype. Continued research efforts to understand and characterize SiC nanomaterials will expand the possibilities towards applications in electrical, mechanical, biomedical, and optical nanodevices.

Bibliography

[1] W.R. Ashurst, M.B.J. Wijesundara, C. Carraro, R. Maboudian. Tribological impact of SiC encapsulation of released polycrystalline silicon microstructures. *Tribol. Lett.* 17 (2004) 195–198. doi:10.1023/B:TRIL.0000032445.01193.19.

[2] C.R. Stoldt, C. Carraro, W.R. Ashurst, D. Gao, R.T. Howe, R. Maboudian. A low-temperature CVD process for silicon carbide MEMS. *Sensors Actuators A Phys.* 97-98 (2002) 410–415. doi:10.1016/S0924-4247(01)00810-X.

[3] C. Hehrlein. Stent passivation with silicon carbide as a possible alternative to drug-eluting stents – a comprehensive review of pre-clinical and clinical results. *Interv. Cardiol. Rev.* 4 (2009) 60. doi:10.15420/icr.2009.4.1.60.

[4] C.L. Frewin, C. Locke, S.E. Saddow, E.J. Weeber. Single-crystal cubic silicon carbide: an in vivo biocompatible semiconductor for brain machine interface devices. *Annu. Int. Conf. IEEE Eng. Med. Biol. Soc.* 2011, pp. 2957–2960. doi:10.1109/IEMBS.2011.6090582.

[5] D. Gao, M.B.J. Wijesundara, C. Carraro, R.T. Howe, R. Maboudian. Recent progress toward a manufacturable polycrystalline SiC surface micromachining technology. *IEEE Sens. J.* 4 (2004) 441–448. doi:10.1109/JSEN.2004.828859.

[6] S. Chen, L.E. Luna, Z. You, C. Carraro, R. Maboudian. Ni-induced graphitization for enhanced long-term stability of ohmic contact to polycrystalline 3C-SiC. *J. Vac. Sci. Technol. A* 33 (2015) 031507. doi:10.1116/1.4916578.

[7] F. Liu, C. Carraro, A.P. Pisano, R. Maboudian. Growth and characterization of nitrogen-doped polycrystalline 3C-SiC thin films for harsh environment MEMS applications. *J. Micromech. Microeng*. 20 (2010) 035011. doi:10.1088/0960-1317/20/3/035011.

[8] R.V. K. G. Thirumalai, B. Krishnan, A. V Davydov, J.N. Merrett, Y. Koshka. Growth on differently oriented sidewalls of SiC mesas as a way of achieving well-aligned SiC nanowires. *Cryst. Growth Des.* 12 (2012) 2221–2225. doi:10.1021/cg201398z.

[9] L.E. Luna, C. Ophus, J. Johansson, R. Maboudian, C. Carraro. Demonstration of hexagonal phase silicon carbide nanowire arrays with vertical alignment. *Cryst. Growth*

Des. 16 (2016) 2887–2892. doi:10.1021/acs.cgd.6b00203.

[10] J.D. Caldwell, L. Lindsay, V. Giannini, I. Vurgaftman, T.L. Reinecke, S.A. Maier, O.J. Glembocki. Low-loss, infrared and terahertz nanophotonics using surface phonon polaritons. *Nanophotonics* 4 (2015) 44–68. doi:10.1515/nanoph-2014-0003.

[11] E. Ramsay. High-temperature integrated circuits (ICs): proving performance in extreme environments. *Technol. Today* (2012) 15.

[12] Y. Goldberg, M. Levinshtein, S. Rumyantsev. Advanced semiconductor materials, John Wiley & Sons, New York, 2001.

[13] F. Zhao, W. Du, C.-F. Huang. Fabrication and characterization of single-crystal 4H-SiC microactuators for MHz frequency operation and determination of Young's modulus. *Microelectron. Eng.* 129 (2014) 53–57. doi:10.1016/j.mee.2014.07.012.

[14] G.L. Harris. Properties of silicon carbide, INSPEC, The Institution of Electrical Engineers, London, United Kingdom, 1995.

[15] K. Zekentes, K. Rogdakis. SiC nanowires: material and devices. *J. Phys. D. Appl. Phys.* 44 (2011) 133001. doi:10.1088/0022-3727/44/13/133001.

[16] L. Latu-Romain, M. Ollivier. Silicon carbide based one-dimensional nanostructure growth: towards electronics and biology perspectives. *J. Phys. D. Appl. Phys.* 47 (2014) 203001. doi:10.1088/0022-3727/47/20/203001.

[17] R. Maboudian, C. Carraro, D.G. Senesky, C.S. Roper. Advances in silicon carbide science and technology at the micro- and nanoscales. *J. Vac. Sci. Technol. A* 31 (2013) 050805. doi:10.1116/1.4807902.

[18] L. Fradetal, V. Stambouli, E. Bano, B. Pelissier, J.H. Choi, M. Ollivier, L. Latu-Romain, T. Boudou, I. Pignot-Paintrand. Bio-functionalization of silicon carbide nanostructures for SiC nanowire-based sensors realization. *J. Nanosci. Nanotechnol.* 14 (2014) 3391–3397. doi:10.1166/jnn.2014.8223.

[19] X. Zhang, Y. Chen, Z. Xie, W. Yang. Shape and doping enhanced field emission properties of quasialigned 3C-SiC nanowires. *J. Phys. Chem. C* 114 (2010) 8251–8255. doi:10.1021/jp101067f.

[20] R. Wu, K. Zhou, J. Wei, Y. Huang, F. Su, J. Chen, L. Wang. Growth of tapered SiC nanowires on flexible carbon fabric: toward field emission applications. *J. Phys. Chem. C* 116 (2012) 12940–12945. doi:10.1021/jp3028935.

[21] M. Vincent, M.S. Kim, C. Carraro, R. Maboudian. Silicon carbide nanowires as an

electrode material for high temperature supercapacitors. *IEEE 25th Int. Conf. Micro Electro Mech. Syst.* 2012: pp. 39–42. doi:10.1109/MEMSYS.2012.6170088.

[22] J.P. Alper, M.S. Kim, M. Vincent, B. Hsia, V. Radmilovic, C. Carraro, R. Maboudian. Silicon carbide nanowires as highly robust electrodes for micro-supercapacitors. *J. Power Sources* 230 (2013) 298–302. doi:10.1016/j.jpowsour.2012.12.085.

[23] J.P. Alper, S. Wang, F. Rossi, G. Salviati, N. Yiu, C. Carraro, R. Maboudian. Selective ultrathin carbon sheath on porous silicon nanowires: materials for extremely high energy density planar micro-supercapacitors. *Nano Lett.* 14 (2014) 1843–1847. doi:10.1021/nl404609a.

[24] P.M. Sarro. Silicon carbide as a new MEMS technology. *Sensors Actuators A Phys.* 82 (2000) 210–218. doi:10.1016/S0924-4247(99)00335-0.

[25] P. Neudeck, R. Okojie, Liang-Yu Chen. High-temperature electronics - a role for wide bandgap semiconductors? *Proc. IEEE*. 90 (2002) 1065–1076. doi:10.1109/JPROC.2002.1021571.

[26] M. Mehregany, C.A. Zorman. SiC MEMS: opportunities and challenges for applications in harsh environments. *Thin Solid Films* 355-356 (1999) 518–524. doi:10.1016/S0257-8972(99)00374-6.

[27] D.G. Senesky, B. Jamshidi, Kan Bun Cheng, A.P. Pisano. Harsh environment silicon carbide sensors for health and performance monitoring of aerospace systems: a review. *IEEE Sens. J.* 9 (2009) 1472–1478. doi:10.1109/JSEN.2009.2026996.

[28] R.S. Okojie, L.J. Evans, D. Lukco, J.P. Morris. A novel tungsten-nickel alloy Ohmic contact to SiC at 900 °C. *IEEE Electron Device Lett.* 31 (2010) 791–793. doi:10.1109/LED.2010.2050761.

[29] L.J. Evans, R.S. Okojie, D. Lukco. Development of an extreme high temperature n-type ohmic contact to silicon carbide. *Mater. Sci. Forum* 717-720 (2012) 841–844. doi:10.4028/www.scientific.net/MSF.717-720.841.

[30] T. Jang, L.M. Porter, G.W.M. Rutsch, B. Odekirk. Tantalum carbide ohmic contacts to n-type silicon carbide. *Appl. Phys. Lett.* 75 (1999) 3956. doi:10.1063/1.125506.

[31] R.S. Okojie, A.A. Ned, A.D. Kurtz, W.N. Carr. Electrical characterization of annealed Ti/TiN/Pt contacts on N-type 6H-SiC epilayer. *IEEE Trans. Electron Devices* 46 (1999) 269–274. doi:10.1109/16.740888.

[32] R.S. Okojie, D. Lukco, Y.L. Chen, D.J. Spry. Reliability assessment of Ti/$TaSi_2$/Pt ohmic contacts on SiC after 1000 h at 600°C. *J. Appl. Phys.* 91 (2002) 6553.

doi:10.1063/1.1470255.

[33] A. Virshup, F. Liu, D. Lukco, K. Buchholt, A.L. Spetz, L.M. Porter. Improved thermal stability observed in Ni-Based ohmic contacts to n-type SiC for high-temperature applications. *J. Electron. Mater.* 40 (2011) 400–405. doi:10.1007/s11664-010-1449-0.

[34] M. Vincent, J. Zhang, C. Carraro, R. Maboudian. A SiC metallization scheme using an ALD protective layer for harsh environment devices. *IEEE 25th Int. Conf. Micro Electro Mech. Syst.* 2012: pp. 385–388. doi:10.1109/MEMSYS.2012.6170214.

[35] S. Jin, S. Rajgopal, M. Mehregany. Silicon carbide pressure sensor for high temperature and high pressure applications: influence of substrate material on performance. *IEEE 16th Int. Solid-State Sensors, Actuators Microsystems Conf.* 2011: pp. 2026–2029. doi:10.1109/TRANSDUCERS.2011.5969209.

[36] R.G. Azevedo, D.G. Jones, A. V. Jog, B. Jamshidi, D.R. Myers, L. Chen, X. Fu, M. Mehregany, M.B.J. Wijesundara, A.P. Pisano. A SiC MEMS resonant strain sensor for harsh environment applications. *IEEE Sens. J.* 7 (2007) 568–576. doi:10.1109/JSEN.2007.891997.

[37] W.-C. Lien, K.B. Cheng, D.G. Senesky, C. Carraro, A.P. Pisano, R. Maboudian. Growth of 3C-SiC thin film on AlN/Si(100) with atomically abrupt interface via tailored precursor feeding procedure. *Electrochem. Solid-State Lett.* 13 (2010) D53. doi:10.1149/1.3418619.

[38] A.R. Oliveira, I. Pereyra, M.N.P. Carreño. A study of metal contact properties on thermal annealed PECVD SiC thin films for MEMS applications. *Phys. Status Solidi*. 7 (2010) NA–NA. doi:10.1002/pssc.200982839.

[39] S. Jin, X. Fu, M. Mehregany. Ohmic contacts on n-type polycrystalline silicon carbide with Ti/$TaSi_2$/Pt. *IEEE Int. Solid-State Sensors, Actuators Microsystems Conf., Transducers* 2009: pp. 1083–1086. doi:10.1109/SENSOR.2009.5285947.

[40] T.H. Lee, K.M. Speer, X.A. Fu, S. Bhunia, M. Mehregany, Polycrystalline silicon carbide NEMS for high-temperature logic. *IEEE Int. Solid-State Sensors, Actuators Microsystems Conf., Transducers* 2009: pp. 900–903. doi:10.1109/SENSOR.2009.5285907.

[41] S. Roy, R.G. DeAnna, C.A. Zorman, M. Mehregany. Fabrication and characterization of polycrystalline SiC resonators. *IEEE Trans. Electron Devices*. 49 (2002) 2323–2332. doi:10.1109/TED.2002.807445.

[42] R.K. Burla, S. Roy, V.M. Haria, C. A. Zorman, M. Mehregany. High-temperature testing of nickel wire bonds for SiC devices. *Proc. SPIE: Int. Soc. Opt. Eng.* 1999: pp. 324–333. doi:10.1117/12.368440.

[43] C. Jacob, P. Pirouz, H.-I. Kuo, M. Mehregany. High temperature ohmic contacts to 3C–silicon carbide films. *Solid. State. Electron.* 42 (1998) 2329–2334. doi:10.1016/S0038-1101(98)00234-2.

[44] F. Liu, B. Hsia, C. Carraro, A.P. Pisano, R. Maboudian. Enhanced ohmic contact via graphitization of polycrystalline silicon carbide. *Appl. Phys. Lett.* 97 (2010) 262107. doi:10.1063/1.3531552.

[45] J. Crofton, L.M. Porter, J.R. Williams. The physics of ohmic contacts to SiC. *Phys. Status Solidi*. 202 (1997) 581–603. doi:10.1002/1521-3951(199707)202:1<581::AID-PSSB581>3.0.CO;2-M.

[46] F. Roccaforte, F. La Via, V. Raineri. Ohmic contacts to SiC. *Int. J. High Speed Electron. Syst.* 15 (2005) 781–820. doi:10.1142/S0129156405003429.

[47] J. Zhang, R.T. Howe, R. Maboudian. Nickel and platinum ohmic contacts to polycrystalline 3C-silicon carbide. *Mater. Sci. Eng. B* 139 (2007) 235–239. doi:10.1016/j.mseb.2007.03.006.

[48] G.S. Marlow, M.B. Das. The effects of contact size and non-zero metal resistance on the determination of specific contact resistance. *Solid. State. Electron.* 25 (1982) 91–94. doi:10.1016/0038-1101(82)90036-3.

[49] V.V. Felmetsger, P.N. Laptev, S.M. Tanner. Innovative technique for tailoring intrinsic stress in reactively sputtered piezoelectric aluminum nitride films. *J. Vac. Sci. Technol. A* 27 (2009) 417. doi:10.1116/1.3089242.

[50] A.C. Ferrari. Raman spectroscopy of graphene and graphite: disorder, electron–phonon coupling, doping and nonadiabatic effects. *Solid State Commun.* 143 (2007) 47–57. doi:10.1016/j.ssc.2007.03.052.

[51] M.A. Pimenta, G. Dresselhaus, M.S. Dresselhaus, L.G. Cançado, A. Jorio, R. Saito. Studying disorder in graphite-based systems by Raman spectroscopy. *Phys. Chem. Chem. Phys.* 9 (2007) 1276–1290. doi:10.1039/B613962K.

[52] N. Ferralis, R. Maboudian, C. Carraro. Evidence of structural strain in epitaxial graphene layers on 6H-SiC(0001). *Phys. Rev. Lett.* 101 (2008) 156801. doi:10.1103/PhysRevLett.101.156801.

[53] S. Kodambaka, J. Tersoff, M.C. Reuter, F.M. Ross. Germanium nanowire growth below the eutectic temperature. *Science* 316 (2007) 729–732. doi:10.1126/science.1139105.

[54] R.S. Wagner, W.C. Ellis. Vapor-liquid-solid mechanism of single crystal growth. *Appl. Phys. Lett.* 4 (1964) 89. doi:10.1063/1.1753975.

[55] J.C. Harmand, G. Patriarche, N. Péré-Laperne, M.-N. Mérat-Combes, L. Travers, F. Glas. Analysis of vapor-liquid-solid mechanism in Au-assisted GaAs nanowire growth. *Appl. Phys. Lett.* 87 (2005) 203101. doi:10.1063/1.2128487.

[56] D.E. Perea, N. Li, R.M. Dickerson, A. Misra, S.T. Picraux. Controlling heterojunction abruptness in VLS-grown semiconductor nanowires via in situ catalyst alloying. *Nano Lett.* 11 (2011) 3117–3122. doi:10.1021/nl201124y.

[57] Y. Wu, P. Yang. Direct observation of vapor−liquid−solid nanowire growth. *J. Am. Chem. Soc.* 123 (2001) 3165–3166. doi:10.1021/ja0059084.

[58] Y. Wang, V. Schmidt, S. Senz, U. Gösele. Epitaxial growth of silicon nanowires using an aluminium catalyst. *Nat. Nanotechnol.* 1 (2006) 186–189. doi:10.1038/nnano.2006.133.

[59] T.I. Kamins, R. Stanley Williams, D.P. Basile, T. Hesjedal, J.S. Harris. Ti-catalyzed Si nanowires by chemical vapor deposition: Microscopy and growth mechanisms. *J. Appl. Phys.* 89 (2001) 1008. doi:10.1063/1.1335640.

[60] H. Adhikari, A.F. Marshall, C.E.D. Chidsey, P.C. McIntyre. Germanium nanowire epitaxy: shape and orientation control. *Nano Lett.* 6 (2006) 318–323. doi:10.1021/nl052231f.

[61] K.A. Dick, K. Deppert, T. Mårtensson, B. Mandl, L. Samuelson, W. Seifert. Failure of the vapor−liquid−solid mechanism in Au-assisted MOVPE growth of InAs nanowires. *Nano Lett.* 5 (2005) 761–764. doi:10.1021/nl050301c.

[62] H.D. Park, A.-C. Gaillot, S.M. Prokes, R.C. Cammarata. Observation of size dependent liquidus depression in the growth of InAs nanowires. *J. Cryst. Growth* 296 (2006) 159–164. doi:10.1016/j.jcrysgro.2006.08.033.

[63] J. Lee, H. Mori, J. Lee, T. Tanaka, K. Penttilä. Phase diagrams of nanometer-sized particles in binary systems. *JOM*. 57 (2005) 56–59. doi:10.1007/s11837-005-0235-6.

[64] K.A. Dick, K. Deppert, L.S. Karlsson, L.R. Wallenberg, L. Samuelson, W. Seifert. A new understanding of Au-assisted growth of III-V semiconductor nanowires. *Adv. Funct. Mater.* 15 (2005) 1603–1610. doi:10.1002/adfm.200500157.

[65] J.S. Ponraj, S.C. Dhanabalan, G. Attolini, G. Salviati. SiC nanostructures toward biomedical applications and its future challenges. *Crit. Rev. Solid State Mater. Sci.* (2016) 1–17. doi:10.1080/10408436.2016.1150806.

[66] R. Yakimova, R.M. Petoral, G.R. Yazdi, C. Vahlberg, A. Lloyd Spetz, K. Uvdal. Surface functionalization and biomedical applications based on SiC. *J. Phys. D. Appl. Phys.* 40 (2007) 6435–6442. doi:10.1088/0022-3727/40/20/S20.

[67] C.-H. Chang, B. Hsia, J.P. Alper, S. Wang, L.E. Luna, C. Carraro, S.-Y. Lu, R. Maboudian. High-temperature all solid-state microsupercapacitors based on SiC nanowire electrode and YSZ electrolyte. *ACS Appl. Mater. Interfaces* 7 (2015) 26658–26665. doi:10.1021/acsami.5b08423.

[68] G. Attolini, F. Rossi, M. Negri, S.C. Dhanabalan, M. Bosi, F. Boschi, P. Lagonegro, P. Lupo, G. Salviati. Growth of SiC NWs by vapor phase technique using Fe as catalyst. *Mater. Lett.* 124 (2014) 169–172. doi:10.1016/j.matlet.2014.03.061.

[69] Y.F. Chen, X.Z. Liu, X.W. Deng. Factors affecting the growth of SiC nano-whiskers. *J. Mater. Sci. Technol.* 26 (2010) 1041–1046. doi:10.1016/S1005-0302(10)60172-7.

[70] H.-J. Choi, H.-K. Seong, J.-C. Lee, Y.-M. Sung. Growth and modulation of silicon carbide nanowires. *J. Cryst. Growth* 269 (2004) 472–478. doi:10.1016/j.jcrysgro.2004.05.094.

[71] Y. Zhang, M. Nishitani-Gamo, C. Xiao, T. Ando. Synthesis of 3C–SiC nanowhiskers and emission of visible photoluminescence. *J. Appl. Phys.* 91 (2002) 6066. doi:10.1063/1.1468278.

[72] X.T. Zhou, H.L. Lai, H.Y. Peng, F.C.K. Au, L.S. Liao, N. Wang, I. Bello, C.S. Lee, S.T. Lee. Thin β-SiC nanorods and their field emission properties. *Chem. Phys. Lett.* 318 (2000) 58–62. doi:10.1016/S0009-2614(99)01398-6.

[73] G. Attolini, F. Rossi, M. Bosi, B.E. Watts, G. Salviati. The effect of substrate type on SiC nanowire orientation. *J. Nanosci. Nanotechnol.* 11 (2011) 4109–4113. doi:10.1166/jnn.2011.3864.

[74] H. Wang, L. Lin, W. Yang, Z. Xie, L. An. Preferred orientation of SiC nanowires induced by substrates. *J. Phys. Chem. C* 114 (2010) 2591–2594. doi:10.1021/jp911911e.

[75] Z. Li, M. Zhang, A. Meng. Synthesis and mechanism of single-crystalline β-SiC nanowire arrays on a 6H-SiC substrate. *CrystEngComm* 13 (2011) 4097. doi:10.1039/c0ce00744g.

[76] A.P. Dabkowska, C.S. Niman, G. Piret, H. Persson, H.P. Wacklin, H. Linke, C.N. Prinz, T. Nylander. Fluid and highly curved model membranes on vertical nanowire arrays. *Nano Lett.* 14 (2014) 4286–4292. doi:10.1021/nl500926y.

[77] J.J. Niu, J.N. Wang, N.S. Xu. Field emission property of aligned and random SiC nanowires arrays synthesized by a simple vapor–solid reaction. *Solid State Sci.* 10 (2008) 618–621. doi:10.1016/j.solidstatesciences.2007.10.020.

[78] G. Larrieu, X.-L. Han. Vertical nanowire array-based field effect transistors for ultimate scaling. *Nanoscale* 5 (2013) 2437–2441. doi:10.1039/C3NR33738C.

[79] D.-L. Kwong, X. Li, Y. Sun, G. Ramanathan, Z.X. Chen, S.M. Wong, Y. Li, N.S. Shen, K. Buddharaju, Y.H. Yu, S.J. Lee, N. Singh, G.Q. Lo. Vertical Silicon Nanowire Platform for Low Power Electronics and Clean Energy Applications. *J. Nanotechnol.* 2012 (2012) 1–21. doi:10.1155/2012/492121.

[80] H. Harima, S. Nakashima, T. Uemura. Raman scattering from anisotropic LO-phonon–plasmon–coupled mode in n-type 4H– and 6H–SiC. *J. Appl. Phys.* 78 (1995) 1996. doi:10.1063/1.360174.

[81] S. Nakashima, T. Kitamura, T. Mitani, H. Okumura, M. Katsuno, N. Ohtani. Raman scattering study of carrier-transport and phonon properties of 4H-SiC crystals with graded doping. *Phys. Rev. B - Condens. Matter Mater. Phys.* 76 (2007) 1–8. doi:10.1103/PhysRevB.76.245208.

[82] J. Fréchette, C. Carraro. Diameter-dependent modulation and polarization anisotropy in Raman scattering from individual nanowires. *Phys. Rev. B* 74 (2006) 161404. doi:10.1103/PhysRevB.74.161404.

[83] W. Lien. Porous and Epitaxial 3C-SiC Thin Films Technology for Micro-electromechanical Systems and Electronics Applications, University of California, Berkeley, 2008.

[84] B. Barda, P. Macháč, S. Cichoň, V. Machovič, M. Kudrnová, A. Michalcová, J. Siegel. Origin of ohmic behavior in Ni, Ni_2Si and Pd contacts on n-type SiC. *Appl. Surf. Sci.* 257 (2010) 414–422. doi:10.1016/j.apsusc.2010.07.003.

[85] S. Cichoň, P. Macháč, B. Barda, V. Machovič, P. Slepička. Raman study of Ni and Ni silicide contacts on 4H– and 6H–SiC. *Thin Solid Films* 520 (2012) 4378–4388. doi:10.1016/j.tsf.2012.02.008.

[86] M. Siad, M. Abdesslam, A.C. Chami. Role of carbon in the formation of ohmic contact in Ni/4H-SiC and Ni/Ti/4H-SiC. *Appl. Surf. Sci.* 258 (2012) 6819–6822. doi:10.1016/j.apsusc.2012.03.108.

[87] L. Holland, S. Ojha. The chemical sputtering of graphite in an oxygen plasma. *Vacuum* 26 (1976) 53–60. doi:10.1016/S0042-207X(76)80624-0.

[88] T.R. Dulski. A manual for the chemical analysis of metals, ASTM International, Ann Arbor, MI, 1996. doi:10.1520/MNL25-EB.

[89] F. Bosselet, J.C. Viala, C. Colin, B.F. Mentzen, J. Bouix. Solid states solubility of aluminum in the δ-Ni_2Si nickel silicide. *Mater. Sci. Eng. A* 167 (1993) 147–154. doi:10.1016/0921-5093(93)90348-I.

[90] D. Connétable, O. Thomas. First-principles study of nickel-silicides ordered phases. *J. Alloys Compd.* 509 (2011) 2639–2644. doi:10.1016/j.jallcom.2010.10.118.

[91] K. Toman. The structure of Ni_2Si. *Acta Crystallogr.* 5 (1952) 329–331. doi:10.1107/S0365110X52001003.

[92] P.G. Neudeck, A.J. Trunek, D.J. Spry, J.A. Powell, H. Du, M. Skowronski, X.R. Huang, M. Dudley. CVD growth of 3C-SiC on 4H/6H mesas. *Chem. Vap. Depos.* 12 (2006) 531–540. doi:10.1002/cvde.200506460.

[93] F. Glas, J.-C. Harmand, G. Patriarche. Why does wurtzite form in nanowires of III-V zinc blende semiconductors? *Phys. Rev. Lett.* 99 (2007) 146101. doi:10.1103/PhysRevLett.99.146101.

[94] Y. Cui, X. Hu, K. Yang, X. Yang, X. Xie, L. Xiao, X. Xu. Influence of nitrogen concentrations on the lattice constants and resistivities of n -type 4H-SiC single crystals. *Cryst. Growth Des.* 15 (2015) 3131–3136. doi:10.1021/cg501216d.

[95] S. Sasaki, J. Suda, T. Kimoto. Lattice mismatch and crystallographic tilt induced by high-dose ion-implantation into 4H-SiC. *J. Appl. Phys.* 111 (2012) 103715. doi:10.1063/1.4720435.

[96] S. Sasaki, J. Suda, T. Kimoto. Doping-induced lattice mismatch and misorientation in 4H-SiC crystals. *Mater. Sci. Forum* 717-720 (2012) 481–484. doi:10.4028/www.scientific.net/MSF.717-720.481.

[97] Y. Cao, L. Nyborg, D.-Q. Yi, U. Jelvestam. Study of reaction process on Ni/4H–SiC contact. *Mater. Sci. Technol.* 22 (2006) 1227–1234. doi:10.1179/174328406X118276.

[98] P. Mélinon, B. Masenelli, F. Tournus, A. Perez. Playing with carbon and silicon at the nanoscale. *Nat. Mater.* 6 (2007) 479–490. doi:10.1038/nmat1914.

[99] M.-J. Youh, C.-L. Tseng, M.-H. Jhuang, S.-C. Chiu, L.-H. Huang, J.-A. Gong, Y.-Y. Li. Flat panel light source with lateral gate structure based on SiC nanowire field emitters. *Sci. Rep.* 5 (2015) 10976. doi:10.1038/srep10976.

[100] S. Chen, P. Ying, L. Wang, G. Wei, F. Gao, J. Zheng, M. Shang, Z. Yang, W. Yang, T. Wu. Highly flexible and robust n-doped SiC nanoneedle field emitters. *NPG Asia Mater.* 7 (2015) e157. doi:10.1038/am.2014.126.

[101] X.L. Feng, M.H. Matheny, C.A. Zorman, M. Mehregany, M.L. Roukes. Low voltage nanoelectromechanical switches based on silicon carbide nanowires. *Nano Lett.* 10 (2010) 2891–2896. doi:10.1021/nl1009734.

[102] R. Hillenbrand, T. Taubner, F. Keilmann. Phonon-enhanced light–matter interaction at the nanometre scale. *Nature* 418 (2002) 159–162. doi:10.1038/nature00899.

[103] J.P. Alper, A. Gutes, C. Carraro, R. Maboudian. Semiconductor nanowires directly grown on graphene – towards wafer scale transferable nanowire arrays with improved electrical contact. *Nanoscale* 5 (2013) 4114. doi:10.1039/c3nr00367a.

[104] B. Krishnan, R.V.K.G. Thirumalai, Y. Koshka, S. Sundaresan, I. Levin, A. V Davydov, J.N. Merrett. Substrate-dependent orientation and polytype control in SiC nanowires grown on 4H-SiC substrates. *Cryst. Growth Des.* 11 (2011) 538–541. doi:10.1021/cg101405u.

[105] P.T.B. Shaffer. A review of the structure of silicon carbide. *Acta Crystallogr. Sect. B Struct. Crystallogr. Cryst. Chem.* 25 (1969) 477–488. doi:10.1107/S0567740869002457.

[106] F.M. Morales, C. Förster, O. Ambacher, J. Pezoldt. α-SiC–β-SiC heteropolytype structures on Si (111). *Appl. Phys. Lett.* 87 (2005) 201910. doi:10.1063/1.2131179.

[107] F. Bechstedt, A. Fissel, J. Furthmüller, U. Kaiser, H.-C. Weissker, W. Wesch. Quantum structures in SiC. *Appl. Surf. Sci.* 212-213 (2003) 820–825. doi:10.1016/S0169-4332(03)00068-0.

[108] C. Cheng, R.J. Needs, V. Heine. Inter-layer interactions and the origin of SiC polytypes. *J. Phys. C Solid State Phys.* 21 (1988) 1049–1063. doi:10.1088/0022-3719/21/6/012.

[109] P. Caroff, J. Bolinsson, J. Johansson. Crystal phases in III-V nanowires: from random toward engineered polytypism. *IEEE J. Sel. Top. Quantum Electron.* 17 (2011) 829–846. doi:10.1109/JSTQE.2010.2070790.

[110] J. Johansson, Z. Zanolli, K.A. Dick. Polytype attainability in III–V semiconductor nanowires. *Cryst. Growth Des.* 16 (2016) 371–379. doi:10.1021/acs.cgd.5b01339.

[111] G. Priante, J.-C. Harmand, G. Patriarche, F. Glas. Random stacking sequences in III-V nanowires are correlated. *Phys. Rev. B* 89 (2014) 241301. doi:10.1103/PhysRevB.89.241301.

[112] R.C.J. Schiepers, F.J.J. Loo, G. With. Reactions between α-silicon carbide ceramic and nickel or iron. *J. Am. Ceram. Soc.* 71 (1988) C–284–C–287. doi:10.1111/j.1151-2916.1988.tb05903.x.

[113] J. Johansson, J. Bolinsson, M. Ek, P. Caroff, K.A. Dick. Combinatorial approaches to understanding polytypism in III–V nanowires. *ACS Nano* 6 (2012) 6142–6149. doi:10.1021/nn301477x.

[114] J. Fréchette, C. Carraro. Resolving radial composition gradients in polarized confocal Raman spectra of individual 3C-SiC nanowires. *J. Am. Chem. Soc.* 128 (2006) 14774–14775. doi:10.1021/ja0656346.

[115] S. Nakashima, A. Wada, Z. Inoue. Raman scattering from anisotropic phonon modes in SiC polytypes. *J. Phys. Soc. Japan* 56 (1987) 3375–3380. doi:10.1143/JPSJ.56.3375.

[116] D.T.J. Hurle. A mechanism for twin formation during Czochralski and encapsulated vertical Bridgman growth of III–V compound semiconductors. *J. Cryst. Growth* 147 (1995) 239–250. doi:10.1016/0022-0248(94)00666-0.

[117] X.G. Ning, H.Q. Ye. Experimental determination of the intrinsic stacking-fault energy of SiC crystals. *J. Phys. Condens. Matter*. 2 (1990) 10223–10225. doi:10.1088/0953-8984/2/50/028.

[118] V.V. Voronkov. Supercooling at the face developing on a rounded crystalization front. *Sov. Phys.-Crystallogr.* 17 (1973) 807–813.

[119] J. Heremans, C.H. Olk, G.L. Eesley, J. Steinbeck, G. Dresselhaus. Observation of metallic conductivity in liquid carbon. *Phys. Rev. Lett.* 60 (1988) 452–455. doi:10.1103/PhysRevLett.60.452.

[120] F.P. Bundy. Direct conversion of graphite to diamond in static pressure apparatus. *Science* 137 (1962) 1057–1058. doi:10.1126/science.137.3535.1057.

[121] F.P. Bundy. Melting of graphite at very high pressure. *J. Chem. Phys.* 38 (1963) 618. doi:10.1063/1.1733715.

[122] J. Johansson, K.A. Dick, P. Caroff, M.E. Messing, J. Bolinsson, K. Deppert, L. Samuelson. Diameter dependence of the wurtzite−zinc blende transition in InAs nanowires. *J. Phys. Chem. C* 114 (2010) 3837–3842. doi:10.1021/jp910821e.

[123] S. Kotamraju, B. Krishnan, G. Melnychuk, Y. Koshka. Low-temperature homoepitaxial growth of 4H–SiC with CH_3Cl and $SiCl_4$ precursors. *J. Cryst. Growth* 312 (2010) 645–650. doi:10.1016/j.jcrysgro.2009.12.017.

[124] V. Suwanmethanond, E. Goo, P.K.T. Liu, G. Johnston, M. Sahimi, T.T. Tsotsis. Porous silicon carbide sintered substrates for high-temperature membranes. *Ind. Eng. Chem. Res.* 39 (2000) 3264–3271. doi:10.1021/ie0000156.

[125] J. Park, S. Heo, J.-G. Chung, H. Kim, H. Lee, K. Kim, G.-S. Park. Bandgap measurement of thin dielectric films using monochromated STEM-EELS. *Ultramicroscopy* 109 (2009) 1183–1188. doi:10.1016/j.ultramic.2009.04.005.

[126] L. Gu, V. Srot, W. Sigle, C. Koch, P.A. van Aken. VEELS band gap measurements using monochromated electrons. *J. Phys. Conf. Ser.* 126 (2008) 012005. doi:10.1088/1742-6596/126/1/012005.

[127] B. Rafferty, S.J. Pennycook, L.M. Brown. Zero loss peak deconvolution for bandgap EEL spectra. *J. Electron Microsc.* 49 (2000) 517–524. doi:10.1093/oxfordjournals.jmicro.a023838.

[128] A.B. Minella, D. Pohl, C. Täschner, R. Erni, R. Ummethala, M.H. Rümmeli, L. Schultz, B. Rellinghaus. Silicon carbide embedded in carbon nanofibres: structure and band gap determination. *Phys. Chem. Chem. Phys.* 16 (2014) 24437–24442. doi:10.1039/C4CP02975E.

[129] P.R. Couchman, W.A. Jesser. Thermodynamic theory of size dependence of melting temperature in metals. *Nature* 269 (1977) 481–483. doi:10.1038/269481a0.

[130] T. Tanaka. Prediction of phase diagrams in nano-sized binary alloys. *Mater. Sci. Forum* 653 (2010) 55–75. doi:10.4028/www.scientific.net/MSF.653.55.

[131] Y. Basin, V. Kuznetsoz, V. Markov, L. Guzei. C-Ni-Si phase diagram (1988 Basin Y. M.), ASM Alloy Phase Diagrams Database, P. Villars, editor-in-chief; H. Okamoto and K. Cenzual, section editors; <http://www1.asminternational.org/AsmEnterprise/APD>, ASM International, Materials Park, OH, 2006.

[132] M. Jackson, R. Mehan, A. Davis, E. Hall. C-Ni-Si phase diagram (1983 Jackson, M. R.), ASM Alloy Phase Diagrams Database, P. Villars, editor-in-chief; H. Okamoto and K. Cenzual, section editors; <http://www1.asminternational.org/AsmEnterprise/APD>, ASM International, Materials Park, OH, 2006.

[133] C.V. Thompson. Solid-state dewetting of thin films. *Annu. Rev. Mater. Res.* 42 (2012) 399–434. doi:10.1146/annurev-matsci-070511-155048.

[134] J. Bischof, D. Scherer, S. Herminghaus, P. Leiderer. Dewetting modes of thin metallic films: nucleation of holes and spinodal dewetting. *Phys. Rev. Lett.* 77 (1996) 1536–1539. doi:10.1103/PhysRevLett.77.1536.

[135] F. Cheynis, E. Bussmann, F. Leroy, T. Passanante, P. Müller. Stress effects on solid-state dewetting of nano-thin films. *Int. J. Nanotechnol.* 9 (2012) 396. doi:10.1504/IJNT.2012.045344.

[136] E.J. Luber, B.C. Olsen, C. Ophus, D. Mitlin. Solid-state dewetting mechanisms of ultrathin Ni films revealed by combining in situ time resolved differential reflectometry monitoring and atomic force microscopy. *Phys. Rev. B* 82 (2010) 085407. doi:10.1103/PhysRevB.82.085407.

[137] D. Kim, A.L. Giermann, C.V. Thompson. Solid-state dewetting of patterned thin films. *Appl. Phys. Lett.* 95 (2009) 251903. doi:10.1063/1.3268477.

[138] P.R. Gadkari, A.P. Warren, R.M. Todi, R.V. Petrova, K.R. Coffey. Comparison of the agglomeration behavior of thin metallic films on SiO_2. *J. Vac. Sci. Technol. A* 23 (2005) 1152. doi:10.1116/1.1861943.

[139] S. Strobel, C. Kirkendall, J.-B. Chang, K.K. Berggren. Sub-10 nm structures on silicon by thermal dewetting of platinum. *Nanotechnology* 21 (2010) 505301. doi:10.1088/0957-4484/21/50/505301.

[140] F. Ruffino, M.G. Grimaldi. Dewetting of template-confined Au films on SiC surface: from patterned films to patterned arrays of nanoparticles. *Vacuum* 99 (2014) 28–37. doi:10.1016/j.vacuum.2013.04.021.

[141] Y. Shishkin, W.J. Choyke, R.P. Devaty. Photoelectrochemical etching of n-type 4H silicon carbide. *J. Appl. Phys.* 96 (2004) 2311. doi:10.1063/1.1768612.

[142] A. Geissler, M. He, J.-M. Benoit, P. Petit. Effect of hydrogen pressure on the size of nickel nanoparticles formed during dewetting and reduction of thin nickel films. *J. Phys. Chem. C* 114 (2010) 89–92. doi:10.1021/jp908427r.

[143] M. Yu, C.S. Jayanthi, S.Y. Wu. Size-, shape-, and orientation-dependent properties of SiC nanowires of selected bulk polytypes. *J. Mater. Res.* 28 (2013) 57–67. doi:10.1557/jmr.2012.237.

[144] N. Ferralis, F. El Gabaly, A.K. Schmid, R. Maboudian, C. Carraro. Real-time observation of reactive spreading of gold on silicon. *Phys. Rev. Lett.* 103 (2009) 256102. doi:10.1103/PhysRevLett.103.256102.

[145] R.J. Phaneuf, A.K. Schmid. Low-energy electron microscopy: Imaging surface dynamics. *Phys. Today* 56 (2003) 50–55. doi:10.1063/1.1570772.

[146] K. V. Emtsev, A. Bostwick, K. Horn, J. Jobst, G.L. Kellogg, L. Ley, J.L. McChesney, T. Ohta, S.A. Reshanov, J. Röhrl, E. Rotenberg, A.K. Schmid, D. Waldmann, H.B. Weber, T. Seyller. Towards wafer-size graphene layers by atmospheric pressure graphitization of silicon carbide. *Nat. Mater.* 8 (2009) 203–207. doi:10.1038/nmat2382.

Appendix A. Cross-sectional TEM sample preparation

Introduction

The following procedure was conducted at the Molecular Foundry in the National Center of Microscopy (NCEM) sample preparation room. A special thank you to scientific engineering associate Marissa Libbee at NCEM for training and guidance during sample preparation.

Step 1. Cut a 5 mm × 5 mm stack from 10 mm × 10 mm coupons

In this work, the starting coupons are double side polished 10 mm × 10 mm squares. Since the side corresponding to the surface of interest cannot be readily distinguish from the other side, it will be difficult to identify surface of interest after the various mechanical processing steps. To avoid confusion, roughen the side you are **not** interested in with diamond sand paper. Scratches should be visible by naked eye.

Mount a glass slide on a rectangular metal block with Crystalbond. For Crystalbond to melt, it has to be heated to ~180 °C on the designated hot plate.

Add Crystalbond in an amount comparable to the size of your sample on a heated glass slide. Make sure to add enough Crystalbond so that the edges of your sample are also protected with Crystalbond.

Mount surface of interest with Crystalbond onto a glass slide. This means the surface of interest is in contact with Crystalbond. Make sure to add enough Crystalbond so that the entire surface is covered. Use Model 650 low speed diamond wheel saw (South Bay Technology) to cut stack. Low concentration diamond blade can be used to cut silicon carbide samples. Add water mixed with yellow lubricant fluid to tray so that water level just touches the blade. Water should appear a light yellow color. Cut sample into 5 mm x 5 mm squares. Need to cut a counter substrate also into 5 mm × 5 mm squares.

Step 2. Make 5 mm × 5 mm stack with 2 coupons: 4H-SiC (0001) / Ni_2Si on 4H-SiC (0001)

Two same size coupons/samples are necessary to begin. If you are starting with coupons larger than 5 mm × 5 mm squares, follow Step 1 to make two 5 mm × 5 mm. One or both can contain a surface of interest. This part will describe the steps assuming there is only 1 coupon with a surface of interest. As such, a counter or blank substrate of the same size will be used to protect the surface of interest during mechanical processing.

Take out epoxy from refrigerator and let it stabilize at room temperature for a few minutes. Set the hot plate to 250 °C (thermometer should read 160 °C). Prepare aluminum foil to serve as a container for curing epoxy in the vice. In the hood, mount two substrates (with surface of interest facing inside) with epoxy from fridge. Place within aluminum foil in vice and fold the foil edges to prevent epoxy from spilling out. Cure in vice on hot plate (sample facing hot plate) for 90 minutes to minimize glue/epoxy line (Figure A.1). Store epoxy back in refrigerator. The goal of the vice is to establish the thinnest glue/epoxy line possible.

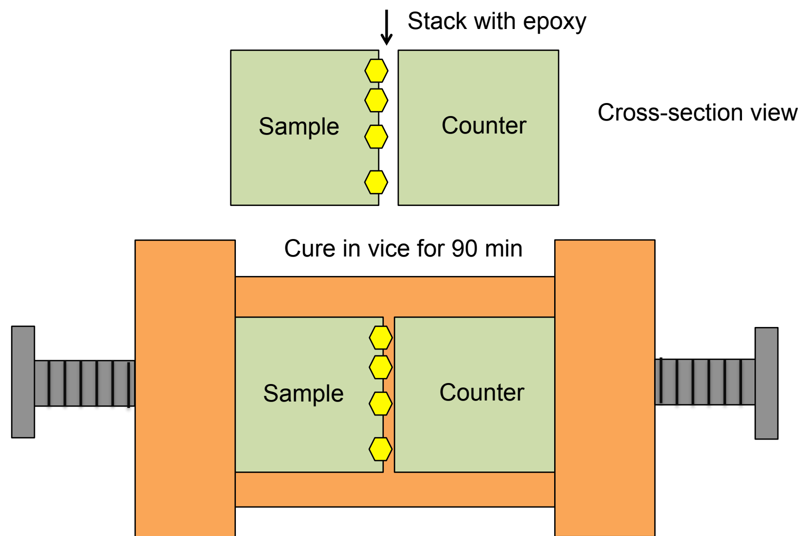

Figure A.1. Schematic of initial 5 mm × 5 mm stack with surface of interest facing the counter substrate. The surface of interest is in contact with epoxy that is cured for 90 min. A very thin glue line is ideal. Aluminum foil described in procedure is not shown here.

Step 3. Sandwich 5 mm × 5 mm stack with Si coupons: Si / Si /4H-SiC (0001) / Ni_2Si on 4H-SiC (0001) / Si / Si

Take epoxy out of refrigerator. Cut Si dummy pieces into 5 mm × 5 mm following Step 1. Gently knick Si with diamond cutter, place glass slide under cut and press down to break Si along the knick. Use epoxy to sandwich 2 Si coupons on each side of the already cured sample from Step 2. Place and center sandwiched stacking with Si coupons within an Al foil cage within vice. Tighten the vice and fold Al foil edges over each other to prevent epoxy leakage onto vice.

Place sample side face down on hot plate and let cure in vice for 90 min. Use tongs to let vice cool on chill plate. Now we have the following 5 mm x 5 mm stack: Si/Si/4H-SiC(0001)/clusters on 4H-SiC(0001)/Si/Si (Figure A.2).

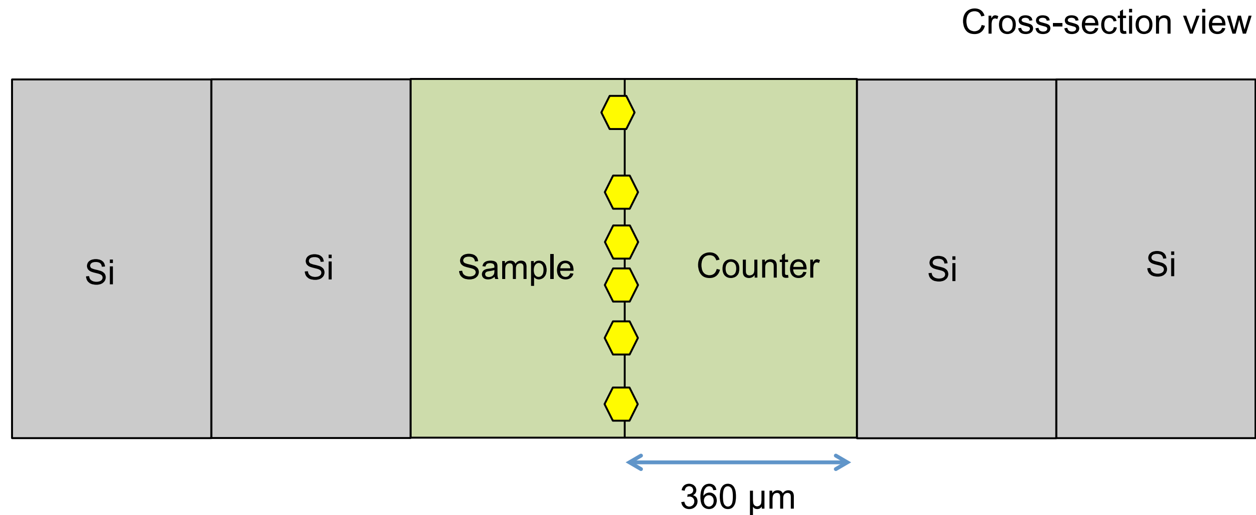

Figure A.2. Schematic of 5 mm × 5 mm stack sandwiched with Si coupons. A very thin glue line is ideal between all coupons. However, the most critical glue line is that at the interface of interest. A thin glue line at interface of interest improves imaging.

Step 4. Cut 5 mm × 5 mm stack into 1 mm thick slabs

Use Model 650 low speed diamond wheel saw (South Bay Technology) to cut stack into 1 mm thick slabs. Mount stack onto saw platform such that the blade cut lines and are perpendicular to the interface of interest. Discard first edge slice. Using the center slice is the ideal TEM sample, but other slices can also be used. Use Model 360 rotary disc cutter with silicon carbide slurry to cut out a 3 mm disk (the TEM sample holder holds 3 mm disks). Polishing with abrasive papers,

dimpling with Dimpler, and etching a hole with ion milling (PIPS 2) are the final steps to achieve an electron transparent region in the 3 mm disk.

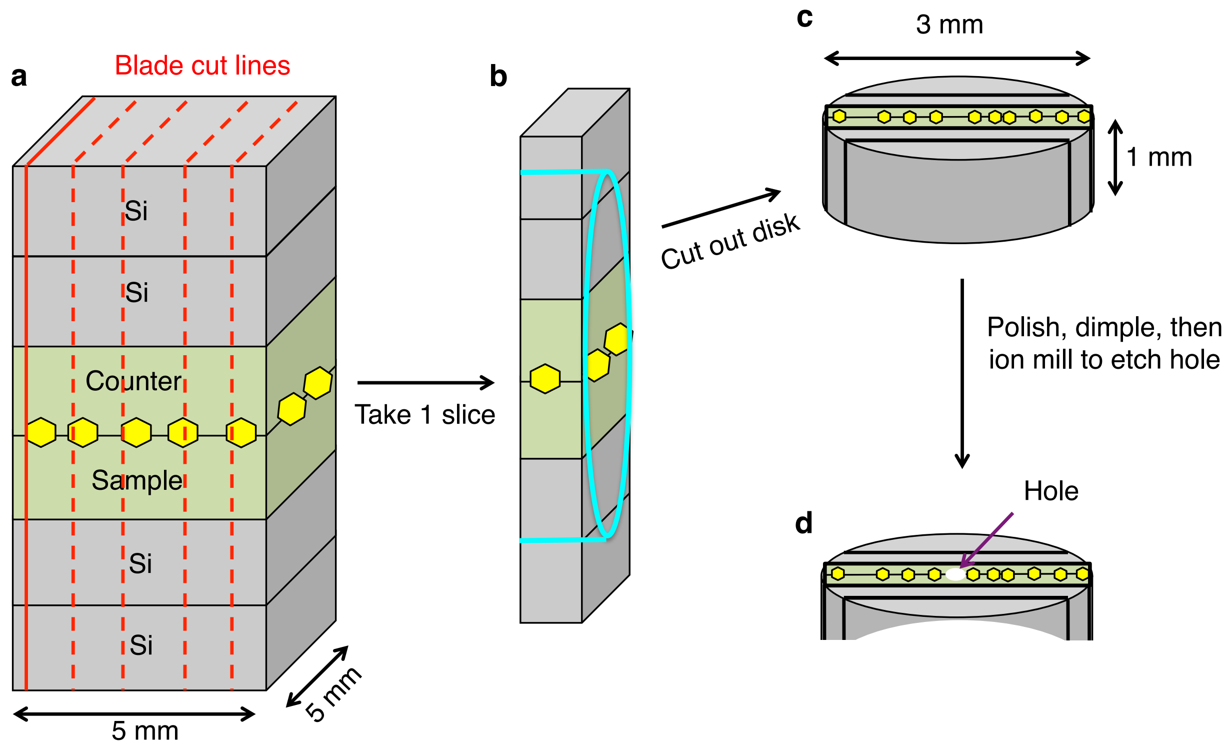

Figure A.3. Flow diagram of sample thinning. (a) Cut 1 mm slices using wheel saw. (b) Isolate 1 slice, preferably center slice. (c) Cut 3 mm disk out of 1 mm slice using rotary cutter. (d) After polishing, dimpling, and ion milling, the 3 mm disk will have a hole in the middle of the interface of interest. Electron transparent regions surround hole.

Step 5. Polish (Multiprep) and Dimple (Dimpler)

Use Multiprep to polish TEM side 1. Use varying roughness of diamond paper: 30, 6, 3, 1, 0.1 (or 0.25) µm. Use Dimpler to dimple the same side such that the thickness at the dimple is ~ 10 µm. Start with brass, flat polishing wheel and 6-µm slurry. Then switch to stainless steel (ss) polishing wheel with 3-µm slurry. Finish with, ss, texmet polishing wheel with 3-µm slurry. Use optical microscope to check for scratch density.

Step 6. Ion Mill (PIPS 2) to electron transparency.

PIPS 2 Quick Overview:

A) Align stage to center of its rotation
B) Align right beam to A (with macor stud)
C) Align left bottom gun to A (with transparent glass slide)
D) Align sample to where beam is aligned

A) Align stage to center of its rotation.

- Place stage straight down, put cap on
- Lower stage
- Click "Camera"→ live view. Move camera over micrometer to move alignment screen in view.
- Track a **feature** using Lasso Tool in Digital Micrograph to approximate center of rotation.
- Click "Alignment" → home
- Select Line Tool in Digital Micrograph.
- Draw a line from the feature to the center of rotation.
- Go "home" again to see if the center of rotation is a good estimate.
- Lift camera up manually and lift sample up on touch screen.
- Vent
- Focus camera, reduce illumination
- Move reference line (that we drew earlier) so that one end begins at the **feature** again.
- Use tool to move hole so its center is aligned with the center of rotation
- Place cap on, put sample down (it pumps down automatically)
- Focus camera and check rotation.
- Remove camera and rotate

B) Align beam to A

- Milling: start beam at 5keV
- Camera, turn OFF bottom illumination
- Move beam to 10°, no modulation
- Align beam to have uniform cross beam
- Set Left beam to 4° and Right beam to 5°. The Right beam is most important.
- Raise sample, Vent
- Change holder with glass/dummy sample, lower.
- Align Left beam. Move to - 4°. Adjust beam on glass.
- Raise and put in sample with interface parallel to desk edge, with cluster side closest to your body. Lower sample.

D) Align sample to where beam is aligned

- Want to align sample to center of rotation of lasso circle.
- Enter live view with camera all the way at the left hard stop.

- Lower sample
- Follow debris on sample with Lasso Tool.
- Go home.
- Mark center with a cross. Draw a line for another particle to the center of the cross.
- Bring sample up, raise camera with big black knobs, and remove cap. Use micrometers on stage to manually move sample to the new center.
- Take a picture.
- Add liquid nitrogen. Wait for coldfinger to reach -172 °C.
- Make sure both beams are on.
- Start ion milling in increments of 20 min.
- Camera → red illumination → black/red image to see thickness fringes.
- When done, stop beam, raise sample. Wait ~20 min for sample to heat up.
- If someone is coming after you, enable “cold stage heater” with 23 C set point.
- If you are the last one or the person next to you is using LN2, enable “dewar heater”

Notes:

- When hole growth is approaching glue line, reduce voltage to 1keV for at least 10 min.
- Afterwards, reduce to 0.5 keV for 5 min.
- Then 0.1 keV for 1 min.
- Raise the sample and let warm up for 20 min.

Appendix B. Common surface reconstructions

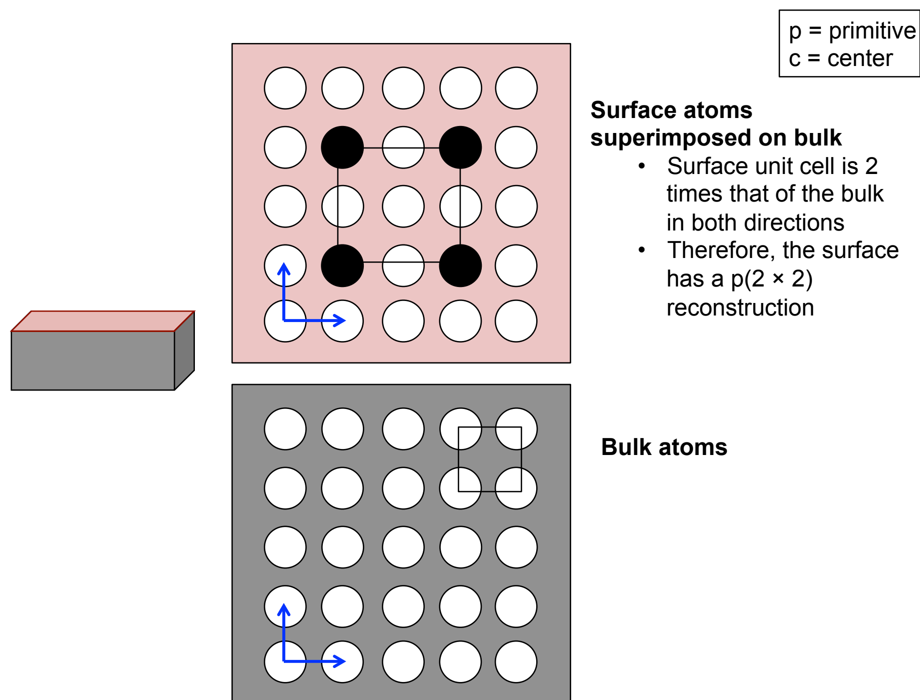

Figure B.1. Surface reconstructions of a square lattice.

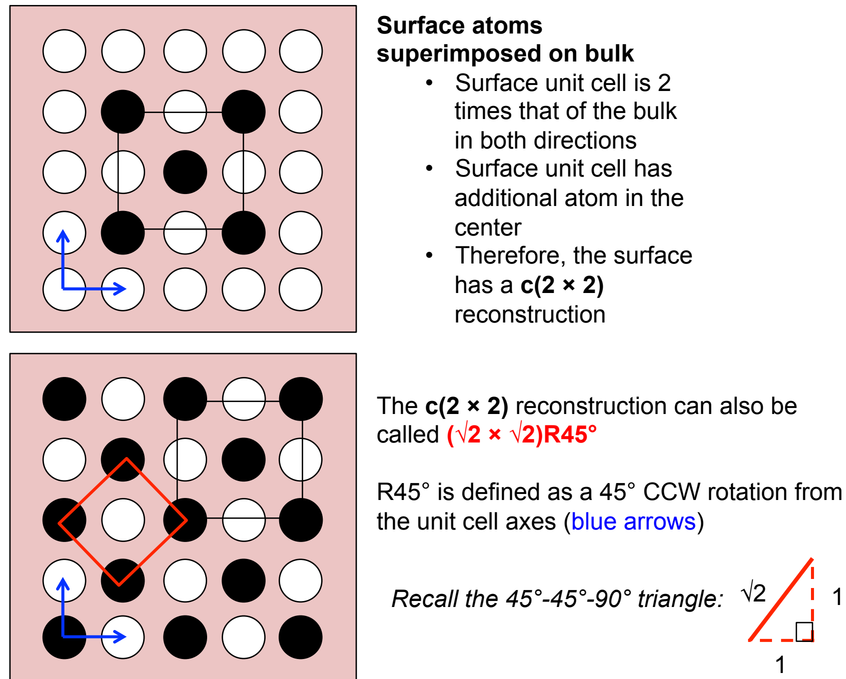

Figure B.2. Surface reconstructions of a square lattice.

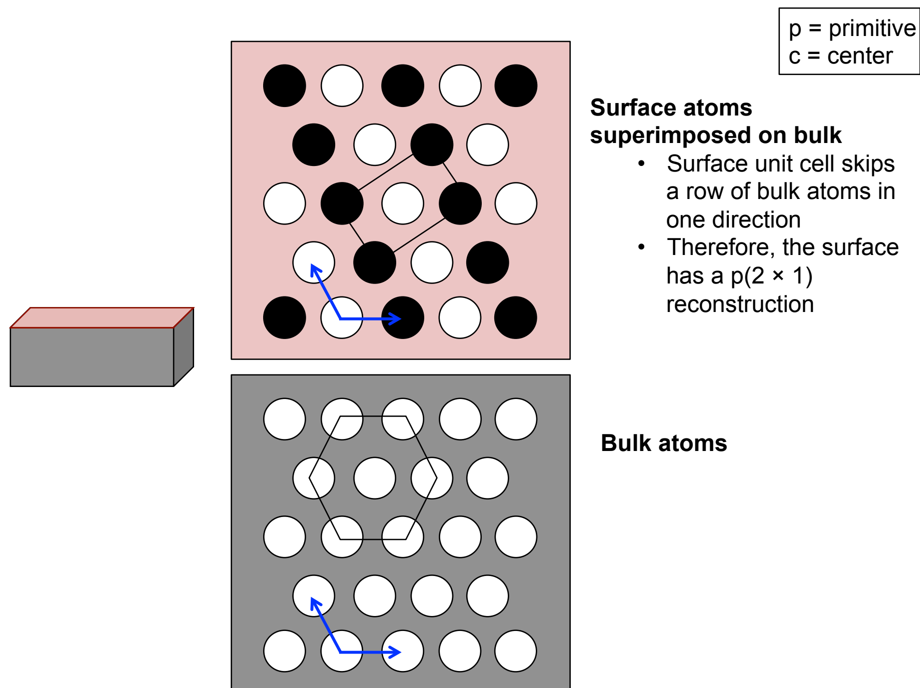

Figure B.3. Surface reconstructions of a hexagonal lattice.

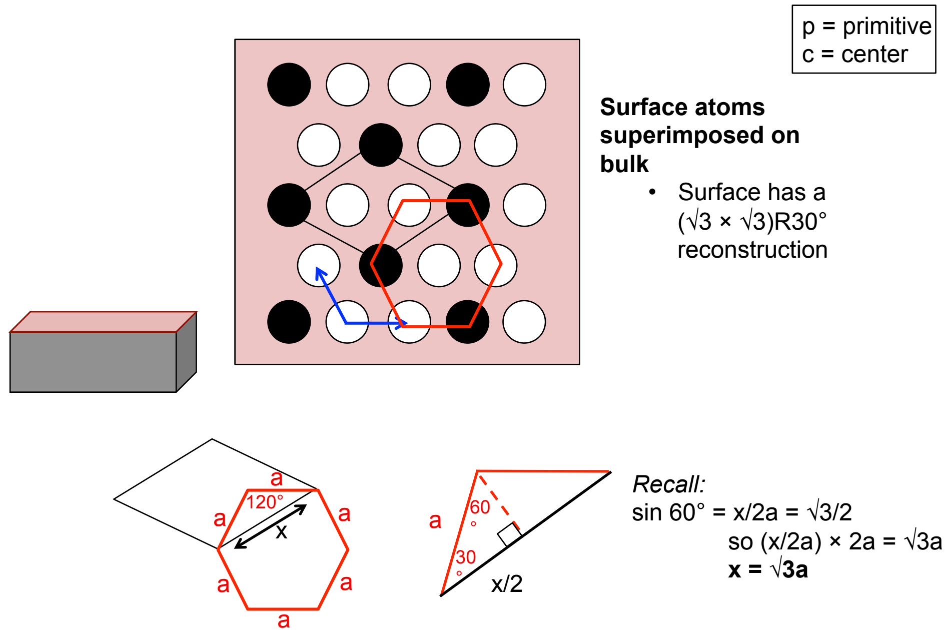

Figure B.4. Surface reconstructions of a hexagonal lattice.